Construction of an enzyme-free electrochemical sensor based on Ag-Fe_2O_3/POM/RGO novel nanocomposite for hydrogen peroxide detection

By

Noniko Civilized Nqakala

(BSc Honours)

A full thesis submitted in fulfilment of the requirements for the degree of Magister Scientiae in the Department of Chemistry, University of the Western Cape.

Faculty of Science
University of the Western Cape
Cape Town / South Africa

Supervisor: Dr N Ross

Co-supervisor: Dr M Bilibana

December 2018

KEYWORDS

Polyoxometalate (POM)

Enzyme-less electrochemical sensor

Hydrogen peroxide (H_2O_2)

Cyclic voltammetry (CV)

Amperometry (AMP)

Limit of detection (LOD)

Limit of quantification (LOQ)

Real life analysis

ABSTRACT

The motivation to determine H_2O_2 lies in the fact that this chemical species plays a crucial role in diverse fields of practise such as cosmetic, food, diagnostic, pharmaceutical, clinical and environmental protection industries. Several methods such as chromatography, colorimetry, titrimetry and spectrophotometry have been developed for its detection. However, these methods are known to manifest underlying disadvantages such as high cost, time consuming, instability and complicated immobilization procedures. In this present study an enzyme-less electrochemical sensor based on Ag-Fe_2O_3/POM/RGO nanocomposite (POM stands for polyoxometalate and RGO stands for reduced graphene oxide) was successfully synthesised via a hydrothermal method and a photochemical reduction method for the detection of hydrogen peroxide (H_2O_2).

Graphene oxide (GO) was chemically reduced by sodium borohydride to RGO. UV-Vis, FTIR, Raman and XRD studies confirmed the reduction process. The disappearance of the vibrational peak at 3126 cm^{-1} assigned to O-H stretching in the FTIR of RGO and the disappearance of the shoulder located at 291 nm in the Uv-Vis absorption of RGO due to the removal of oxygen-containing functional groups suggested that GO was reduced to RGO. The photochemical reduction of POM at the surface of RGO sheet was followed by hydrothermal synthesis of Ag-Fe_2O_3 to form the novel Ag-Fe_2O_3/POM/RGO nanocomposite. The synthesised composites, namely POM/RGO, Ag-Fe_2O_3 nanoparticles and Ag-Fe_2O_3/POM/RGO were studied using UV-Vis, FTIR, XRD, SEM, TEM, AFM, EDX and SAXS analysis. The TEM revealed that the Ag-Fe_2O_3 nanoparticles onto the POM/RGO surface had different shape and size, with the Ag being of a spherical shape with size ranging from (3-5) nm and the Fe_2O_3 nanoparticles with irregular shapes being (15-16) nm in size. SASX analysis revealed that these nanoparticles on the surface of POM/RGO are very close to each other with the Fe_2O_3 nanoparticles being more intense than the Ag nanoparticles. XRD analysis showed that the Ag-Fe_2O_3/POM/RGO nanocomposite had rhombohedral and spherical crystalline structure due to Fe_2O_3 and Ag nanoparticles respectively, this high crystallinity was further confirmed by the Selected area (electron) diffraction of the novel nanocomposite.

The Ag-Fe_2O_3/POM/RGO nanocomposite was further modified on a glassy carbon electrode (GCE) and was used to investigate its electrochemical properties. The cyclic voltammetry (CV) revealed that the Ag-Fe_2O_3/POM/RGO nanocomposite has excellent electroreduction behaviour towards H_2O_2 when compared to the response of GCE due to the presence of POM/RGO which enhanced the rate of transfer of electrons during the electrochemical reduction of H_2O_2. Amperometric method was further used to quantify H_2O_2 using Ag-Fe_2O_3/POM/RGO nanocomposite, and the response was linear over the concentration ranging from 0.3 mM to 3.3 mM ($R^2 = 0.992$). The detection limit and sensitivity were calculated to be 0.0029 mM and 270.96 μA.Mm^{-1}cm^{-2}, respectively with the response time of about 5 s at a signal to noise ratio (S/N=4). The fabricated sensor was also used for the detection of H_2O_2 in the presence of potentially active interfering species, and found high selectivity towards H_2O_2. Further studies of this sensor with real life water samples obtained from the Western Cape Science Services showed that the sensor was able to detect and reduce H_2O_2 successfully with relative standard deviation (RSD) % values being less than 4.2 %. This sensors good performance is attributed to the synergetic effect of the Ag-Fe_2O_3 nanoparticles and POM with RGO. RGO is believed to have increase the surface area roughness and therefore acted as an excelled underneath layer. POM served as a matrix for incorporating the nanoparticles. The metal-metal oxide nanoparticles (Ag-Fe_2O_3) NPs exhibited an irregular size distribution and helped to enhance the electrocatalytic activity and increased the sensitivity of the fabricated sensor.

DECLARATION

I hereby **declare** that *“**Construction of an enzyme-less electrochemical sensor based on Ag-Fe_2O_3/POM/RGO novel nanocomposite for hydrogen peroxide detection**”* is my own work, and that it has not been submitted for any degree or examination in any other university, and that all sources I have used or quoted have been indicated and acknowledged by complete references.

Noniko Civilized Nqakala **Date: December 2018**

Signature:

Dr Natasha Ross **Date: December 2018**

Signature:

ACKNOWLEDGEMENTS

"*I can do all things through Christ, who strengthens me"* a verse from Philippians chapter 4. To the **Almighty God**, whom has given me strength, courage and vison, I thank you. For you armed me with your strength and kept my way secure through difficult and good times. Father, your guidance and love gave me strength, dedication, hope and courage to complete this work.

In preparing this dissertation, I am indebted to many people. I would like to express my sincere thanks to my **supervisors**' **Dr N Ross, Dr M Bilibana** and **Prof Emmanuel Iwuoha**, for their help and guidance throughout the research process. Without their constructive comments and guidance, this dissertation would have not been possible

To the **Nqakala family**: For putting me in their prayers, their love and support kept me going. To my sisters: **Nombuyiselo and Zimkhitha.** To my brother **Yamkela**. To my grandmother **Nothandekile.** To my nieces and nephews: **Othandwayo, Esekho, Lunathi, Siphesihle, Bonakele, Myolisisi, Lonwabo** and **Ntando**. Thank you for giving me a reason to stay focused and to never give up.

My appreciation goes to the **Department of Chemistry staff, SensorLab researchers** and my **colleagues** especially **Dr Masikini, Dr T Waryo** and **Miranda Ndiphingwi.** Thank you for your assistance.

The contributions of my beloved friends: **Nkazimulo Feketshane, Nzaliseko Mashiya, Juliat Clementine Louw, Siphokazi Tshoko, Sabelo Sifuba,** and **Bangile Rholihlahla** are highly appreciated. You have been a great team to work with.

I would also like to acknowledge the **CSIR, SensorLab and Chemistry Department** for funding my studies.

Lastly, yet very important, I would like to express my heartfelt thanks to my lovely mother: **Bukelwa Nqakala**, this is for you. Thank you very much for your love, care and upbringing. You are truly the best gift from God.

TABLE OF CONTENTS

ACRONYMS AND ABBREVIATIONS

H_2O_2	Hydrogen peroxide
POM	Polyoxometalate
NPs	Nanoparticles
GO	Graphene oxide
RGO	Reduced graphene oxide
Ag-Fe_2O_3/POM/RGO	Silver-Iron Oxide/Polyoxometalate/Reduced graphene oxide
CV	Cyclic voltammetry
EIS	Electrochemical impedance spectroscopy
XRD	X-ray diffraction
FTIR	Fourier transform infrared spectroscopy
TEM	Transmission electron microscopy
SEM	Scanning electron microscopy
AFM	Atomic force microscopy
R_{ct}	Charge transfer resistance
CPE	Constant phase element
W_o	Warburg open circuit
E_{pa}	Anodic peak potential
E_{pc}	Cathodic peak potential
I_{pc}	Cathodic peak current
I_{pa}	Anodic peak current
E°	Formal potential
SAED	Selected area (electron) diffraction
RSD	Relative standard deviation

LIST OF FIGURES

LIST OF TABLES

LIST OF SCHEMES

CHAPTER 1

Chapter Overview

This chapter gives an overview on the importance of detecting hydrogen peroxide (H_2O_2) and the rationale behind the choice of electrochemical detection methods over other reported analytical methods. Disadvantages associated with electrochemical enzyme sensors over non-enzyme sensors based on previously conducted studies are also discussed. The chapter further elaborates on the rationale behind the use of Graphene oxide, Silver-Iron Oxide nanoparticles and Polyoxometalate (POM) for the construction of enzyme-free electrochemical H_2O_2 sensor. The research objectives, problem statement and motivation of the study are presented. The chapter closes with a general outline of the thesis layout.

1.1 Introduction

Discovered by Louis Auguste Thenard, a French Scientist in 1818, hydrogen peroxide is a compound with the chemical formula (H_2O_2); it is a pale-blue covalent liquid in its pure form but appears colourless in a dilute solution, somewhat more viscous than water (Scandurra et al., 2013). It is the simplest of the class of peroxides (compounds with an oxygen-oxygen single bond). In chemical terms, H_2O_2 is poorly reactive; its chemistry is subjugated by the identity of its unstable peroxide bond. It is found in small amounts in the environment (air and water) and in biological systems including the human body (Y et al., 2000).

In the human body, produced by a secondary class of white blood cells called neutrophils, H_2O_2 functions as the first line of protection against toxins, bacteria, parasites, viruses and yeast. H_2O_2 also plays an important role in modifying the renal function and has an antibacterial effect that is advantageous at high levels in urine that could reduce bladder and urinary tract infections (Yusoff et al., 2017). However, high (usually$\geq$ 50 µM) levels of H_2O_2 are toxic to human health, including irritating the eyes, skin, and can constitute a pathogenic factor in vascular organ damage attendant upon systemic hypertension. These high levels can be controlled by excretion and catabolism (Y et al., 2000).

In industrial applications, H_2O_2 is one of the components in rocket fuels, in tooth whitening paste, laundry detergent, and purification of water and healing purposes. At high concentrations, H_2O_2 can also be used as bleach for textiles and paper. Due to its powerful oxidizing properties that allow it to react with viruses, spores, yeast and bacteria, H_2O_2 is used as a chemical agent for sterilization in the food industry (Liu, Liu & Chen, 2013). Thus, the detection and quantification of H_2O_2 is of significance.

Several techniques including chromatography, colorimetry, chemiluminescence, titrimetry, spectrophotometry, fluorimetry and electrochemistry (Keston & Brandt, 1965; Bader, Sturzenegger & Hoigné, 1988; Uchida et al., 2004; Tarvin et al., 2010; Liu, Tian, et al., 2012; Liu, Liu & Chen, 2013; Hsu et al., 2015) have been developed to detect and measure hydrogen peroxide. In comparison with the other techniques, the electrochemical methods are cost effective, require simpler experimental set up and allows sensitive and fast detection of hydrogen peroxide with sensitivities as low as 0.01 (µA mM^{-1} cm^{-2}) and detection limits ranging from (0.01 to 57 000)µM (Liu, Li, et al., 2012; Liu, Weng & Yang, 2017). It is for these reasons that the science community is on a frenzy for electrochemical techniques. Currently, a majority of research on electrochemical detection of hydrogen peroxide is done to develop and characterize the modified electrode on the surface where reduction/oxidation of hydrogen peroxide is achievable, by operating at low voltage thus improving the sensors selectivity (Scandurra et al., 2013).To improve the electrochemical detection of H_2O_2 sensors, the electrode can be fabricated using either carbon micro and nanomaterials, nanostructured metal oxides, conducting polymers, metal and metal alloy nanomaterials composites (Kumar et al., 2018).

Ever since its discovery by Novoselov and Geim in 2004, graphene, a sp^2 hybridized 2D sheet of single thick carbon atom has become the main focus in the science community because of its unique electronic, optical , mechanical , thermal and chemical properties (Teymourian, Salimi & Khezrian, 2013). Due to these properties it has been widely used in nanomaterial and nanotechnology applications. Graphene Oxide, a derivative of graphene has been an ideal material for electrochemistry due to its ability to provide a large specific surface area for the attachment of large amounts of substances such as nanoparticles, metals and biomolecules (Dhara et al., 2016). This can in turn enable high sensitivity, selectivity and manufacturing of small devices in electrochemical sensors (Li, Du, et al., 2010). Apart from the applications of graphene and graphene oxide, mixing of graphene oxide with nanoparticles, metals , metal oxides polyoxometalates and polymers into nanocomposites have received great attention due to their new and/or enhanced properties that cannot be achieved by either component alone and therefore holds a wide variety of applications in catalysis, sensors and medical field (Teymourian, Salimi & Khezrian, 2013). A wide range of graphene based composites, such as graphene metal oxides, graphene-metal and polyoxometalate-graphene oxide composites have been exploited as electrochemical sensors for the detection of H_2O_2 (Paul et al., 2016; Zhang & Zheng, 2017). Polyoxometalates (POMs) are combinations between oxygen and early transition metals (e.g. M= V, Nb, Ta, Mo, W) at their high oxidation states with high structural, electronic and chemical versatility (Ammam, 2013). Due to their interesting structural and physicochemical properties, POM's are prospective candidates for electrochemical applications such as photocatalysis, energy storage systems and sensors (Lin, Hu & Song, 2017).

With the ever increasing developments of nanotechnology and nanoscience, an extensive variety of nanomaterials particularly, nanoparticles have become a hot topic because of their unique physicochemical properties. Among them are magnetic nanoparticles, particularly iron oxide (Fe_2O_3) have been exploited for use in gas sensors, electrochemical sensors, lithium ion batteries, catalysis, biomedical and biological applications (Pan, Tang & Chen, 2013). On the other hand, integration of iron oxide nanoparticles with other metals or transition metals oxide into a nanocomposite has attracted more attention due to their synergetic effect, and therefore leading to enhanced properties and wide range of applications. Among these nanocomposites are silver/iron oxide nanocomposites (Ag-Fe_3O_2) which have been used more in catalysis (Biabani-ravandi, Rezaei & Fattah, 2013). For example, (Jang et al., 2009) developed Ag-Fe_2O_3 nanocomposite photocatalyst for water oxidation. (Narasimharao, Al-Shehri & Al-Thabaiti, 2015) also synthesised Ag-Fe_2O_3 nanocomposite catalyst for oxidation of carbon monoxide. Also Ag-Fe_3O_2 composite was synthesised by (Gao, Chen & Jiang, 2013) but it was for antibacterial property. The interest in integrating Ag in the iron oxide composite is to explore on properties of Ag nanoparticles which include biocompatibility, high electrical conductivity and large surface area (Evanoff & Chumanov, 2005). However Ag nanoparticles aggregate hence limiting their use, thus many research have shown that a graphene material can protect the nanoparticles against aggregation (Geetha Bai et al., 2016; Shaikh, Parida & Böhm, 2016; Zhao, Zhang & Zheng, 2017).

In a research done by (Kumar et al., 2018) toward the detection of H_2O_2, a silver nanoparticle-reduced graphene oxide–polyaniline composite was constructed; the silver nanoparticles immobilized onto the reduced graphene oxide did not aggregate. (Bai et al., 2014) used the modification of a silver mirror to construct an Ag/RGO nanocomposite for electrochemical sensing. (Xu et al., 2011)a simple and scalable method for preparation of Ag/RGO. From these researches it was found that graphene oxide can be used to protect the silver nanoparticles towards aggregation. Incorporating Fe_2O_3-Ag nanoparticle composite with graphene oxide to form Ag-Fe_2O_3-graphene oxide nanocomposite will lead to enhanced chemical properties. This study presents findings on the development of a cost effective, sensitive and selective enzyme free electrochemical sensor based of the novel Ag-Fe_2O_3/POM-RGO nanocomposite modified glassy carbon electrode for the detection of H_2O_2.

1.2 Problem Statement

Despite the fact that there are numerous techniques for detecting H_2O_2 there still exists some disadvantages associated with the reported preferred electrochemical techniques. The electrochemical detection technique of H_2O_2 is achieved through non-enzyme and enzyme-based sensors. Even though, so far advanced enzyme-based sensors have high sensitivity and selectivity, they also exhibit some drawbacks, such as instability, high costs, restricted storage time and complicated immobilization procedures. Horseradish Peroxidase (HRP), haemoglobin (Hb), myoglobin (Mb) and cytochrome C (Cyt *c*) (Lei et al., 2003; Ahammad, 2012; Wang et al., 2012; Dinesh et al., 2014) are the most commonly used enzymes for the construction of H_2O_2 biosensors. The major challenge with these is that, the direct electron transfer between the proteins and the electrode is difficult because the active sites of the proteins are deeply buried in a thick protein shell, and that the large distance between the active sites of the proteins and the electrode surface will slow down the electron transfer. To overcome these drawbacks, the development of non-enzyme electrochemical sensors for detection of H_2O_2 has received great attention (Dinesh et al., 2014). As part of the solution to the demand of sensitive and selective enzyme-free based H_2O_2 sensors, we propose to develop an enzyme free sensor which requires minimal skill operation, inexpensive and that produces real time analytical results towards H_2O_2 detection.

1.3 Motivation

The fact that there are vast applications of H_2O_2, clinically, environmentally and industrially, yet, calls abounds for the development of a cheap, environmental friendly and easy to use method for its detection. Quantitative and qualitative detection of H_2O_2 has been investigated through utilization of many platforms. The preceding literature exploration showed that nanoparticle composites and graphene nanocomposites such as metal oxide graphene nanocomposites and polyoxometalates-graphene nanocomposites have been used for selective and sensitive non-enzyme electrochemical detection of H_2O_2. Even though there have not been a number of papers on these composite combined together, Nig and Jianbin constructed an enzyme free sensor based on silver-iron-oxide/reduced graphene oxide nanocomposite for the detection of H_2O_2 which proves to be very effective with the detection limit of 0.5 $\mu molL^{-1}$

(Zhang & Zheng, 2017). On the other hand Arumugan and Sambandam constructed an enzyme free H_2O_2 sensor based on silver nanoparticles embedded phosphomolybdate-polyaniline hydride (Manivel & Anandan, 2011). Cyclic voltammetry showed that the electronic properties of POM were retained even after the formation of the hybrid which led to an effective reduction of H_2O_2 with a less negative over potential. The detection limit of their sensor was estimated to be 750 nM. Incorporating POM in RGO led to an accurate, selective and sensitive H_2O_2 detection. Thus, the fabrication of Ag-Fe_2O_3/POM/RGO nanocomposite presents a novel, simple, cheap and environmental friendly method for detection of H_2O_2.

1.4 Aim and Objectives

This study will develop a synergetic electrochemical sensor based on Ag-Fe_2O_3 NPs/POM/RGO nanocomposite for the detection of hydrogen peroxide. The aim is to combine the electrochemical properties of phosphomolybdic acid and Ag-Fe_2O_3-RGO nanocomposite into a very sensitive and high selective nanocomposite that is capable of detecting H_2O_2. The main objectives of this study are as follows.

1. To synthesize the various materials for the sensor platform including RGO, Ag and Fe_2O_3 nanoparticles and investigate their surface morphology using scanning electron microscope (SEM) and transmission electron microscopy (TEM); elemental analysis using x-ray diffraction (XRD) and energy dispersive x-ray spectroscopy (EDX), also structural analysis using Ultraviolet-Visible spectroscopy (UV-Vis), Fourier Transform-Infrared Spectroscopy (FTIR) and Raman Spectroscopy.

2. Development of the Ag-Fe_2O_3 NPs/POM/RGO nanocomposite on the glassy carbon electrode and investigate the electrochemical properties of the developed platform using cyclic voltammetry (CV), amperometry (AMP) and electrochemical impedance spectroscopy (EIS).

3. To determine the potential at which H_2O_2 is reduced on the surface of the electrode using CV with different concentrations of H_2O_2.

1.5 Research Framework

Research methodology leading to final results followed consecutive steps. Below is the flow diagram showing the summary of the study objectives in line with the experimental procedure.

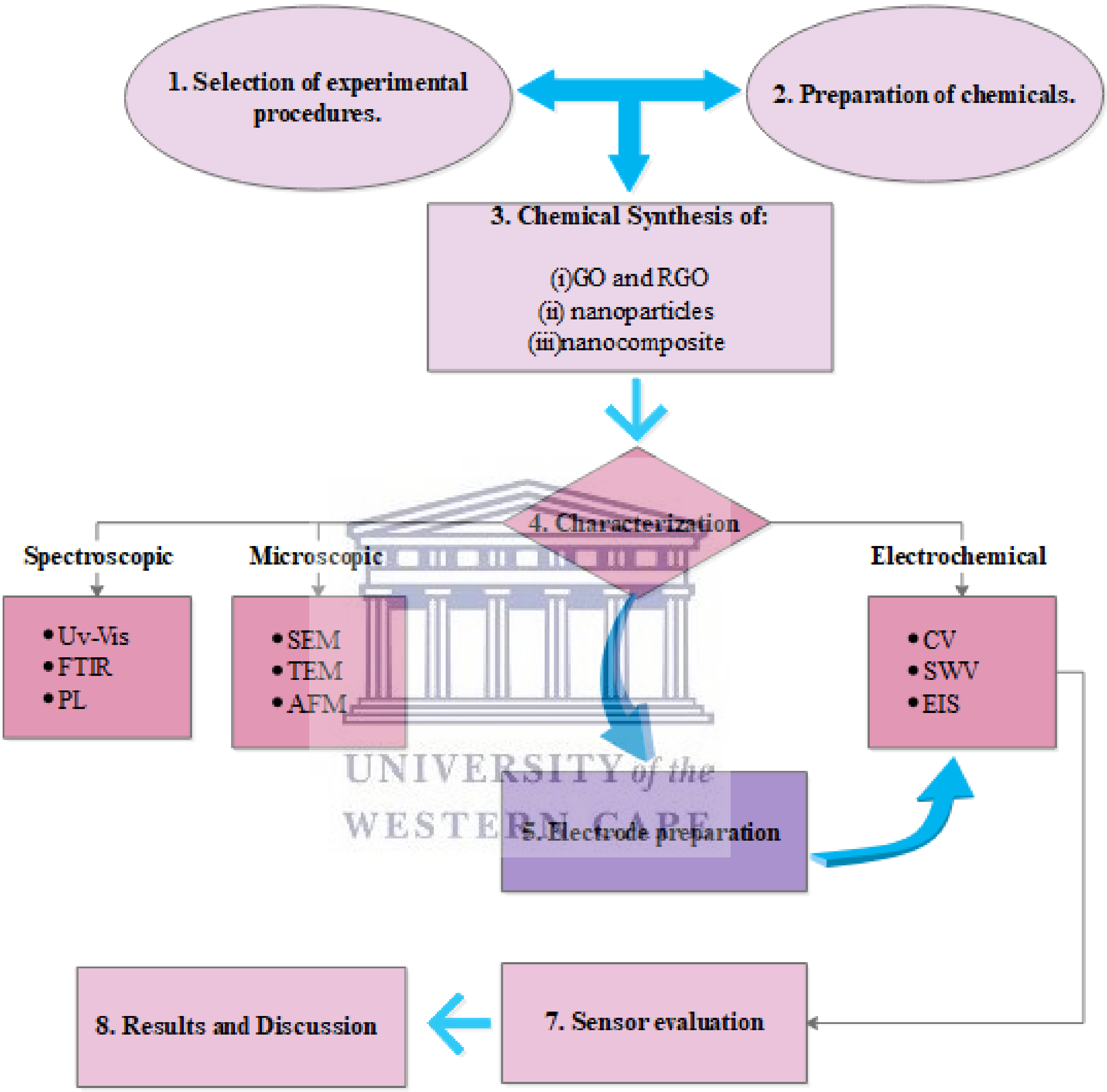

Scheme 1.1: Research framework showing the summary of the study objectives in line with the experimental procedure for the development and application of the Ag-Fe_2O_3/POM/RGO nanocomposite electrode for H_2O_2 detection.

1.6 Thesis Outline

The thesis will be presented as outlined briefly below:

Chapter 1 introduces the background and importance of the study and its objectives

Chapter 2 reviews the literature related to biosensors, graphene, POMs, nanomaterials, synthetic methods, applications and relevant research associated with the problem addressed in this study.

Chapter 3 includes information on the chemicals used, instrumentation and research design with an overview of successive steps taken to meet the objectives. Also characterization methods, such as cyclic voltammetry (CV), transmission electron microscopy (TEM) and electrochemical impedance spectroscopy (EIS) are discussed briefly in this chapter.

Chapter 4 and 5 will represent results and discussion generated from the experimental followed in chapter **3.**

Chapter 4 will mainly represent and discuss the characterization results of the developed nanocomposite**.**

Chapter 5 will discuss the enzyme-less sensor response towards the detection of H_2O_2 based on CV. A more detailed description of the enzyme-less sensor and its analytical characteristics such as linear range, stability, detection limits and selectivity is presented in this chapter. This chapter also reports the application of the sensor to real life samples.

Chapter 6 will present the conclusion, future work and recommendations.

CHAPTER 2

LITERATURE REVIEW

Chapter overview

Furnishing the sensor with high selectivity and sensitivity for analyte measurements is one of the primary goals of any sensor recognition system. Numerous materials such as POM and several classes of nanomaterials such as metals, metal oxides and carbon based materials that enhance the sensor's selectivity and sensitivity for H_2O_2 detection have been reported in the literature. These nanomaterials include graphene, iron oxide, heteropolyanions and silver nanoparticles. In most cases the reported materials work in synergy with each other leading towards electrocatalytic detection of H_2O_2. In this section the most promising materials used to fabricate sensing devices with respect to enhanced analytical properties will be reviewed.

2.1 Sensors

Since the pioneering work of Clark and Lyons on biosensors, great efforts have been devoted to their commercialization (Karunakaran, Rajkumar & Bhargava, 2015). Known as the father of the "Biosensor" concept, 62 years ago, Prof Leland C Clark published his paper on the development of an oxygen electrode which now bears his name: "Clark Electrode". The concept was demonstrated by immobilizing the enzyme glucose oxide on a Clark oxygen electrode surface using a super-permeable dialysis membrane. The addition of the glucose concentration was proportional to the decrease of the measured oxygen concentration (Mascini, 2006). 13 years later, after Clarks invention, Springs Instrumental (Yellow Springs, OH, USA) placed the first commercially produced biosensor in the market (Iqbal, Gupta & Hussaini, 2012). It was applied to a glucose assay in blood samples from diabetics (Pohanka & Republic, 2008). Since then several breakthroughs have been accomplished by other scientist in this field of sensing.

Advancements in science, technology and engineering remain the core drivers in the development of miniaturized multidisciplinary sensors. Devices that record chemical, physical, or biological changes in their environment and convert these changes into measurable signals are called sensors (Ronkainen, Halsall & Heineman, 2010). They are simple, portable analytical devices with many applications including environmental monitoring, defence, drug discovery, health care and food safety (Cosnier, 2005). Connected in series, a recognition element and transducer are usually the two main components of a sensor. While the recognition element allows selective response to a particular analyte or a group of analytes, the transducer or detector device provides the signal (Ronkainen, Halsall & Heineman, 2010). In this regard, a device that converts chemical information, ranging from composition and concentration of the relevant material via an electrical signal is called a chemical sensor (K. Ihokura, 1994). In a chemical sensor the recognition element is known as a chemical or molecular recognition system (receptor) and the transducer is a physicochemical transducer (Thévenot et al., 2001). According to the transducer's operating principle a chemical sensor can be classified into electrochemical, piezoelectric and optical sensors (Bochenkov & Sergeev, 2010).

In order to correctly use the sensor's operating system and the signal information, the nature of the signal they produce must be fully understood. Hence before discussing the main components of a chemical sensor, it is important to familiarise ourselves with the terminology around this technology. A typical chemical sensor is represented in **Figure 2.1** ; containing the following.

- ***Sample*** – It is the substance that you wish to investigate. The sample contains the analyte, probably amongst other stuff.
- ***Analyte*** – It is a substance being measured in an analytical procedure. For instance, H_2O_2 is an analyte in a biosensor that is designed to detect H_2O_2.

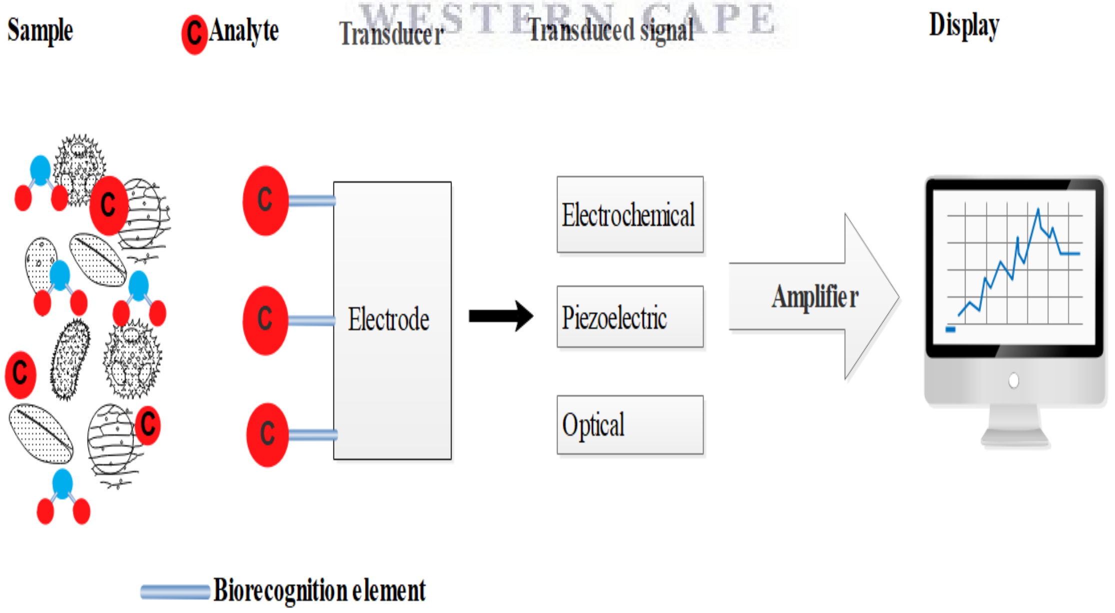

Figure 2.1: diagram of a chemical sensor

- ***Biorecognition element***

The biorecognition element of a biosensor is composed of a bioreceptor which is stuck to a matrix support on a transducer surface, translating the information from the biochemical domain into a chemical or physical output signal (Thévenot et al., 2001). The bioreceptor is carefully chosen to selectively interact and bind a target analyte from the sample. which gives rise to transduction and signal production (Munyao, 2008). Since the sensitivity and specificity of the overall biosensor depends on the bioreceptor, the bioreceptor's properties are regarded to be very important (Ronkainen, Halsall & Heineman, 2010). Furthermore the stability, orientation and the method in which the bioreceptor is immobilized onto the support matrix are also regarded to be very important (Cosnier, 2005). Bioreceptors can be classified as catalytic based (enzymes, proteins, microorganisms) and affinity based (immunesensors, DNA sensors and receptor sensors) (Subrahmanyam, Piletsky & Turner, 2002).

- ***Transducer***

The transducer is the element that converts the biological event resulting from the interaction on the bioreceptor with the analyte into a measurable signal which may be read at the signal display (Koyun, Ahlatc & İ, 1962). The transducing element of the sensor is also known as a detector, sensor or electrode but to avoid confusion the term "transducer" is preferred (Thevenot et al., 1999). As stated before biosensors can be classified based on the type of transducer and bioreceptor used, biosensors are categorized as optical, piezoelectric and electrochemical sensors (Perumal & Hashim, 2014); below is a brief description of each with emphasis on electrochemical biosensors which are the main focus of this work.

2.1.1 Types of Chemical Sensors

2.1.1.1 Optical

Optical biosensors are sensors which make use of optical principles for the transduction of biochemical interaction into a suitable output signal (To & Biosensors, 2005). The absorbed or emitted light as a consequence of a biological or chemical reaction is the main measurement technique in optical biosensors. In this biosensor, suitable detectors such as semiconductors, electrodes guide the light waves by means of optical fibres. They are advantageous in their immunity to electromagnetic interferences, capability to sense remotely and use of multiple detection in one device. However, there exist several draw backs such as instability of bioreceptor and sensitive to light. They can be used to measure pH, CO_2 or O_2 (Chaubey & Malhotra, 2002).

2.1.1.2 Piezoelectric

Piezoelectric “mechanical” transducer act by converting the physical mass on an analyte into an electrical signal. The operation principle of this type of biosensor is based on the rule of coating the surface of the biosensor with a selectively binding biologically active substance, usually a quartz-crystal coated with a gold electrode (Janshoff, Galla & Steinem, n.d.). The coated surface is then put in a solution containing analytes that stick to the binding substance. Consequently, the resonance frequency of oscillation decreases while the mass of the crystal increases proportionally. Disadvantages associated with this type of biosensor include lack or selectivity or sensitivity and interruption from the liquid media where the analysis takes place(MEHRVAR & ABDI, 2004). Examples of piezoelectric sensors include bulk wave and surface acoustic wave (Perumal & Hashim, 2014). It has been used to detect nitrous oxide, carbon monoxide, ammonia and methane (Moozarm Nia, 2017).

2.1.1.3 Electrochemical

The electrochemical biosensors are the largest and most developed class of Chemical sensors. They measure the current produced from oxidation and reduction reactions (Perumal & Hashim, 2014). In an electrochemical biosensor the transducer is made up of a metal or carbon electrode. Since the biochemical film is coated with ionic conducting, semi-conducting and electronic conducting materials, the electrochemical biosensor is considered a chemically modified electrode (Thévenot et al., 2001). The electrode itself plays a crucial role in the performance of the electrochemical biosensor, since the reactions are usually detected only in proximity to the electrode surface. Depending on the chosen function of a specific electrode, the electrochemical biosensor’s detection ability is greatly influenced by the electrode’s material, its surface modification and its dimensions. As previously mentioned, dependent on the operating transducing principle, electrochemical biosensors can be classified further classified as amperometric, potentiometric and impedimetric sensors (Bochenkov & Sergeev, 2010).

2.1.1.3.1 Impedimetric biosensor

The impedimetric biosensor follows impedance (Z) in Ohms, or its components capacitance (C) in Faraday and resistance (R) in Ohm’s. Since inductance does minimal influence in the electrochemical setup, the expression of impedance is as shown in the above **equation 2.1**:

$$Z^2 = R^2 + \frac{1}{(2fC)^2} \qquad \textbf{(2.1)}$$

For some reasons other researchers also call this system “conductometric” , since conductance is the inverse value of resistance (Iqbal, Gupta & Hussaini, 2012). This type of electrochemical biosensor detects changes in the electrical field due to a change in capacitance and electron transfer resistance at the working electrode surface arising from analyte-bioreceptor interaction. As the concentration of the analyte increases, analyte stuck to the bioreceptor increases, and successively impedance across the electrode surface changes, which is detected at the transducer (Mantzila & Prodromidis, 2005). One important advantage of these biosensors is that there is no need for electroactive specie, meaning there are no limits on analyte type. Even so there exist some drawbacks such as reproducibility, non-specific binding and high limits of detection.

2.1.1.3.2. Potentiometric biosensor

The principal phenomenon of a potentiometric sensor is the measurement of the potential difference between either two reference electrodes or an indicator and a reference electrode divided by a permselective membrane, when there is no flow of any significant current between them. Potentiometric sensors are based on ion-selective electrodes (ISE) and ion-selective field effect transistors (ISFET) (Lee, Kyu Kim & Kim, 2009). The potential difference between the indicator and the reference electrode are proportional to the logarithm of the ion activity or gas concentration, the electrode potential E, as defined by the **Equation 2.2** below (Pohanka & Republic, 2008). But this can only be true if the interesting ions have a low enough or a constant concentration and all various phase boundaries potential differences are neglected or remain constant, except at the membrane/sample-solution boundary (Thévenot et al., 2001).

$$E = E^0 + 2.303\frac{RT}{n_e F}log_{10}(a_i), \qquad \textbf{(2.2)}$$

Where E^0 (standard potential) is the constant dependent upon the type of measuring and reference electrodes being used, R is the universal gas constant (8.314 J/mol.K), T is the temperature in Kelvin, F is the Faraday constant (9.648 x 10^4 C/mol), n is the valence of the ion and a_i is the ionic activity of the ion being measured.

The ionic activity, a_i, of the solution is related to the analytical concentration, [i], by the following relationship

$$a_i = \Upsilon_i[i] \qquad \textbf{(2.3)}$$

Where Υ_i is the ion activity coefficient.

The pH electrodes are the most common potentiometric devices while several ion (F^-, I^-, CN^-, Na^+, K^+, Ca^+, NH_4^+) or gas (CO_2, NH_3) selective electrodes are also available.

2.1.1.3.3 Amperometric biosensor

Compared to potentiometric biosensors, amperometric biosensors are quite sensitive and are more suited for mass production. Measuring the current as a function of time resulting from oxidation and reduction of an electroactive species in a biochemical reaction that mainly depends on the concentration of the analyte with a fixed potential is one of the bases of an amperometric biosensor (Grieshaber et al., 2008). In this device as particular species undergo redox reactions (oxidized or reduced) at inert metal electrodes, there is a transfer of electrons from the analyte to the working electrode or vice versa. Since the direction of the electrons depends upon the properties of the analyte they can be controlled by the electric potential applied on the working electrode (Perumal & Hashim, 2014). The amperometric cell usually consists of two or three electrodes. The working electrode also known as the sensing or redox electrode, which is usually constructed from carbon (C), gold (Au), platinum (Pt), is the first electrode. The reference electrode usually made form Ag/AgCl, which has a fixed potential that controls and maintains a constant potential at a Pt, Au and C based working electrodes. A third electrode called a counter or auxiliary electrode which is sometimes included to assist in the measuring of current flow (Wang et al., 2008).

They are divided into three generations depending on the electron transfer method that is used for measuring the biochemical reaction or the degree of separation of the components of the biosensor. In all cases an enzyme is required and therefore the performance of the sensor relies on different parameters, like temperature and pH. **Figure 2.1** shows a 3rd generation Amperometric enzyme electrochemical sensor; here the biosensor depends on the bioelectrocatalysis and there is a direct electron transfer between enzyme and electrode (Rocchitta et al., 2016).

2.3 Characteristics of sensors

To characterize a sensor's performance, a set of static and dynamic parameters are used. The quality of these parameters decides the sensors effectiveness towards a particular application. For defining how accurate an output signal is employed for the description of a time varying analyte, dynamic parameters can be employed. On the other hand, static parameters are those that relate to issues such as: how a sensor's output range in response to an input change is, how selective a sensor is, or internal interferences can affect its response and how stable the operation of a sensing system can be. Below is the list of the some static and dynamic parameters and their definitions (Thevenot et al., 1999; Ronkainen, Halsall & Heineman, 2010; Bandodkar & Wang, 2014; Karunakaran, Rajkumar & Bhargava, 2015).

- **Detection Limit** – It is the lowest concentration of the analyte that can be measured under specified conditions. It is regarded as one of the most important characteristics of a sensor. A sensor that can respond to concentrations of an analyte as low as ppb levels is said to be a good sensor.

- **Selectivity** – It refers to characteristics that can decide whether a sensing system can selectively respond to a group of analytes or even more precisely for a single target analyte in the presence of other interferences. For example, an oxygen gas sensor that does not show any response to other gas species, such as carbon dioxide or nitrogen oxide, is considered a very selective sensor.

- **Sensitivity** – It is the ratio of the incremental change in the sensor's output (Δy) to the incremental change of the subject to be measured in input (Δx), i.e., the slope of calibration graph. Sometimes it is confused with the detection limit.

- **Response Time** – When a sensing system is exposed to a subject to be measured, the time required for a sensor to respond to a step concentration change from zero to a certain concentration value is the response time.

- **Recovery Time** –It defined conversely to "the response time" as the amount of time it takes for the sensor signal to return to its initial value after a step concentration change from a certain value to zero.

- **Stability** – It is a sensing system's ability to provide reproducible results for a certain period while keeping the sensitivity, selectivity, and response and recovery time.

- **Dynamic Range** – Also called the measurement range or span, the dynamic range is the analyte's concentration range between maximum and minimum values that can be measured with the sensing system i.e., the analyte concentration range between the detection limit and the highest limit concentration. It gives a meaning and accurate output for the sensor. Damage to the sensor, unacceptably large inaccuracies and unintelligible readings may be caused by signals outside of this range.

- **Reproducibility** – The ability of a sensing system to give the same response after changing the conditions of the measurement. For instance, when a sensing system shows indistinguishable responses when performed by different operators or at laboratories the system is said to be reproducible.

- **Resolution** – Strongly limited by any noise in the signal the resolution also known as the "discrimination" is the minimal concentration difference that can be distinguished by the sensor.

- **Life time** – It is the period in which the sensor will continue to work without any weakening in its performance.

2.4 Materials used for electrochemical H_2O_2 Sensor

Over the past few years, publications related to H_2O_2 enzyme-free electrochemical sensors have increased rapidly. This improvement indubitably indicates good development activities and a continuing bright future for enzyme-free H_2O_2 electrochemical sensors. Because of their desirable chemical, physical and electronic properties, unique from those of bulk materials, nanomaterials have attracted great attention in the engineering, science and technology behind the construction of these enzyme-less H_2O_2 sensors (Liu, Weng & Yang, 2017). Furthermore, the correct combination of nanomaterials with different morphologies or components has led to the remarkable progress of multifunctional nano-assembles systems. In parallel with the advancement of nanomaterial science and nanotechnology, numerous types of nanomaterials have been used for designing enzyme-free H_2O_2 electrochemical sensor including polyoxometalates, metal nanoparticles, metal oxide nanoparticles, bimetallic nanoparticles and carbon based nanoparticles. This section of the this will review this afore mentioned nanomaterials as potential materials for H_2O_2 detection (Chen et al., 2014).

2.4.1 Graphene oxide

Graphene is a very interesting material among carbon structures such as fullerenes, carbon nanotubes (CNTs) and graphite. Structurally it a single layer of carbon atoms densely packed in a honey two-dimensional 2D lattice. Compared to CNTs, it shows competitive advantages such as low cost, ease of preparation and safety. In addition, it is also an ideal platform for electrochemical research since it is free from contamination of transition metals which are apt to exist in CNTs. The graphene can be prepared by several methods with the reduction of GO being a more promising approach (Wang, Wu, et al., 2014). Different methods have been used for the synthesis of graphene oxide (GO) to reduced graphene oxide (RGO), such as thermal, electrochemical and chemical reduction (Amanulla et al., 2017). Compared to other methods, the reduction of GO by chemical route is the most widely used method for obtaining RGO. However, the major drawback of this method is that the RGO agglomerates and reverts to graphite (Kumar et al., 2018). Its unique optical, electronic, chemical and its ability to immobilize large amount of substance due to its large specific surface area offered great potential in electrochemical sensor applications (Li, Du, et al., 2010; Zhao, Zhang & Zheng, 2017). In addition, this high surface area of electrically conductive graphene sheets can give rise to high densities of attached analyte molecules. It has been reported that carboxyl-modifies GO possess intrinsic peroxide-like activity that can catalyse the reaction of peroxide substrate. This in turn can facilitate high selectivity and sensitivity in electrochemical sensors (Yusoff et al., 2017).

2.4.1.1 Graphene based H_2O_2 sensor

For developing an H_2O_2 sensor, it is an important mission to decrease the oxidation-reduction over potential. (Zhou, Zhai & Dong, 2009) characterized a chemically reduced graphene oxide (CR-GO) investigating its performance towards H_2O_2 detection. Compared to the graphite modified electrode the CR-GO modified electrode showed enhanced electron transfer rates. The oxidation/reduction of H_2O_2 started at 0.2/0.1 V (vs. Ag/AgCl), a much lower onset potential compared to the bare and the graphite electrode. The superior electrocatalytic activity of the CR-GO modified electrode was ascribed to the high density of the edge-plane like defective sites on CR-GO. (Shan et al., 2009) prepared and characterized a H_2O_2 sensor based on a PVP-protected graphene functionalized ion liquid (PFIL). The positive reduction potential (0 V) and the reduction current showed that the modified electrode by graphene showed better electrolysis that the PFIL modified electrode for H_2O_2. Due to properties such as hydrophicity and multiple oxygen moieties. These oxygen moieties allow further modification, especially with materials. Moreover, the same group modified graphene with gold nanoparticles and chitosan to construct a glucose biosensor. The resulting graphene/AuNPs/chitosan sensor showed good electrocatalytic activity towards H_2O_2. The good electrocatalytical activity might be due to the synergetic effect of graphene and the nanoparticles.

2.4.2 Metal nanoparticles

Metal nanoparticles, especially transition metal nanoparticles, are known to be good catalysts due to their ability to adopt multiple oxidation states and activate other substances in the process of adsorbing them onto their surfaces. Furthermore, owing to their nano-size, they display unique advantages of enhanced mass transport, high effective surface area, sized controlled electrical activity and effective utilization of expensive materials (Luo et al., 2006). Thus, transition metal nanoparticles can be made excellent catalysts due to their high ratio of surface atoms with free valences to the cluster of total atoms (Son & Jang, 2013). The introduction of these nanoparticles with catalytic properties into electrochemical sensors can decrease over potentials of many analytically important electrochemical reactions, and even realize the reversibility of some redox reactions, which are irreversible at common unmodified electrodes. Platinum (Pt), Palladium (Pd), Gold (Au), Copper (Cu) and Silver (Ag) are the mostly used transition metals for making nanoparticles for H_2O_2 sensing (Chen, Yuan, et al., 2013). Ag nanoparticles are cheap compared to Au nanoparticles (Li et al., 2015), therefore in this study Ag nanoparticles will be used. And we will only focus on Ag nanoparticles (AgNPs), reviewing their properties and fabrication methods for potential use as H_2O_2 sensors.

2.4.2.1 Silver nanoparticles (AgNPs)

Silver nanoparticles (AgNPs) are a class of material with size between 1nm and 100 nm (Syafiuddin et al., 2017). Even though they are called “AgNPs” some have large percentages of silver oxide (AgO) owing to their large ratio of surface to bulk silver atoms. Different shapes of these nanoparticles can be constructed depending on their application e.g. spheres, diamond shape, wires, rods, octagonal and thin sheets (Tran, Nguyen & Le, 2013; Ajitha et al., 2016). Compared to the bulk parent, AgNPs exhibit remarkable physical and chemical properties different from both the bulk and ion material (Srikar et al., 2016) such as optical, catalytic activity, high thermal and electrical conductivity, surface enhanced Raman scattering and chemical stability (Haider & Kang, 2015) . These properties sorely depend on the size, shape and morphology make them very attractive in many applications such electronics, catalysis, antibacterial agents and sensors (Zainal Abidin Ali Shamala Devi Sekaran, and R. Puteh, in press; Han & Kim, 2015; Van der Horst et al., 2015; Shaikh, Parida & Böhm, 2016). Thus control of their size, shape and morphology is of very importance. In general, this specific control often depends on varying the methods of preparation, reducing agents and stabilizers (Abou El-Nour et al., 2010).

2.4.2.1.1 Preparation

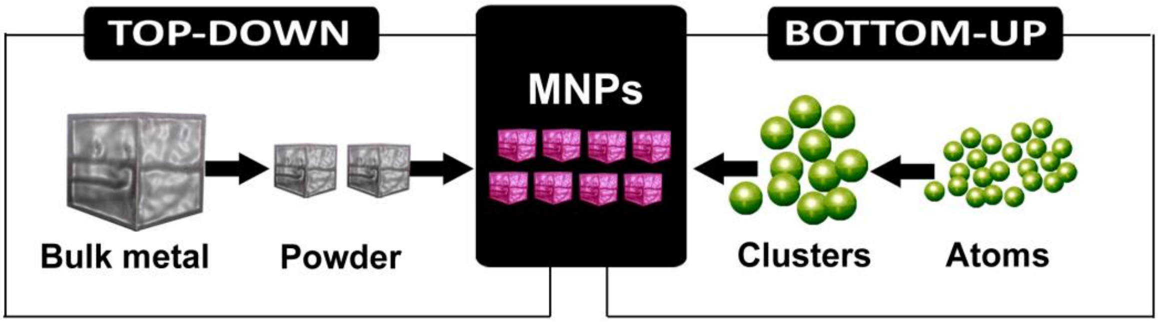

Figure 2.2: Top-down and bottom-up approaches for the synthesis of nanoparticles (https://nanografi.com/blog/metallic-nanoparticles-part-ii-top-down-and-bottomup/).

Due to the afore mentioned metal nanoparticle's interesting properties and their promising applications in different fields, many routes have been introduced for their preparation and can be grouped into "bottom up" and "top-down" approaches (Nurani et al., 2015). The former approach produces nanoparticles by build-up of material from the bottom by executing physical processes such as laser ablation, condensation and evaporation. On the other hand, the latter approach produced nanoparticles from ions, atoms and molecule by using wet chemical processes. Each method has its advantages and its drawbacks. The main merit of bottom-up approach is that homogenous nanostructures with perfect crystallographic and surface structures are achievable. While the main merit for top-down is that from a short period of time nanomaterials can be synthesised in bulky quantity (Pareek et al., 2017).

2.4.2.1.2 Ag-based H_2O_2 sensors

As typical nanomaterials, Ag nanoparticles have been extensively used to manufacture non-enzymatic H_2O_2 sensors because of their excellent catalytic activity for the reduction of H_2O_2. Previously obtained electrochemical results by other researchers show that the presence of Ag nanoparticles is responsible for the sensor response, in terms of cathodic current increment regarding the reduction of H_2O_2. (Welch et al., 2005) were able to show that modifying the glassy-carbon surface with nano-sized Ag assemblies successfully facilitates the reduction of H_2O_2.

Since size, distribution, shape, and dispersion of Ag nanoparticles play a vital role in the sensor performance, several methods have been used in order to synthesise the desired Ag nanoparticles (Zhao et al., 2009). Among these methods, hydrothermal technology has been a promising and attractive route for synthesising Ag nanoparticles since it is able to provide monodispersed nanoparticles with well control over their size and shape along with their chemical homogeneity. Additionally, to obtain the desired physicochemical properties, protective agents, surfactants, polyelectrolytes or polymers are often used in conjunction with the hydrothermal method (Ajitha et al., 2016). For example, (Yi et al., 2011) used the hydrothermal process to synthesise novel nano-porous Ag particles through the reduction of Ag^+-EDTA complex by polyethylene glycol as the reducing agent for electro-reduction of H_2O_2 in alkaline media. On the other hand, (Lu et al., 2011) used a facile hydrothermal synthesis process without the extra introduction of other reducing or protective agents to prepare well-stable Ag nanoparticles with diameter of 5 nm from an aqueous solution $AgNO_3$ and poly [(2-ethyldimethylammonioethyl methacrylate ethyl sulfate)-co-(1-vinylpyrrolidone)] (PQ11). From their report it was discovered that stable Ag nanoparticles-embedded films on a bare electrode surface can arise from such dispersions and these nanoparticles show remarkable catalytic performance for the detection of H_2O_2.

Recently, a variety of Ag nanoparticles based nanocomposites have been prepared through the chemical reduction of silver ion to construct H_2O_2 sensor, including graphene-Ag nanoparticles, polyaniline-Ag nanoparticles, carbon nanotubes-Ag nanoparticles, Iron Oxide-Ag nanoparticles, multi-wall carbon nanotube (MWCNT)-Ag nanoparticles and single wall carbon nanotubes (SWCNT)-Ag nanoparticles (Zhao et al., 2009; Lorestani et al., 2015; Qi & Zheng, 2016; Sang et al., 2017; Kumar et al., 2018). Using a simple one-step hydrothermal method without a reducing agent, Lorestani and team (Lorestani et al., 2015) were able to fabricate a novel sensing composite of Ag nanoparticles-reduced graphene oxide (RGO)-carbon nanotube (MWCNT). It was found that a uniform distribution of the nanosized Ag nanoparticles can be achieved using silver ammonia complex as the precursor instead of commonly using the $AgNO_3$. The composite exhibited excellent electro catalytic activity for the reduction of H_2O_2. An interesting work was reported by Sun and colleagues (Tian, Liu & Sun, 2010) where the preparation of supramolecular micro fibrils of o-phenylenediamine (OPD) dimers was based on the oxidation of OPD monomers by $FeCl_3$. The subsequent treatment of such micro fibrils with $AgNO_3$ aqueous solution transforms them into nanofibers decorated with spherical Ag nanoparticles with sizes in the range of 5-20 nm leading to a non-enzymatic H_2O_2 sensor. After He and colleagues proved electrochemical deposition to be the least expensive, highly productive and readily adoptable method to synthesise Ag nanoparticles, it has been used to synthesise Ag nanoparticles for H_2O_2 sensors. A novel H_2O_2 sensor was developed by electrodepositing Ag nanoparticles on a glassy carbon electrode modified with three-dimensional DNA networks by Kang and his team. The electrochemical results showed that such sensor had favourable catalytic ability to reduction of H_2O_2. The hybrid nanoparticles exhibited a narrow size distribution (Cui et al., 2008). Bui and colleagues (Bui et al., 2010) reported using an electrochemical deposition method to pattern Ag nanoparticles on flexible transparent SWCNT films. The patterned Ag nanoparticles were then used as electrodes to detect H_2O_2.

Besides electrodeposition and chemical reduction methods, many other methods have been used to prepare Ag nanoparticles, such as UV irradiation method, microwave assisted reduction method, chemical plating method and green synthesis of Ag nanoparticles. For example, in a study conducted by Vasileva and his team (Vasileva et al., 2011), a green approach was used to prepare stable and uniform starch-stabilized Ag nanoparticles with an average diameter of 14.4±3.3 using ultrasound mediated reduction of $AgNO_3$ by $_D$-glucose. These nanoparticles exhibited a catalytic activity in the reduction of H_2O_2. The feasibility of the non-enzyme H_2O_2 sensor was exhibited in all these works.

2.4.3 Metal Oxide nanoparticles

Currently, the group of the most important nanomaterials includes simple metal oxides such as titanium oxide (TiO_2), zinc oxide (ZnO), copper oxide (CuO), magnesium oxide MgO, aluminium oxide (Al_2O_3), manganese oxide (MnO_2) and iron oxide (Fe_3O_4, Fe_2O_3) (Chen et al., 2014). These are finding increasing application in many fields of science, engineering and technology industries. They are used in photocatalytic treatment of wastewater and pesticide degradation (TiO_2), in rubber and textile industries (ZnO), in medical applications (CuO, Fe_2O_3), for the removal of dyes from aqueous solutions (Al_2O_3), in lithium-ion batteries and sensors (MnO, Fe_2O_3,Fe_3O_4) (Chen et al., 2005; Mital & Manoj, 2011; Liu et al., 2013; Kołodziejczak-radzimska & Jesionowski, 2014; Dhawale, Khobragade & Kulkarni, 2018; Khatoon, Mantravadi & Nageswara, 2018). Due to their limited size and high density of edge surfaces, oxide nanoparticles display exceptional physicochemical properties. Particle size, morphology, crystalline structure of any nanomaterial strongly influences the use and performance of the material for different properties and applications. Therefore, developing methods for the synthesis of metal oxide nanoparticles, where there is control over particle size and crystalline structure of the products is very important. Preparation methods are the first prerequisite for any novel nanoparticulated metal oxide. Methods for synthesising metal oxide nanoparticles are divided into three main groups: solution-phase (e.g. co-precipitation, sol-gel, micro emulsion, hydrothermal/solvothermal), solid-state (e.g. milling and precipitation) and lastly vapour-phase methods (e.g. spray pyrolysis and flame or plasma based methods) (Smith et al., 2015). As previously stated, each method has its merits and demerits.

In summary, uniform metal oxide nanoparticles with excellent control over particle, size distribution, dispersion and morphology can be produced by solid-phase methods, particularly those that employ surfactants or non-aqueous solvents. Nonetheless, organic impurities can be a problem and for certain applications (e.g. sensing) the capping agents are a complication that needs to be removed in order to access the oxide surface (Marcos Fernández-Garcia, 2007). To produce industrial quantities solution-state methods are favoured because of their cheap, fast and easily scaled protocols. However, these methods (milling or sonication) can also introduce impurities as well as cause strain on the crystalline structure. Lastly, vapour-phase methods are very successful when it comes to synthesizing one dimensional nanostructures but they are very costly when it comes to equipment and the energy needed to vaporize the reagent. Basically, no technique is the best for every application, most routes are successful for certain applications and certain nanomaterial (Corr, 2014). Equipment also plays a vital role for synthesis of specific metal oxide nanoparticles and in some cases it can be a challenge. In this study, hydrothermal synthesis was used to synthesize the desired material. Hydrothermal method falls under the solution-phase method. This method involves thermal decomposition of metal complexes from high temperatures either by boiling in inert atmosphere or using a sealed reactor usually an autoclave, with the help of pressure. Advantages of the hydrothermal process include low cost, mild reaction condition and easily controlling the device by changing experimental parameters such as pressure, temperature and time. However, these nanoparticles suffer from strong aggregation during synthesis and since high temperatures and pressures are used, the risk of solid state fusion in addition to agglomeration is high .To control the particle size growth and agglomeration, suitable surfactants are usually added to the reaction media in order to improve the hydrothermal process (Guo et al., 2015).

2.4.3.1 Iron oxide nanoparticles: Introduction and properties

Ferric irons or iron (III) oxides are the most important iron ores in industry. They are basically composed of iron (Fe), oxygen (O) or/and hydroxide (OH) but vary in valency of iron and crystalline structure. Ferric iron has four polymorphs, two of them are found in nature as minerals hematite (α-Fe_2O_3) and maghemite (γ-Fe_2O_3), but the other two can be synthetic nanoparticles (β-Fe_2O_3, ε-Fe_2O_3) each polymorph unique from the other in terms of structure, properties making them suitable for specific applications (Saragi et al., 2017). For example, hematite (α-Fe_2O_3) is the most stable with rhombohedral structure, low cost, high resistance to corrosion, non-toxic and environmentally friendly. It also possesses n-type semiconducting properties with 2.1 eV band gap and its weakly ferromagnetic. The magnetic properties of hematite systems relay on pressure, particle size and magnetic intensity (Jayanthi et al., 2015). Hematite nanoparticles have been applied in sensor, catalysis and batteries because of these afore mentioned properties (Kopanja et al., 2016).

As typical metal oxide nanoparticles hematite nanoparticles can be synthesised as mentioned above. For example (Lassoued et al., 2017) synthesized hematite nanoparticles using the co-precipitation method. These nanoparticles resulted in particle size of 21 nm, this was achieved when very low concentrations of the precursor were 0.05 M. On the other hand, using the hydrothermal method (Pervaiz, Gul & Anwar, 2013) synthesised hematite nanoparticles with particle size ranging from 50-100 nm. Fe_2O_3 nanoparticles suffers from a number of demerits for example, relatively low electron transfer rates and low conductivity, both which could significantly affect its activity. Preparing Fe_2O_3 nanoparticles in the use of conducting supports have been the only alternative. Lately, effort has been made on the study of hematite composites blended with metals or other meta oxides, since this may produce new or/and enhanced materials with novel physicochemical that could not be achieved by either material alone, yielding novel performances in many applications. For example, (Liu et al., 2015a) synthesised Fe_2O_3-RGO hybrid material using a one pot hydrothermal method for the removal of malachite green (MC) in water. The excellent capacity of Fe_2O_3-RGO to remove MG from water is ascribed to the synergetic adsorptive effect between Fe_2O_3 (15 nm diameter) and RGO. Among these hematite composites, bifunctional noble metal/iron oxides has also raised attention with potential applications, such as Ag-Fe_2O_3 nanoparticles (catalysis and antibacterial applications) (Gao, Chen & Jiang, 2013; Kumar et al., 2017). In a study to investigate the electrocatalytic properties of Ag-Fe_2O_3 nanoparticles, (Pan, Tang & Chen, 2013) used a hydrothermal method to synthesised Ag-Fe_2O_3 nanoparticles for p-nitrophenol detection. The results showed an enhanced catalytic performance in comparison with the bare GCE. Moreover, p-nitrophenol could be reduced at lower peak potentials on the GCE modified with Ag-Fe_2O_3 nanoparticles. Even though there are a number of applications reported on Fe_2O_3 nanocomposite, this thesis will only focus on hematite based sensors for the detection of H_2O_2 species.

2.4.3.2 Fe_2O_3 nanoparticle based H_2O_2 sensors

As previously stated that Fe_2O_3 nanoparticles suffer from low electron transfer rates and low conductivity, this demerit can hinder its application as the H_2O_2 sensor. To avoid this (Wang, Shen, et al., 2014) used a hydrothermal method to decorate Fe_2O_3 with average size of 21 nm on RGO sheets without adding any reducing agents for H_2O_2 detection. Electrochemical impedance spectroscopy (EIS) and linear sweep voltammetry were used to investigate the electrochemical performance of Fe_2O_3/RGO. In the presence of H_2O_2, this composite exhibited notable catalytic reduction at -0,22 V vs Ag/AgCl and showed no response in the absence of H_2O_2, indicating catalytic reduction of H_2O_2. In contrast the bare Fe_2O_3 nanoparticles and RGO showed very low activities under the same conditions. EIS was employed to prove electron transfer kinetics of the ferric hybrids, the semi-circular for Fe_2O_3/RGO compared to Fe_2O_3 nanoparticles, almost similar to that of RGO. This indicated that the electron transfer performance of the ferric hybrid was significantly enhanced, which could make the catalytic reduction of H_2O_2 much easier and more efficiently than Fe_2O_3 without RGO supports. This sensor had a detection limit of 1 μM and a high sensitivity of 129.9 ($\mu A/Mm/cm^2$). Also using the hydrothermal method (Zhang & Zheng, 2017) were able to successfully disperse AgNP onto the Fe_2O_3/RGO composite to yield Ag-Fe_2O_3-RGO nanocomposite for the detection of H_2O_2. Electrochemical investigations indicated that the obtained Ag–Fe_2O_3–RGO nanocomposites had excellent electrocatalytic performance toward H_2O_2 reduction. The linear range for H_2O_2 was estimated to be from 1.6×10^{-6} to 5.7×10^{-2} mol L^{-1} with a sensitivity of 50.8 $\mu A\ mM^{-1}\ cm^{-2}$ and a detection limit of 0.5 $\mu mol\ L^{-1}$.

2.4.4 Polyoxometalates

2.4.4.1 Classification and Historical Background

Polyoxometalates (POMs), are a class of nanometre sized inorganic polyanions mainly formed from oxides of molybdenum (Mo), tungsten (W), vanadium (V) and less frequently tantalum (Ta), niobium (Nb) or a mixture of these elements in their high (configuration d0 or d1) oxidation states (Mercier et al., 2015). Depending on their chemical composition, POMs can be split into three broad classes (Ammam, 2013):

a) Heteropolyanions (HPAs), with general formula $[X_xM_mO_y]^{q-}$ (x $\leq$ m)

b) Isopolyanions (IPAs), with general formula $[M_mO_y]^{p-}$,

c) Molybdenum-brown (Mo-brown) and Molybdenum-blue (Mo-Blue) reduced POM clusters

Where metal M, also called addenda atom or polyatom, is positioned at the centre of the polyhedral (formed by the addenda atom coordinated by the oxygen ligands (O)), MO_x, and the polyhedra are all bonded together through their corners or their edges and seldom their faces (Mallick, Rana & Parida, 2012). Because they are composed of only one metal type and oxygen atoms with no internal heteroanion/heteroatom, IPAs are much unstable than HPAs counterparts. Despite that, IPAs also possess fascinating physical properties such as high charges, making them attractive units for use as building blocks. Related to Molybdenum blue type species, the composition of Mo-Blue or Mo-brown, first reported in 1783 was greatly unknown until 1995, where a very high nuclearity cluster (Mo_{154}) with a ring topology was synthesised and characterized structurally by Muller *et al*. Varying the pH and augmenting the number of reducing agent along with the inclusion of a ligand like acetate facilitated the formation of Mo_{132}, a spherical ball-like cluster. As a result, one of the most thrilling advances in POM chemistry with potential spin-off application in nanoscience are represented by this high reduced POM clusters. For HPAs, the polyhedra are assembled around a heteroatom, X, usually, heteroanions such as SO_4^{2-} or PO_4^{3-} with their symmetry following that of the central heteroatom. They possess Keggin $[XM_{12}O_{40}]^{2-}$and Wells-Dawson $[X_2M_{18}O_{62}]^{4-}$anion structures and are the most reported and explored class of POMs (Chen & Barteau, 2016). They are attractive units for building blocks due to the fact that they have high charges and strongly acid surfaces (Gupta, Aberg & Carrizosa, 2017).

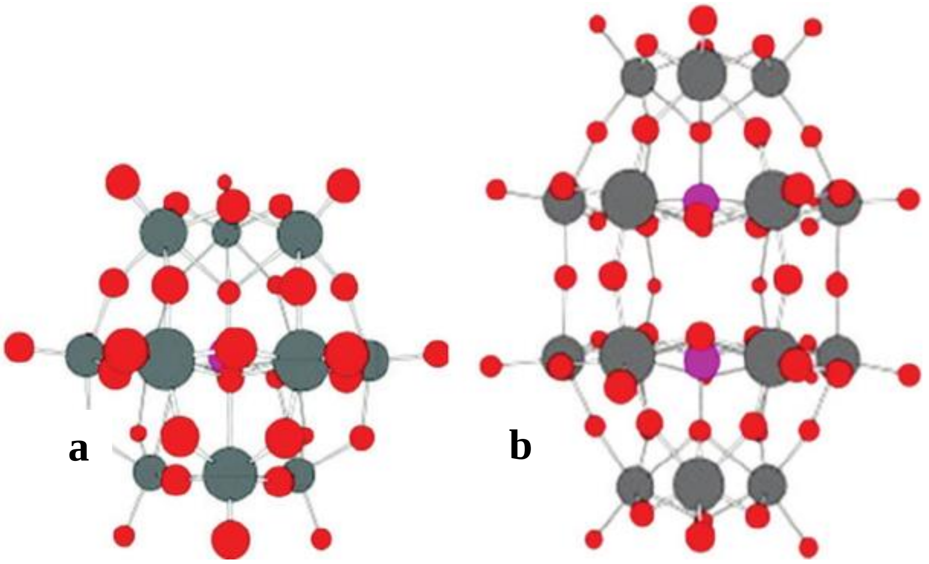

Figure 2.3 : stick and ball presentation of the two most reported and explored HPAs, namely (a) Keggin $[XM_{12}O_{40}]^{2-}$ and (b) Well-Dawson $[X_2M_{18}O_{62}]^{4-}$. Where the magenta, red and grey balls represent the heteroatom, oxygen atoms and the addenda atoms respectively (Ivanova, 2014).

Historically, the first report of POM, the phosphomolybdate, dates back to the work of Berzelius, who in 1826 recognised the formation of ammonium salt of $[PM_{12}O_{40}]^{3-}$, a light yellow crystalline solid from the reaction of ammonium molybdate $(NH_4)_2MoO_4$ with an excess of phosphoric acid (Pope & Müller, 1991). Following Berzelius initial report, Svanberg and Struve used this compound for the determination of phosphorus in analytical chemistry in 1848. In 1862, Marignac discovered the first heteropolytungstates and provided analytical composition of the 12:1 heteropoly species. Although hundreds of polyoxometalates were synthesised during the next half-century, little progress was made in understanding their structures. It was Keggin who in 1933 solved the structure of the related anion $[PW_{12}O_{40}]^{3-}$ by powder x-ray analysis which now bears his name (Poblet, López & Bo, 2003) . Since then, a range of different types of POMs have been synthesized including Lindqvist ($[M_6O_{19}]^{n-}$), Anderson $[xM_6O_{24}]^{n-}$, Dawson $[XM_{18}O_{62}]^{n-}$, Waugh $[X^{n+}M_9O_{32}(10-n)^{-}$ structures. However, Keggin and Dawson structures are the most widely used anion clusters as shown in **Figure 2.3**. And in this thesis we will only focus on a Keggin type and try to review details of its structure and physicochemical properties. Examples of Keggin type HPAs include 12-phosphotungstic acid, 12-silicomolybdic acid, 12-silicotungstic and in this thesis 12-phosphomolybdic acid was used.

2.4.1.2 Keggin anion structure

As already stated in section 2.4.4.1, the Keggin ion has the general formula $[XM_{12}O_{40}]^{2-}$, featuring tetrahedral anion XO_4 surrounded by twelve edge- and corner-sharing octahedra, MO_6 (M= Mo or W) with a diameter of 1.2 nm. The Keggin structure has four different types of oxygen atoms as shown in **Figure 2.4** (Ivanova, 2014). The four central oxygen (O_a) atoms X-O-M, two bridging types (O_b and O_c): (O_c) twelve edge-bridging oxygen atoms that bridge two Mo atoms sharing a central oxygen atom (M-O-M), (O_b) twelve corner-bridging oxygen atoms that bridge Mo not sharing a central oxygen atom and lastly twelve terminal oxygen atoms (O_d) bound to a single Mo atom (M=O). The bonds display distinctive infrared bands around 500 to 1100 cm^{-1} range (Gumerova & Rompel, 2018).

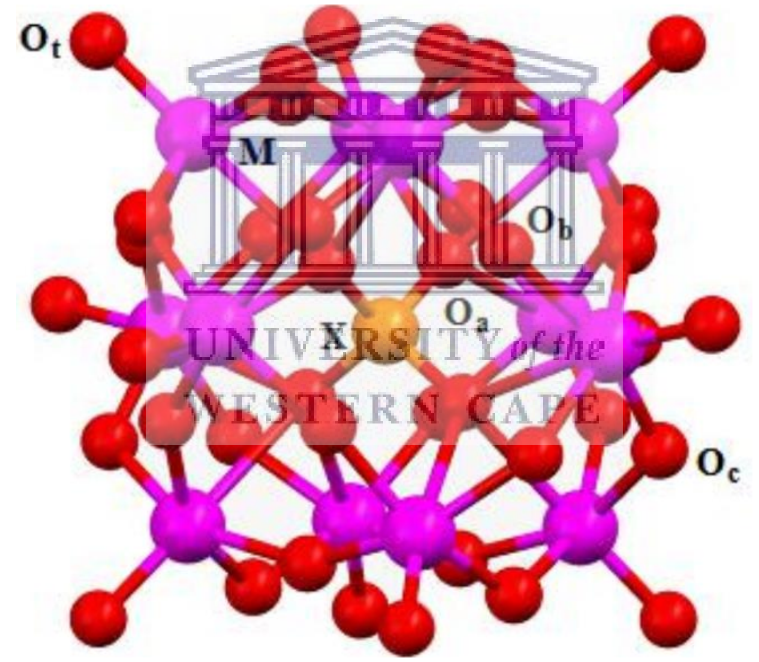

Figure 2.4: Ball and stick representation of Keggin anion (Red: Oxygen, Magenta: addenda atom, orange: heteroatom).

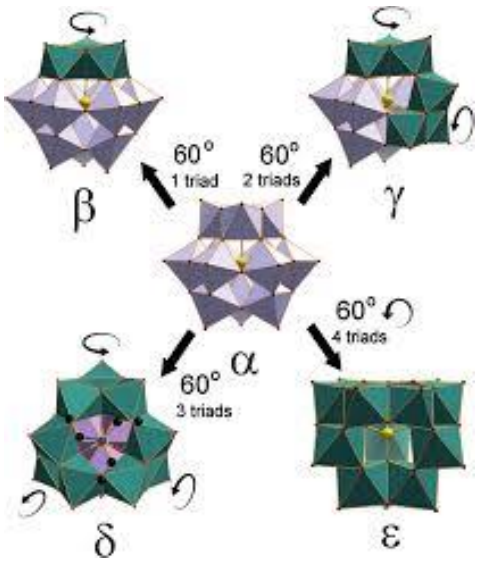

Figure 2.5: Polyhedral representation of the crystal structures of all the isomers of the Keggin anion: (α, β, γ, δ and ε isomers). The green polyhedral shows the M_3O_{13} units, rotated 60 with respect to α-isomer. The yellow spheres represent the heteroatom and the red spheres are oxo-ligands. The coordinating ligands allowing the formation of the d isomer are represented by the black ball and blue stick (Sartzi et al., 2015).

Interestingly, this arrangement permits the formation of the structural isomers with the α-Keggin ion, being one of the five isomers as demonstrated in **Figure 2.5** which then undergoes a 60° rotation of one, two, three and four M_3O_{13} triads to give respectively give the β, γ, δ and ε isomers respectively (López et al., 2001). This rearrangement of the triads affects the overall atomic and electronic structure and electrostatic repulsion between these units. However, due to the number of edge-sharing octahedra increasing these structures are energetically unflavoured. As a result, the most commonly found Keggin structure is the α–isomer with only few examples of the energetically favoured β, γ, δ and ε isomers. Due of the number of possible isomers and the dissimilarity of addenda and heteroatoms, structural and compositional control can obviously be achievable; these aspects make Keggin anions attractive compounds for studies ranging from acidity and catalysis to electrochemistry and redox activity.

2.4.4.3 Properties and Applications of HPAs

The size, composition, structure and charge diversifications of POMs has led to numerous properties. For example, HPAs such as 12-phosphomolybdic acid and 12-silicotungstic are very strong acids in aqueous solution. In a study conducted by Kulikov *et al* it was found that the acidity of 12-phosphotungsteric acid is stronger than that of unusual minerals (H_2SO_4 and $HClO_4$) (Petit & Bandosz, 2009). Because of this, POMs are used in homogenous catalyst reactions. Another most important property of HPAs is their flexible redox properties and their structures can remain unchanged after a multi-electron redox process (Yokuş et al., 2016). The electrochemical behaviour of POMs in acidic media involves one or two electron reversible reductions to produce reduced POMs, or so-called heteropoly blues owing to their changed colour (Yola et al., 2015). In reduced forms, their electron and proton transfer and/or storage abilities make them act as efficient donors or acceptors of several electrons without structural change (Zhang et al., 2012). However, bulk form of Keggin heteropoly acids have limited number of catalytic applications since they are associated with certain drawbacks. Pure HPAs have high water solubility and very low surface areas (as low as< 10 m^2/g), which hinders accessibility to their strong acidic sites limiting their stability and catalytic activities (Kim & Shanmugam, 2013). Numerous research studies on the electrochemistry of immobilizing HPAs on solid supports indicated that the physicochemical properties HPAs are retained after immobilization. Hence immobilizing or dispersing them onto various supports or entrapping them into various matrices such as nanoparticles, polymers and carbon based materials is expected to increase the number of active centres and improve their catalytic activity resulting in new or enhanced modified electrochemical properties for potential use in the sensing industry (Chi & Dong, 1995; Kang et al., 2009; Li, Zhang, et al., 2010; Zhou & Han, 2010; Lin, Hu & Song, 2017). For example, (Zhang et al., 2012) prepared GO nanosheets and POM such as $H_3PW_{12}O_{40}$ (PTA) into a multilayer film via a layer-by-layer inkjet printing method. The PTA/GO chemical sensor displayed good electrocatalytic activity for the oxidation of Dopamine. On the other hand, (Chen, Liu, et al., 2013) used a photochemical reduction method to construct a $H_3PMo_{12}O_{40}$ (PMoA)-RGO nanocomposite to investigate its electrocatalytic activity in acid solution. The electrochemical properties investigated through cyclic voltammetry indicate that the PMoA-RGO modified glassy carbon electrode has high electrocatalytic activity via a fast, surface-controlled electron transfer process. The results indicated that the introduction of RGO not only increased the electroactive surface area but also facilitated the electron transfer due to its high electric conductivity. Even though there are a number of sensing application reported on HPAs for different analytes, this thesis will only focus on Keggin ion-based sensors that are devoted to the detection of H_2O_2 species.

2.4.4.4 POM based H_2O_2 sensor

As previously stated above, one of the methods of modifying HPAs is to support them on high surface area or neutral acidic media. In this this regard, the group of (Haghighi, Hamidi & Gorton, 2010) formed a robust and stable film containing 1:12 phosphomolybdic acid (PMo_{12}) and n-octylpyridinum hexafluorophosphate ([C_8Py][PF_6]) on a modified multi wall carbon nanotube glassy carbon electrode (GCE/MWCNTs) through a dip-coating procedure for the detection of H_2O_2 and Iodate. In this study, cyclic voltammetry was used to examine the electrocatalytic activity of this composite. The GCE/MWCNTs/[C_8Py][PF_6]-PMo_{12} exhibited good electrocatalytic activity towards H_2O_2 reduction but there was no response observed on GCE/MWCNTs/[C_8Py][PF_6] for H_2O_2. The catalytic effect appeared on the reduction peak of the second redox pair (II–II) of PMo_{12}, which corresponds to the reduction process from two-electron to four-electron reduced species. The modified electrode showed the ability for hydrogen peroxide and iodate detection at reduced overpotential with many desirable properties including low detection limit, high sensitivity, short response time (<2 s) and satisfactory linear concentration range. The main limitation of the proposed electrode, which is common in the most POM-modified electrodes, is the loss of its stability and catalytic activity at pH around 7 as polyoxometalates decompose normally very rapidly above pH 3. This drawback limits the utilization of POM-modified electrodes for the fabrication of biosensors where biological elements such as enzymes are used. Shown below are the three pairs of redox peaks i.e. (I–I), (II–II) and (III–III) corresponded to the oxidation and reduction of PMo_{12} through two-, four- and six-electron processes, respectively.

$$PMo_{12}O_{40}^{3-} + 2e^- + 2H^+ \rightarrow H_2PMo_{12}O_{40}^{3-} \qquad \textbf{(2.4)}$$

$$H_2PMo_{12}O_{40}^{3-} + 2e^- + 2H^+ \rightarrow H_4PMo_{12}O_{40}^{3-} \qquad \textbf{(2.5)}$$

$$H_4PMo_{12}O_{40}^{3-} + 2e^- + 2H^+ \rightarrow H_6PMo_{12}O_{40}^{3-} \qquad \textbf{(2.6)}$$

(Yang et al., 2016a) through a simple manner constructed POM-g-RGO nanohybrids by mixing a highly efficient electrocatalytic polyoxometalate (POM) namely phosphomolybdic acid hydrate ($H_3PMo_{12}O_{40}$) with polymetric ionic liquid functionalized (PIL)-RGO for the electrochemical detection of H_2O_2 and glucose. CV measurement where used investigate the electrochemical behaviour of this nanohybdrid using 0.5 M H_2SO_4 as an electrolyte. Compared to the PIL-RGO which had no peaks, the POM-g-RGO showed an increased current response on increasing the scan rate and had three pairs of well-defined redox peaks.

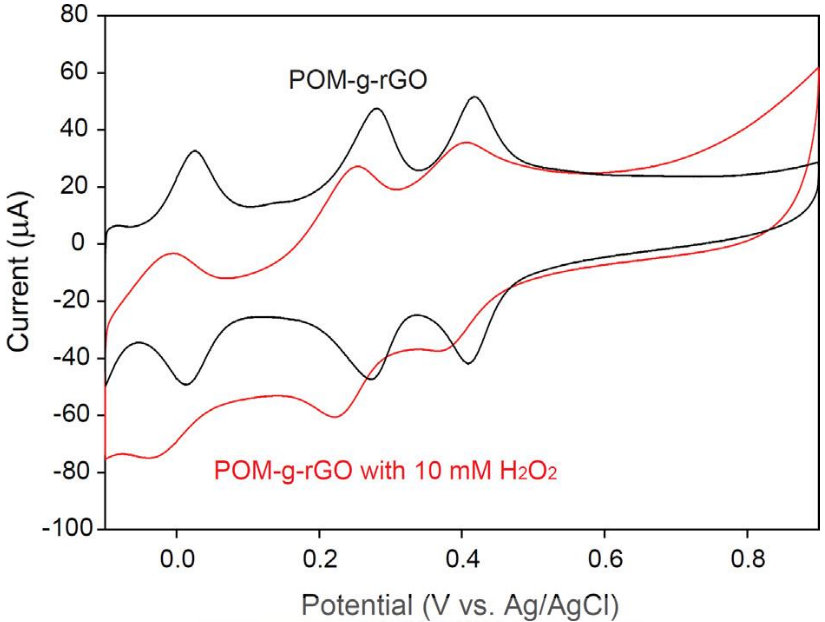

Figure 2.6: CV curves of POM-g-rGO electrode at scan rate of 50 mV/s in absence and presence of H_2O_2 (Yang et al., 2016b).

This behaviour was due to the efficient and fast charge transfer between rGO and POM. This nanohybrid was incorporated into a flow-injection device to evaluate the electrocatalytic reduction of H_2O_2 in the presence and absence of 10 mM H_2O_2. The electrocatalytic of reduction mechanism of H_2O_2 was as follows:

$$H_2O_2 + e^- \rightarrow OH_{ad} + OH^-$$

$$OH_{ad} + e^- \rightarrow OH^-$$

$$2OH^- + 2H^+ \rightarrow 2H_2O$$

When H_2O_2 was introduced, the POM-g-rGO showed an increase in cathodic reduction peak which indicated a high electrocatalytic ability of POMs in POM-g-RGO. In particular, the POM-g-RGO had a 5s response time with high sensitivity of 95.5 (μA/Mm/cm^2) and had a large range of detecting limit (100 μM – 20 μM). Furthermore, the distribution of the POM on rGO Surface was found to permit the multiple reversible redox reaction. Hence introduction of the POM onto the RGO makes this sensor's electrochemical performance an excellent and developmental candidate for different types of electrochemical sensing.

CHAPTER 3

EXPERIMENTAL & PROCEDURE

Chapter review

This chapter starts by outlining the chemicals used to construct the Ag-Fe_2O_3/POM/RGO composite. It further discusses in detail the experimental procedures involved in the fabrication of the materials namely, AgFe_2O_3 nanoparticles, POM/RGO nanocomposite, RGO, GO and the novel Ag-Fe_2O_3/POM/RGO composite. It then closes with a summary of the instrumentation and experimental techniques used to characterize the synthesized materials.

3.1 Materials and Chemicals

The list of chemicals used vis-a-vis their molecular formula, % purity and the manufacturer is presented in **Table 3.1**

Chemical Compound	Molecular Formula	Purity (%)	Company
Graphite powder	C	Extra pure	Merck Pty(LTD)
Sulphuric Acid	H_2SO_4	95.0 -98.0	Sigma Aldrich
Potassium Permanganate	$KMnO_4$	≤ 99.9	Sigma Aldrich
Hydrogen Peroxide	H_2O_2	30	Sigma Aldrich
Sodium Borohydride	$NaBH_4$	≤ 99.9	Fluka Analytical
Ethanol	C_2H_5OH	99.9	Kimix
Acetone	$CH_3{\cdot}CO\ CH_3$	99	Kimix
Silver nitrate	$AgNO_3$	99.0	Sigma Aldrich
Polyvinyl Alcohol	$(C_2H_4O)x$	-	Sigma Aldrich
Isopropyl	C_3H_8O	-	Sigma Aldrich
Ethylene glycol	$C_2H_6O_2$	99.8	Sigma Aldrich
Phosphomolybdic acid hydrate	$H_3Mo_{12}O_{40}P{\cdot}xH_2O$	-	Sigma Aldrich
Ferric chloride	$FeCl_3{\cdot}6H_2O$	99	Kimix
Urea	CH_4N_2O	95	Fluka Analytical
Nafion® 117 sol	-	5	Aldrich chemical
Potassium Bromide	KBr	-	Sigma Aldrich
Potassium Chloride	KCl	-	Sigma Aldrich

3.2 Cell setup and Synthesis

3.2.1 Cell arrangement

Figure 3.1 shows pictures of (a) coiled platinum wire used as a counter electrode, (b) a glassy carbon electrode (3 mm diameter) used as a working electrode, (c) a Silver/Silver Chloride electrode saturated (SSCE) in a 3 M Potassium Chloride solution used as a reference electrode and (d) a three electrode electrochemical cell setup used in this study. These electrodes were purchased from a company called BASS (Analytical Instruments, USA). Cyclic voltammetry (CV), electrochemical impedance spectroscopy (EIS) and amperometry (AMP) measurements were performed using Palms Sens working station (Bioanalytical Systems, USA).

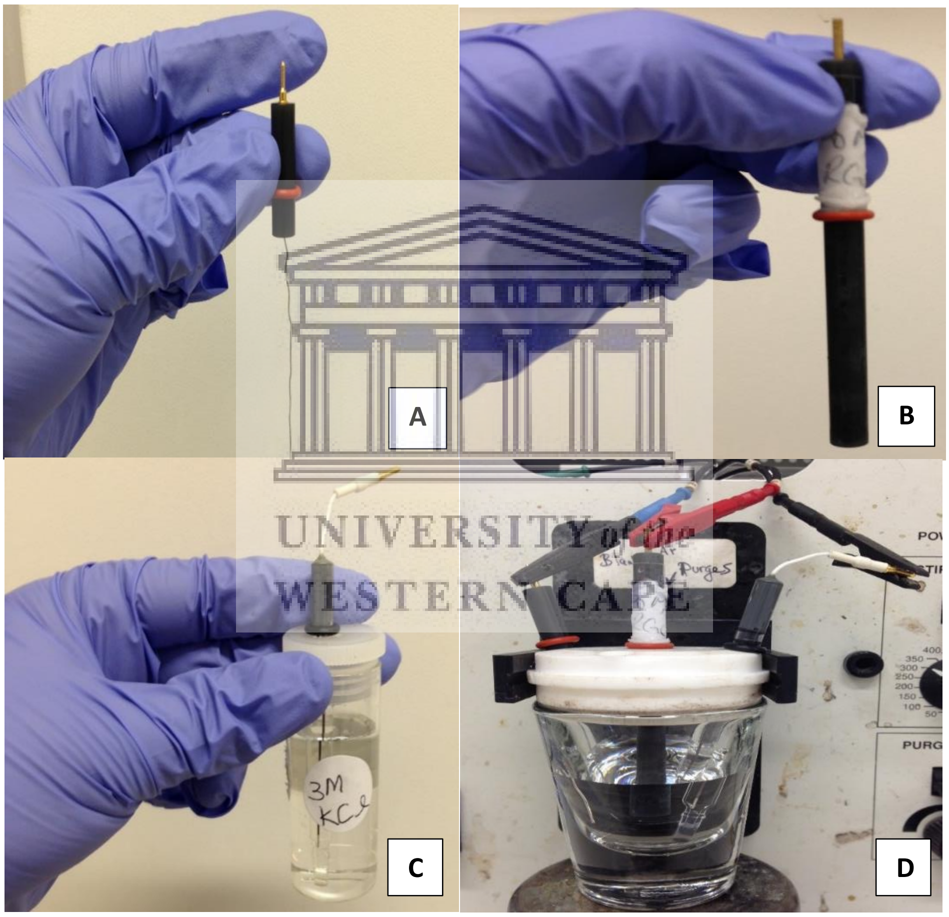

Figure 3.1: Pictures showing the assemblage of electrodes and the electrochemical cell system. (a) coiled platinum wire, (b) a glassy carbon electrode (3 mm diameter) u, (c) a SSCE (Silver/Silver Chloride electrode) and (d) a three electrode electrochemical cell setup used in this study

3.2.2 Preliminary treatment of the electrode

The surface of the bare glassy carbon electrode was polished prior to fabrication, in order to remove any traces which may affect the rate of electron transfer. Mechanical polishing is the most common method in which a micro cloth (brown soft velvety texture) is used with 0,05, 0,3 and 1 µm alumina polishing powders respectively. The electrode is placed face down on the micro cloth pad, using a smooth, circular motion and an even pressure, the electrode is then moved all over the pad while making a figure-8 motion as shown in figure 3.2. After 5-10 minutes the electrode was rinsed with copious amount of distilled water and was sonicated for 15 minutes with ethanol and distilled water to ensure complete removal of the alumina particles. It was then dried under Argon gas to be ready for use. This process was done before and after conducting CV , AMP and EIS measurements.

Figure 3.2: Electrode polishing process

3.2.3 Preparation of Solutions

Ethanol Solution

50 % of ethanol solution was prepared by mixing 25.5 ml of 98 % ethanol with 24.5 ml of distilled water. The obtained 50 ml solution was sonicated for 5 minutes before use.

Nafion Solution

1 % of Nafion solution was prepared by mixing 2 ml of 5% Nafion® 117 solution with 8 ml of distilled water. The 10 ml solution was sonicated for 5 minutes to carefully mix the solution.

0.5 M H_2SO_4 solution

0.5 M solution was prepared by mixing 27.74 ml of 98 % of H_2SO_4 with 972.26 ml of distilled water in a 1 L Standard Flask. This was used as an electrolyte for all electrochemistry measurements.

Phosphate buffer solution (PBS)

A buffer solution of 0.1 M and pH 7.4 was prepared by dissolving 8.895 g of disodium hydrogen orthophosphate (Na_2HPO_4) and 7.81 g of sodium dihydrogen orthophosphate ($Na_2H_2PO_4$) separately in 500 mL deionized water. Then the salt solution was mixed according to the Henderson-Hasselbach equation to obtain the required pH level. This was used for the application of the sensor.

3.2.4 Synthesis of Graphene Oxide (GO)

The synthesis of graphene oxide was conducted using the Modified Hummers method (Loryuenyong et al., 2013). 50 ml of concentrated H_2SO_4 was added to 2g of graphite powder into a 250 under stirring at room temperature. The flask was cooled to 0°C in an ice bath followed by a slow addition of 7 g $KMnO_4$. The flask was allowed to warm to room temperature. The flask was removed from the ice bath and the reaction temperature was raised to 35 °C. The reaction mixture was stirred with a Teflon coated magnetic stirrer for 2 h. After which it was cooled in an ice bath and 120 ml of H_2O was added as well as a slow addition of 20 ml H_2O_2 (30 % wt.) until gas evolution stopped. The reaction mixture was left to stir overnight. The resulting yellow brown suspension was extensively washed with ethanol and water and was centrifuged to remove residual exfoliated graphite. The material that was obtained was vacuum dried at 65°C overnight to give GO.

3.2.4.1Formation mechanism of GO

The active species to oxidize graphite is dimanganese heptoxide (Mn_2O_7) which is obtained via the reaction of monometallic tetra oxide ion MnO_3^+ and tetraoxomanganate (viii) ion (MnO_4^-) as shown by **equation (3.1)** below (Emiru & Ayele, 2017).

$$KMnO_4 + 3H_2SO_4 \rightarrow K^+ + MnO_3^+ + H_3O^+ + 3HSO_4^- \qquad \textbf{(3.1)}$$

$$MnO_3^+ + MnO_4^- \rightarrow Mn_2O_7 \qquad \textbf{(3.2)}$$

The transformation of MnO_4 into a more reactive form Mn_2O_7 will certainly help oxidize graphite powder as shown by **equation (3.3)** below.

$$Mn_2O_7 + H_2SO_4 + C\ (graphite) \rightarrow \begin{pmatrix} C - O - C \\ C - OH \\ COOH \end{pmatrix} + MnO_5 + \ H_2O + \ SO_4^{-2} \qquad \textbf{(3.3)}$$

3.2.4.2 Reduction of GO

In a typical reduction, 1 g of GO was dispersed finely in 200 ml distilled water and stirred by ultrasonic treatment for 3 h. After three hours, 2 g of $NaBH_4$ was added to the GO suspension while stirring. The solution was then heated in an oil bath at 80-100 °C under a water cooled condenser for 12 h. Water level was kept during the reduction. RGO was precipitated by centrifugation at 4500 revolutions per minute (rpm) for 15 minutes The supernatant was discarded and the precipitate of RGO was washed three times with acetone, ethanol and distilled water, respectively. The product was dried in a vacuum oven for 24 h. **Figure 3.3** shows the difference in the colour of the product obtain for GO and RGO when dispersed in water (Loryuenyong et al., 2013). The fabrication procedure is presented in **Scheme 3.1** showing the process of combinations of atoms and the electrochemical reactions taking place.

Figure 3.3: Colour comparison of 1.8 $mg.ml^{-1}$ of graphene oxide (brown) and reduced graphene oxide (black), respectively.

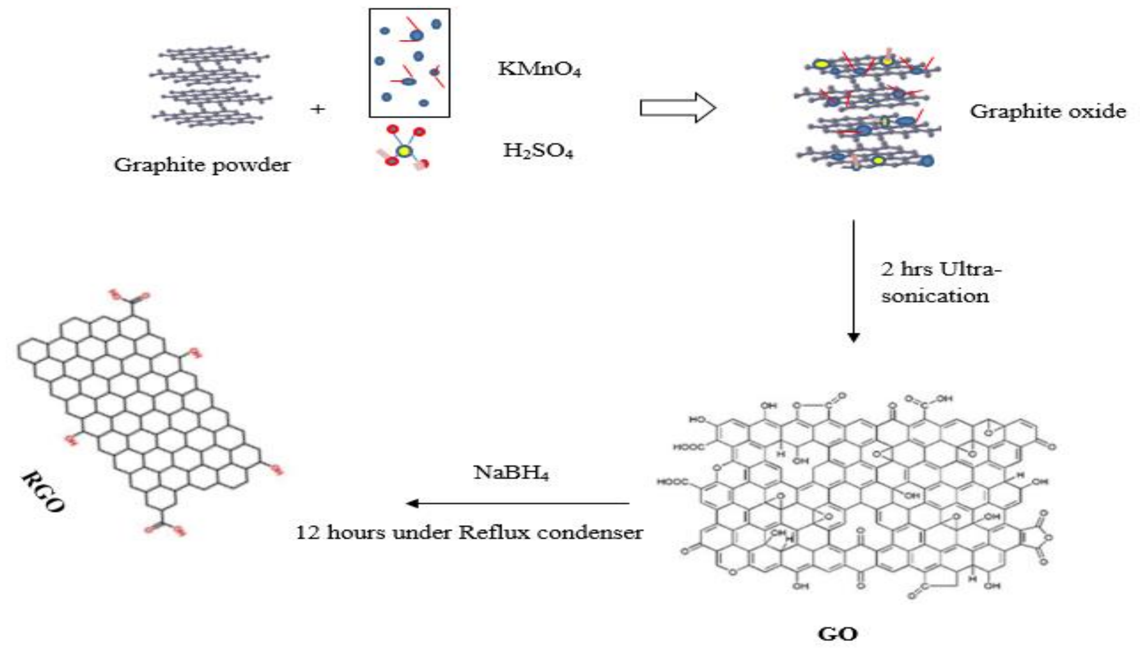

Scheme 3.1: Fabrication procedure of the representative GO using the Hummers method and reduction by sodium borohydride modified from (Rowley-Neale et al., 2018)

3.2.5 Synthesis of POM/RGO nanocomposite

Using a method developed by (Kim & Shanmugam, 2013), POM/RGO composite was prepared with a slight modification. 1 g of RGO was dispersed into 800 ml water containing 8 ml of ethylene glycol by ultra-sonication for 30 minutes. 10 g of POM was added to the solution and the system was subjected to an additional 10-minute stirring and ultra-sonication. The mixture was irradiated under (300 W) UV light for 2 h. The concentration of the reduced POM can be controlled by varying the irradiation time. Subsequently, the mixture was stirred in the dark at room temperature for 48 h, the colour changed from yellowish-brown to a blue-black colour. The blue-black solution was centrifuged and washed with ethanol and distilled water three times to remove the unabsorbed POM. It was then dried in an oven at 80 °C for 12 h. The **Scheme 3.2** below shows the intercalation process of the POM into the crevices of the RGO.

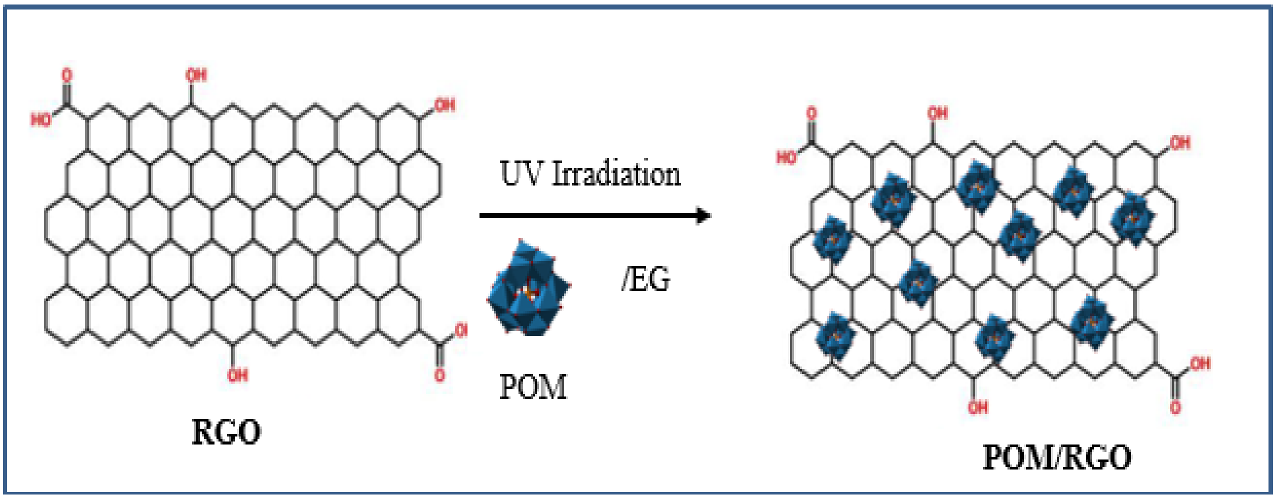

Scheme 3.2: Fabrication procedure of the representative POM/RGO nanocomposite (Kim & Shanmugam, 2013)

3.2.6 Synthesis of Ag-Fe_2O_3/POM/RGO nanocomposite

20 ml aqueous solution of 1.8 mg.ml^{-1} POM/RGO was mixed with 0.084 g of $AgNO_3$ (0.5 mmol) and 0.80 g of $Fe(NO_3)_3 \cdot 9H_2O$ (2 mmol) while stirring, for 15 minutes. To this 1.08 g of CH_4N_2O (0.018 M) and 2 g of PEG (0.5 mmol) were added and the above mixture was sonicated for 30 minutes at 25 °C. After sonication for 30 minutes, about 80 mL distilled water was added to the resulting solution and transferred into a 100 mL Teflon-lined stainless steel autoclave, and heated at 180 °C in an electric oven for 8 h. The resulting black product was cooled to room temperature, washed with deionized water and ethanol several times by centrifugation. Finally, the product was dried at 60 °C in a vacuum oven for 8 h and was labelled Ag-Fe_2O_3/POM/RGO nanocomposite. For comparison, bare Ag-Fe_2O_3 nanocomposite were prepared under similar conditions without addition of POM/RGO. Fe_2O_3 nanoparticles were also synthesized under similar conditions without adding $AgNO_3$ and POM/RGO. **Scheme 3.3** presents the fabrication procedure for the representative quaternary Ag-Fe_2O_3/POM/RGO nanocomposite.

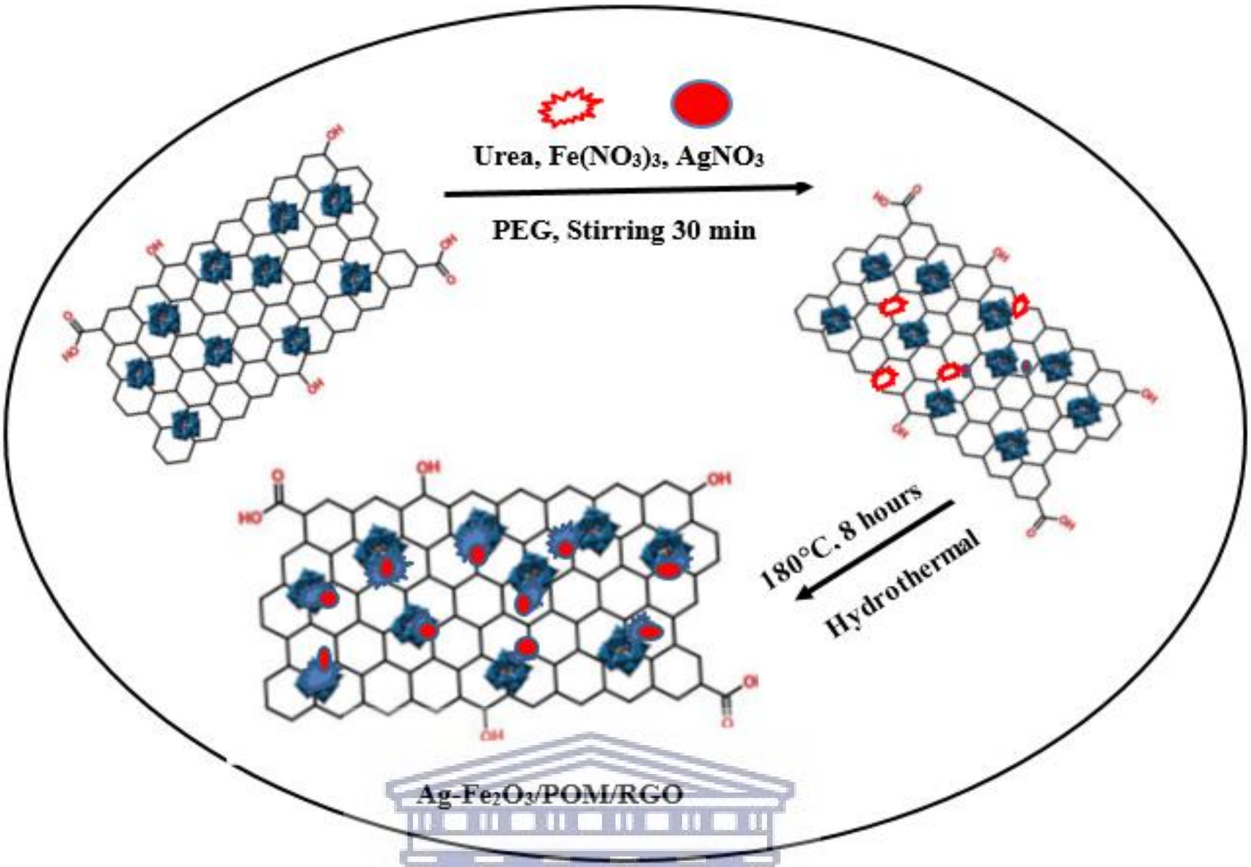

Scheme 3.3: Fabrication procedure of the representative quaternary Ag-Fe_2O_3/POM/RGO nanocomposite

To ease the reading, **Table 3.2** features all materials prepared in this study together with their methods of preparation. The total synthesised materials amounts to 7, consisting of four bare materials and 3 composites. In order to distinguish between the composites which were synthesised by "one pot" and "step by step procedure", who different types of styles were used. Symbol "-" was used for those that were prepared by "one pot" e.g. "Ag-Fe_2O_3 nanoparticles" and symbol "/" was used for those prepared by "step by step" procedure e.g. "POM/RGO". The symbol "//" was used to distinguish the deposition of the materials onto the working electrode e.g. "POM/RGO//GCE"

Table: 3.2: Summary of synthesized materials in this study

Abbreviation	**Modification**	**Preparation**
GO	Modified Hummers method	Modified Hummers method
RGO	Reduction by $NaBH_4$	Reflux condenser
POM/RGO	POM deposited on the surface of RGO	Uv light irradiation
Ag NP's	Ag NP's stabilized by PVA	Chemical method
Fe_2O_3 NP's	Fe_2O_3 NP's protected by PEG	Hydrothermal method
Ag-Fe_2O_3	Ag and Fe_2O_3 NP's	Hydrothermal method
Ag-Fe_2O_3/POM/RGO	Ag-Fe_2O_3 NP's are decorated on POM at the surface of RGO	One pot hydrothermal method

3.3 Instrumentation

The surface morphologies of the prepared materials were probed by High resolution Transmission Electron Microscopy (HRTEM Tecnai F20) and Scanning Electron Microscopy (Auriga HR). Energy Dispersive X-ray Spectroscopy (EDXS) was used to verify the weight percentages of the synthesised materials. Ultraviolet-Visible (UV-Vis) spectroscopy was used to analyse the chemical structure of the samples. A Fourier Transform Infrared Spectroscopy (FTIR) was used to get the vibrational spectra of the molecules in the samples. The structures were analysed by X-ray Diffraction (XRD). Electrochemical studies were recorded using PalmSensor. All the electrochemical tests were carried out 3 times and all the measurements were taken at room temperature.

3.3.1 Electrochemical studies

PalmSens was used to investigate and determine the electrochemistry of the modified electrode's electrochemical activity for the detection of H_2O_2. Included in the PalmSensor, the PalmSens software can run useful DC techniques such as Cyclic voltammetry (CV), chronoamperometry (CA) and chronopotentiometry (CP). For the detection of H_2O_2 CV was used and CP was used to determine the linear range, limit of detection, limit of quantification, selectivity and sensitivity of the H_2O_2 modified sensor.

3.3.1.1 Cyclic voltammetry (CV)

Cyclic voltammetry (CV) is one of the important and sensitive electroanalytical methods to study the redox processes, understanding reaction intermediates and obtaining stability of reaction products. Cyclic voltammetry provides crucial information regarding the thermodynamics and kinetics of redox processes based on varying the applied potential in both forward and reverse directions while monitoring the current. The peak potentials and peak currents of the cathodic and anodic peaks are two important parameters in a cyclic voltammogram (Wang, 2006). If the electron transfer process is fast when compared to other processes (such as diffusion), the reaction is said to be electrochemically reversible and the peak separation is:

$$\Delta E_p = E_{pa} - E_{pc} = \frac{2.303RT}{nF} \qquad \textbf{(3.4)}$$

In this work, the electrochemical performance of modified electrodes based on different composites was examined using cyclic voltammetry method in the presence and absence of 1 mM H_2O_2 in 0.5 M H_2SO_4 using PalmSens electrochemical workstation (Bioanalytical Systems, USA) monitored on PSTrace software at a potential window of -0,2 V to 0,8 V. This was done to understand the redox reactions of the synthesised composites in **Table 3.2** and to get information about the unique electrochemical behaviour of the composites and the electron kinetic differences between the individual components (RGO, POM) and the nanocomposites.

3.3.1.2 Amperometry (AMP)

In this technique, a constant potential is applied to a working electrode and the current is measured as a function of time. The constant potential is commonly selected (based on the CV experiments) such that the resulting current is mass transport limited, thus at steady state, it represents a concentration of the electro-active species, which is the analyte of interest or can be correlated to its concentration (Guy & Walker, 2016). Amperometry is based on study of the sensor response to a change of substrate concentration, which is referred as titration. It involves the current measurements of a sensor under constant polarisation immersed in a buffer solution, while changing the analyte concentration (stepwise) (Honeychurch, 2012). The results were plotted on a current versus time curve. The time between the changes of analyte concentration is determined by the properties of the sensor, namely by the time required for the current to reach equilibrium state. Solution was stirred to provide faster convective transport of the analyte to the electrode surface.

3.3.1.3 Electrochemical impedance spectroscopy (EIS)

The electrochemical impedance spectroscopy is a more general concept of resistance and has become very popular nowadays as a complementary technique for the characterization of electrode processes at complex interfaces. Electrochemical impedance spectroscopy is measured by applying AC potential with small amplitude (5 to 10 mV) to an electrochemical cell and measuring the current flowing through the working electrode. An electrode-solution interface undergoing an electrochemical reaction is treated as an electronic circuit consisting of a combination of resistors and capacitors (ref). By using this useful technique, the study of any intrinsic material property or specific processes that could influence the conductivity/resistivity of an electrochemical system is possible.

For electrochemical sensing, impedance techniques are useful to observe changes in electrical properties arising from biorecognition events at the surfaces of modified electrodes. In this work, this technique was used to analyse different modified electrodes with a frequency ranging from 0.1 to 1×105 Hz in 0.5 M H_2SO_4 solution.

3.3.2 Spectroscopic

3.3.2.1 A Fourier Transform Infrared Spectroscopy (FTIR)

Fourier Transform-Infrared Spectroscopy (FTIR) is an analytical technique that is used to measure the absorption of infrared radiation by the sample of interest versus wavelength to identify molecular components and structures. It modulates the wavelength from a broadband infrared source using an interferometer (Amir et al., 2013; Munajad, Subroto & Suwarno, 2018). The intensity of reflected or transmitted light is measured by a detector as a function of its wavelength. The signal obtained from the detector is an interferogram, which must be analysed with a computer using Fourier transforms to obtain a single-beam infrared spectrum. The FTIR spectra are usually presented as plots of intensity versus wavenumber (in cm^{-1}). Wavenumber is the reciprocal of the wavelength. The intensity can be plotted as the percentage of light transmittance or absorbance at each wavenumber.

In this work, the FTIR spectra of the samples were recorded at ~293 K on a PerkinElmer FT-IR spectrometer at a weight ratio in the 4000-300 cm^{-1} region. The samples were prepared using the KBr pellet method, typically 0.015 g of each synthesised material and 0.4 g of a pre-dried KBr were grounded in a mortar using a pestle to give a homogeneous mixture. The mixture was then pelletized by application of 7 tons of pressure. The resultant product was scanned on a Perkin Elmer Paragon 1000 PC FTIR spectrometer.

3.3.2.2 Ultraviolet-Visible spectroscopy (Uv-Vis)

UV-Visible spectroscopy (UV-Vis) is a spectroscopic technique that measures the extinction (scatter + absorption) of light passing through a sample. It refers to absorption spectroscopy in the ultraviolet-visible spectral region meaning, it uses light in the visible and adjacent (near-(UV) and near-infrared (NIR) ranges) (Weckhuysen, 2004). Because nanoparticles have unique optical properties that are sensitive to shape, size, concentration, agglomeration state and refractive index near the nanoparticle surface, UV-Vis becomes a reliable and valuable tool for the characterization, identification and studying the nanomaterials. In addition, UV-Vis is selective, sensitive, fast and simple for different types of nanoparticles and only needs a short period of time for the measurement with no calibration required for the particle characterisation of colloidal suspension (Zhang, Liu, et al., 2016).

In this work the UV-Vis spectra of the samples were recorded on Thermo Electron Corporation, Nicolet evolution 100 UV-Vis instrument. The colloidal suspension of each sample synthesised was at a concentration of 1mg/ml. Typically throughout the work, 10 mg of the material was dissolved in 50 % ethanol solution of 10 ml to make the suspension. Ethanol was chosen as a solvent because of its cut-off wavelength which as no significant interference on the wavelengths of the materials to be studied and that all the materials could be easy dissolved in ethanol.

3.3.2.3 X-ray Diffraction (XRD)

X-ray diffraction (XRD) is one of the most popular non-destructive analytical techniques for the analysis of both organic and inorganic crystalline materials. It is used to measure phase identification of a crystalline material, particle size, and to find structural imperfections in a sample from wide range of materials such as polymers, metals, proteins and minerals (Bykkam et al., 2015). In this work, a Brucker AXS (Germany) D8 advanced diffractometer unit, with a Cu-K radiation tube having wavelengths of K_1 1.54065 Å and a Lynx Eye position sensitive detector was used to record the data. The scanning was done in the 2θ range of 0.5° to 130° with step size of 0.034°. The XRD's working principle is based on Bragg's law. When X-rays of wavelength λ are incident at an angle θ on a crystal lattice, a section of these beams will be scattered in all directions. The necessary and sufficient condition for constructive interference is known as Bragg's law **equation (3.5)**. According to the law, scattered waves originating from each atom will be in phase with each another. **Scheme 3.4** shows the geometric requirements for this condition.

$$n\lambda = 2dsin\Theta \qquad \textbf{(3.5)}$$

Where,

λ = the X-ray's wavelength

d = the spacing of the crystal layers

Θ = the incident angle

n = an integer

The principle of Bragg's law is applied in the construction of instruments such as Bragg spectrometer, which is often used to study the structure of crystals and molecules. All aspects of this formula are introduced in **Schematic 3.4**, d_{hkl} is the interplanar spacing as a function of the Miller indices (h, k, and l) as well as the lattice parameters. Usually, diffraction experiments were applied at a fixed wavelength; therefore, measurement of the diffraction angles enables the calculation of the associated d_{hkl} and then the lattice constants (Das et al., 2010).

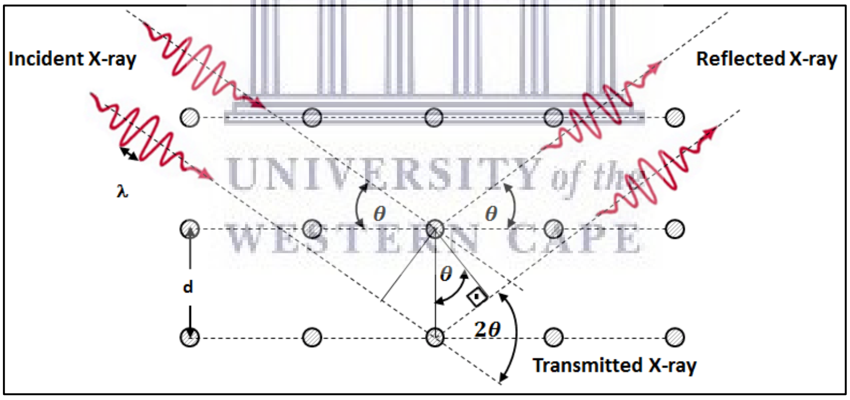

Scheme 3.4: Schematic of the diffraction of an X-rays beam by parallel atomic crystalline material (Bykkam et al., 2015)

3.3.2.4 Energy Dispersive X-ray Spectroscopy (EDXS)

Energy Dispersive X-Ray (EDX), sometimes called EDS or EDAX, is a qualitative and quantitative X-ray technique used to measure the elemental composition of solid surfaces. They are used in conjunction with Electron Microscopy instruments (Scanning Electron Microscopy or Transmission Electron Microscopy) instruments (Wenner et al., 2017). The EDX spectra of the samples were collected using EDAX liquid nitrogen cooled Lithium doped silicon detector instrument. The atomic number of the element within the sampling volume can be correlated to the intensity of backscattered electrons generated by the electron bombardment. Therefore, elemental information can be qualitatively determined. The emitted specific X-rays from the sample serve as finger prints giving elemental data of the samples, including quantitative and semi-quantitative information, as well as line profiling and spatial distribution of elements (MEHRVAR & ABDI, 2004).

3.3.2.5. Raman spectroscopy

Raman spectroscopy is a spectroscopic technique used to observe vibrational, rotational and other low-frequency modes in a system. Raman spectroscopy is commonly used to provide a fingerprint by which molecules can be identified. It relies on inelastic scattering or Raman scattering of monochromatic light, usually from a laser in the visible, near infrared, or near ultraviolet range. The laser light interacts with molecular vibrations, phonons or other excitations in the system, resulting in the energy of the laser photons being shifted up or down. The shift in energy gives information about the vibrational modes in the system (Gurvinder Singh Bumbrah, 2016). Typically, a sample is illuminated with a laser beam. Electromagnetic radiation from the illuminated spot is collected with a lens and sent through a monochromator. Elastic scattered radiation at the wavelength corresponding to the laser line (Rayleigh scattering) is filtered out, while the rest of the collected light is dispersed onto a detector by either a notch filter or a band pass filter (King et al., 2016). Spontaneous Raman scattering is typically very weak and as a result, the main difficulty of Raman spectroscopy is separating the weak inelastically scattered light from the intense Rayleigh scattered laser light.

The Raman spectra were obtained using Dilor XY Raman spectrometer with a Coherent Innova Argon laser employing different excitation wavelength for each synthesised material and are stated in **Chapter 4**. In this study Raman spectroscopy was used to study the vibrational information of the synthesized materials. A Raman Micro 200, Perkin Elmer precisely Spectrometer LabRAM HR800 (Spectrum software), with an output laser power of 50% was used to record the data. Raman analysis was conducted on powdered samples without any prior sample preparation. The spectra were recorded over a range of 50 to 3270 cm^{-1} using an operating spectral resolution of 2.0 cm^{-1}. The spectra were averaged with 20 scans, at an exposure time of 4 s.

3.3.3 Microscopic

3.3.3.1 High resolution Transmission Electron Microscopy (HRTEM)

High Resolution Transmission Electron Microscopy (HRTEM) is a technique in which a high intensity beam of electrons passes through a sample of interest and is able to determine its properties. Properties of most nanomaterials such as quantum dots nanotubes and nanowires are studied using HRTEM imaging. HRTEM analysis can also determine the elemental composition of the sample of interest. In this study, HRTEM was used to obtain the internal structure, crystallinity (lattice fringes) and the elemental composition of the synthesized nanomaterials. HRTEM analysis were performed by casting a drop of the synthesized material on a copper-nickel grid and dried under a lamp to evaporate the solvent for 15 min. Transmission electron micrographs (TEM) were collected using an FEI Tecnai G2 20 field mode at an accelerating voltage of 200kV from (Eindhovea, Netherlands)

3.3.3.2 High resolution Scanning Electron Microscopy (HRSEM)

High resolution Scanning Electron Microscopy (HRSEM) is an extremely useful tool for establishing the surface morphology and elemental composition of materials. Typically, an electron beam produced by an electron gun travels through a vacuum and scans over a selected area on the surface of the sample. As the electron beam scans the surface of the sample, a topographical and morphological representation of the surface is revealed. It then forms three types of images due to secondary electrons which are detected due to their low energies. Many researchers have used HRSEM to examine the morphology and microstructure of nanomaterials. In this study, HRSEM was employed to investigate the surface morphology and to obtain the elemental composition of the synthesised nanomaterials in **Table 3.2**. SEM images were obtained using AURIGA HIGH RESOLUTION Scanning electron microscope from Zeiss Oxford. The images were collected at 5 kV with a working distance of 6 mm. The sample was placed on a carbon supported by alumina and sputter coated for 30 min with a gold-palladium alloy to make the samples conductive.

3.3.3.3 Atomic Force Microscopy

Atomic Force Microscopy (AFM) is a technique that is used to map the surface (soft or hard, synthetic or natural) of a material on a nanoscale using a micro fabricated cantilever as a scanning probe. Three-dimensional topographies of the surface with spatial resolutions of angstrom or nanometre scales are revealed by the AFM image (Omidi et al., 2017). A sharp probing tip at the end of a spring-like cantilever is used to interact with the sample. When the probing tip automatically travels through the surface, the forces between the sample and the tip gives information about the topography of the sample (Kyeyune, 2017). In this study a Nanosurf easyScan 2 AFM system was used to analyse the structures and the morphology of the samples (materials).

3.3.3.4 Small Angle X-ray Scattering (SAXS)

SAXS is an accurate, non-destructive analytical method used to determine the structure of a particle system in terms of average particle sizes or shape. It usually requires only a minimum of sample preparation and the materials can be solid or liquid and can contain solid, liquid or gaseous domains (so called particles) of the same or another material in any combination. Usually, X-rays are sent through the sample (transmission mode) and every particle that happens to be inside the beam will send out signal. Thus, average structure of all illuminated particles in bulk material is measured. Application areas include biological materials, polymers, colloids, nanocomposites, metals, chemicals and can be found in research as well as quality control (Schnablegger & Singh, 2013).

In this study SAXS was used to determine the shape and the size of the Ag-Fe_2O_3 nanoparticles in the novel composite. The sample was prepared by dispersing Ag-Fe_2O_3/POM/RGO in ethanol solution. Small Angle X-rays Scattering was obtained from Anton Paar GmbH (Anton-Paar Str 20 A-8054 Graz).

CHAPTER 4

RESULTS AND DISCUSSION

Chapter overview

This chapter reports the characterization of the synthesized materials (GO, RGO, POM/RGO, Ag, Fe_2O_3, Ag-Fe_2O_3) and the novel Ag-Fe_2O_3/POM/RGO. These include spectroscopic and microscopic characterization techniques. It further discusses the electro-analysis of these materials by analytical techniques such as CV and EIS. Before reporting on the POM/RGO composite, characterizations of GO and RGO were reported to confirm the reduction process. As a result, this chapter kicks off with the comparison between GO and RGO. After, the results of POM/RGO are discussed to confirm the deposition of the POM onto the RGO sheets. This chapter then closes with the Ag-Fe_2O_3/POM/RGO results.

4.1 GO and RGO

4.1.1. Ultraviolet-visible spectroscopy

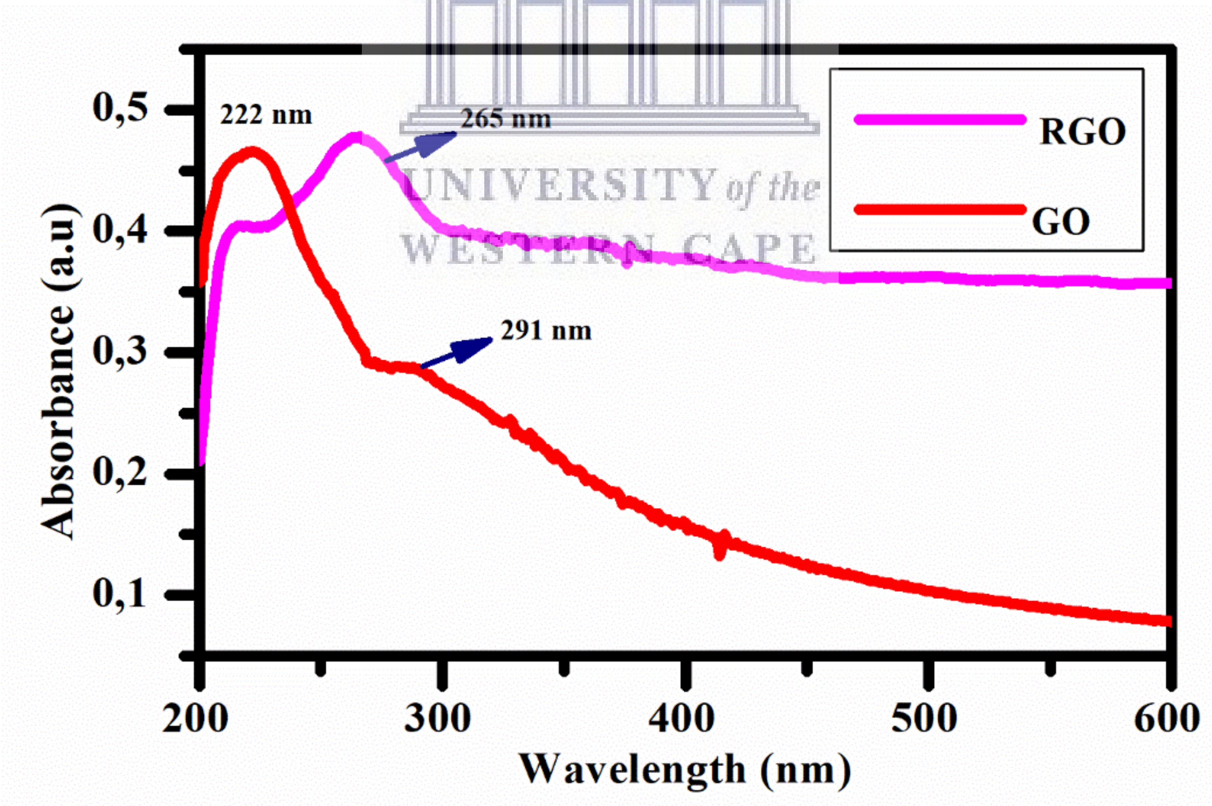

Figure 4.1: UV-vis spectra of GO and RGO

To check the efficiency of the reduction process, the UV-vis absorption spectra of aqueous suspensions of GO and RGO are presented in **Figure 4.1**. The absorption peak of GO shows two bands. The main maximum absorption band of GO observed at 222 nm can be attributed to $\pi \rightarrow \pi^*$ electron transitions of aromatic C-C bonds in the GO plane. The second shoulder band at 291 nm corresponds to $n \rightarrow \pi^*$ transition of C=O bonds (Smarzewska & Ciesielski, 2014) . After the reduction process to RGO, the maximum absorption band of GO at 222 nm have shown a bathochromic shit to 265 nm suggesting the reduction of GO and confirms restoration of the electronic conjugation within the graphene sheets. Moreover, the shoulder located at 291 nm in the structure of GO was not observed in the absorption of RGO this is due to the removal of oxygen-containing functional groups (Wei et al., 2012).

4.1.2. Fourier Transform Infrared Spectroscopy (FTIR)

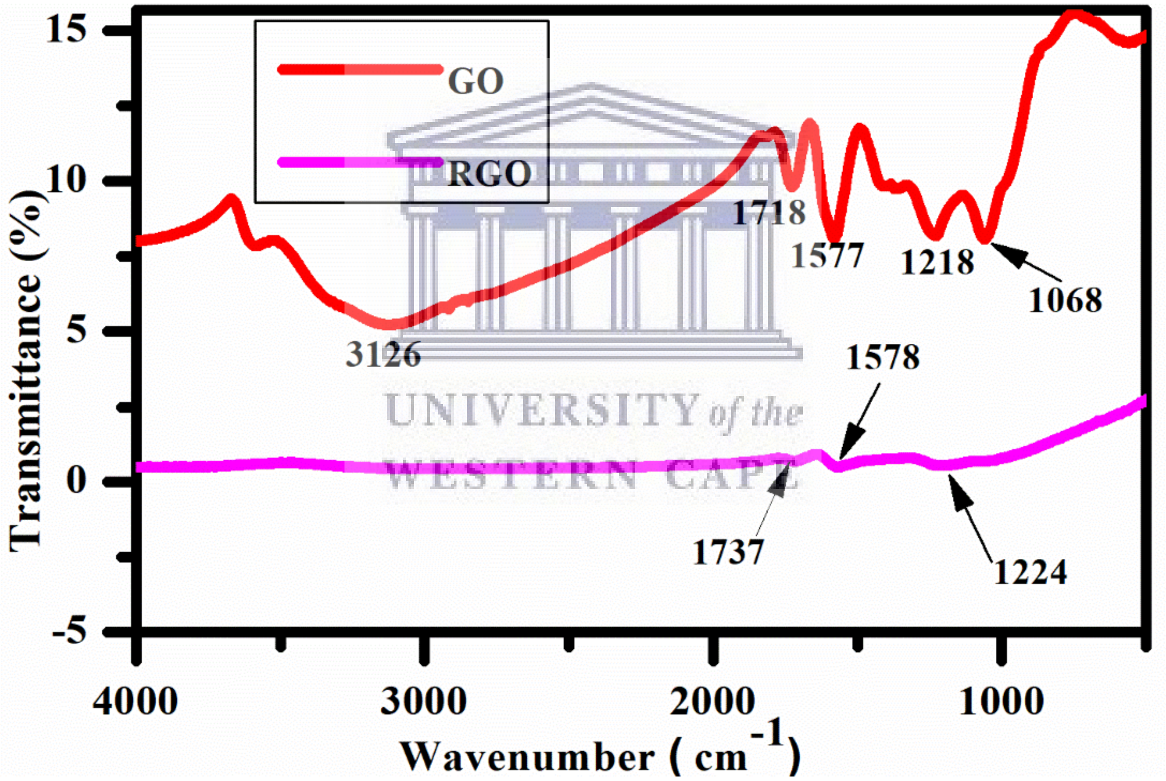

Figure 4.2: FTIR spectra of GO and RGO

The FTIR spectrum of the GO and RGO are shown in **Figure 4.2**. This is a suitable tool to determine the functional groups present before and after the reduction process. GO exhibits a broad peak at 3126 cm^{-1} which is assigned to O-H stretching vibrations mode. Other peaks centred at 1718 cm^{-1}, 1577 cm^{-1}, 1218 cm^{-1} and 1068 cm^{-1} are attributed to C=O stretching, sp^2 hybridized C=C group, C-O vibration of epoxy or alkoxy groups, and finally CO-O-CO anhydride group respectively (Lavin-Lopez et al., 2016). It is obvious from the RGO spectrum that the intensities of oxygen containing functional groups are almost invisible suggesting the effective reduction of GO. As observed in the spectra of RGO the peak at 3126 cm^{-1} assigned to O-H stretching disappeared , the peak at 1737 cm^{-1} is related to phenol C=C sp^{2} stretching and the bands at 1538 cm^{-1} and 1224 are related to C-O and C-OH respectively (Chettri et al., 2017). In other words, FTIR confirms the partial reduction of GO to RGO.

4.1.3. Raman spectroscopy

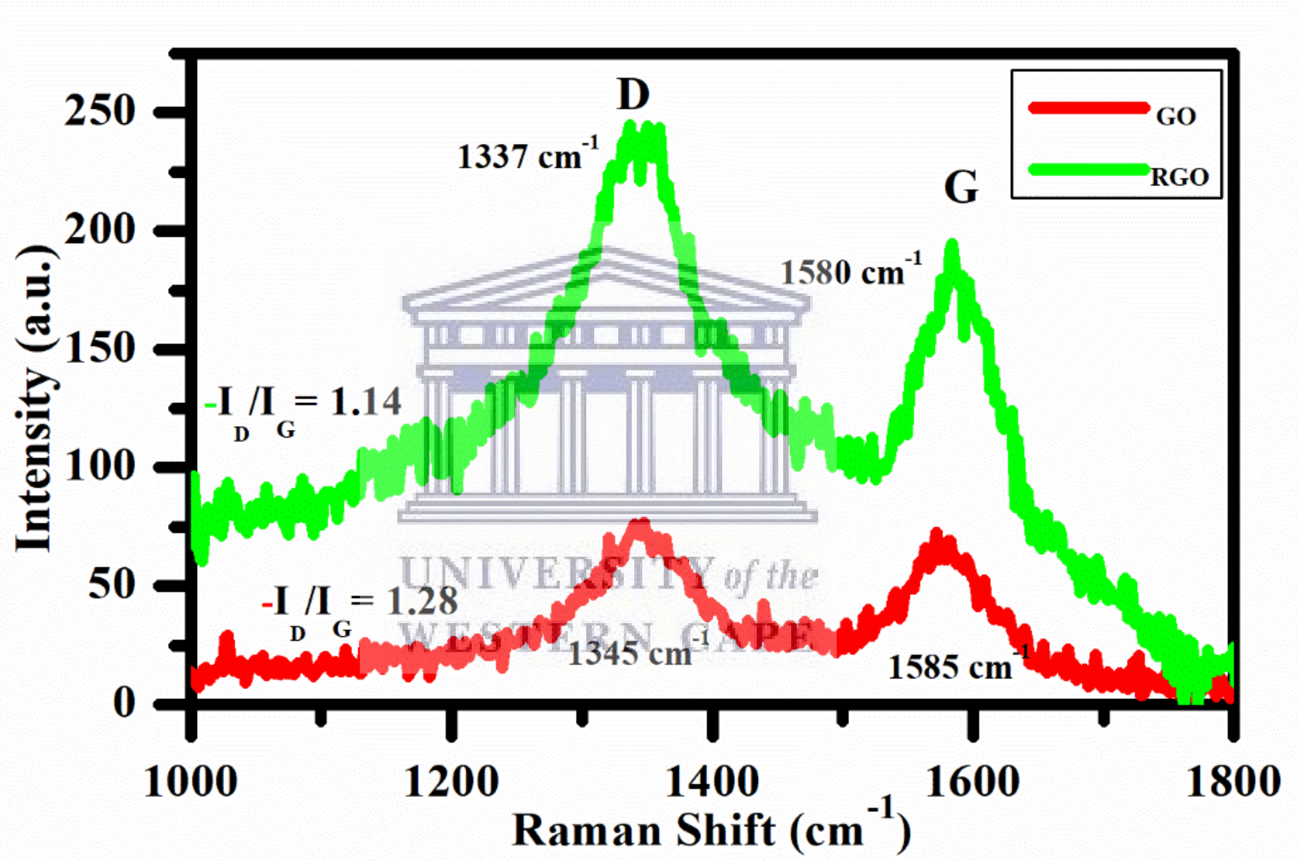

Figure 4.3: Raman spectra of GO and RGO obtained using excitation wavelength of 533 nm.

The reduction of GO to RGO was further investigated by Raman spectra. **Figure 4.3** shows the Raman spectra of GO and RGO. Usually two main bands exist in the spectra of graphite or graphene-based materials, i.e. the G band assigned to the first order scattering of the E_{2g} phonon from sp_2 carbon (graphite lattice), and the D band arising from the structural imperfections created by the hydroxyl (-OH) and the epoxide groups on the carbon basal plane (Bo et al., 2014; King et al., 2016). As shown in the spectra of GO, the D band is located at 1345 cm^{-1} and the G band is located at 1570 cm^{-1}. In comparison with GO, the spectra of RGO is similar to that of the former but showing higher intensity of the D band compared to the G band. A hypsochromic shift of 8 cm^{-1} to 1337 cm^{-1} can be observed for the D and also the G band shows a hypsochromic shift of 12 cm^{-1} to 1582 cm^{-1} in the RGO spectra due to the recovery of the sp_2 domain (Shang et al., 2012). The increase of I_D/I_G ratio from 1.14 (GO) to 1.28 (RGO) after reduction indicates the removal of most oxygen containing functional groups. Another possible reason is the increased fraction of graphene edges, which could also contribute to the increase in the I_D/I_G ratio (Liu et al., 2011a). These observations further confirm the formation of new graphic domains after the reduction process.

4.1.4. X-ray Diffraction (XRD)

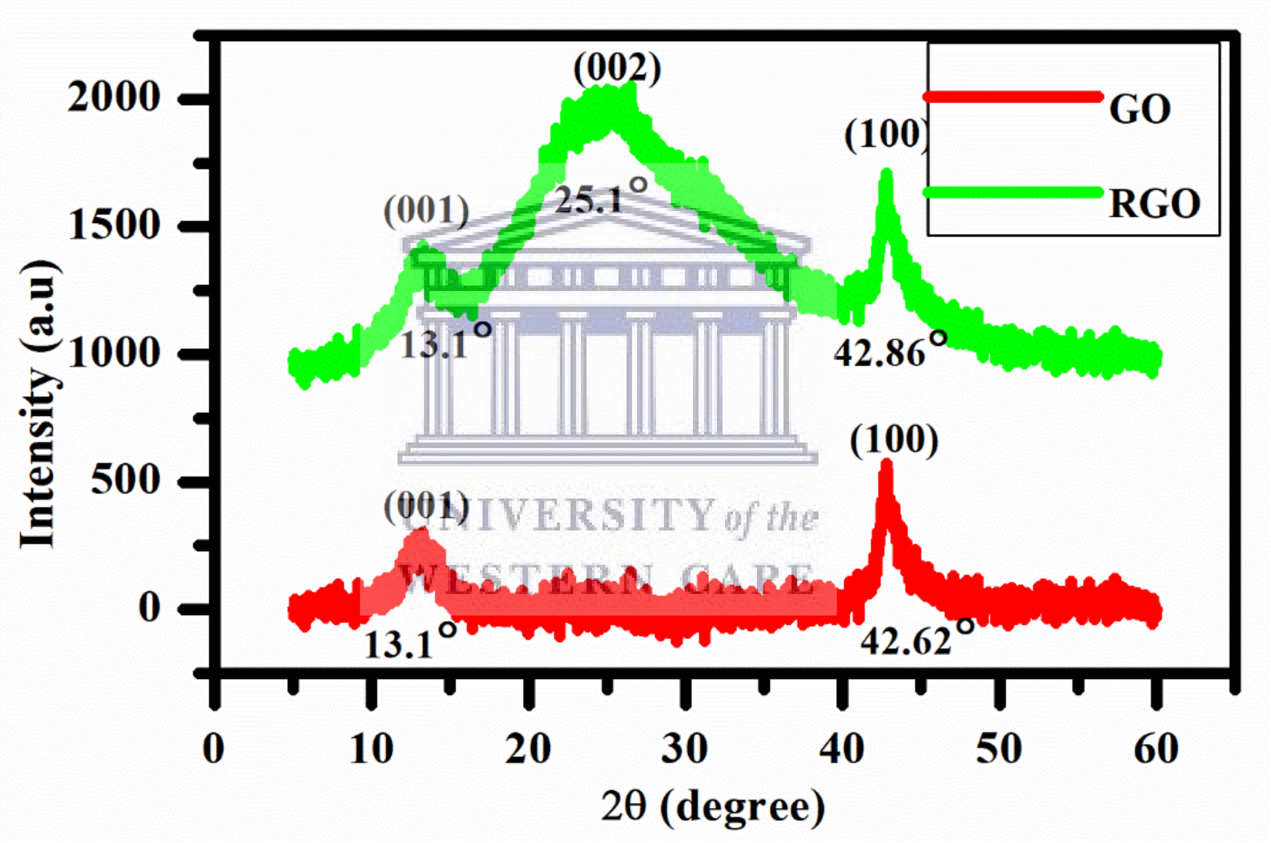

Figure 4.4: XRD spectrum of GO and RGO

The XRD pattern of GO and RGO are presented in **Figure 4.4.** GO exhibits a (001) diffraction peak at 2ϴ = 13.1° with a corresponding interlayer distance of 0.34 nm, this relatively large interlayer spacing of GO is due to the intercalation of water molecules and the formation of oxygen containing functional groups between the layers of graphite (Lavin-Lopez et al., 2016). After the reduction process, a new broad (002) diffraction peak is observed at 2ϴ = 25° corresponding to a layer by layer distance of 0.18 nm. This indicates that after the reduction process, the interlayer distance decreases due to the removal of oxygen containing functional groups, resulting in restacking of the RGO sheets (Emiru & Ayele, 2017). In addition, both the GO and RGO pattern show a (100) diffraction peak at 2ϴ = 42.62° and 2ϴ= 42.86° respectively indicating a short range order in stacked graphene sheets (Chettri et al., 2017). Moreover, a weak peak at 2ϴ = 13.1° is seen for RGO which suggests partial reduction of GO. These observations are in agreement with literature (Emiru & Ayele, 2017) and they confirm the reduction of GO.

After confirming the reduction process with the above characterizations the RGO was used to synthesize the POM/RGO composite as stated in ***Chapter 3.*** *The characterization of the POM/RGO is discussed below.*

4.2 POM/RGO composite

4.2.1 Ultraviolet-Visible spectroscopy (UV-Vis spec)

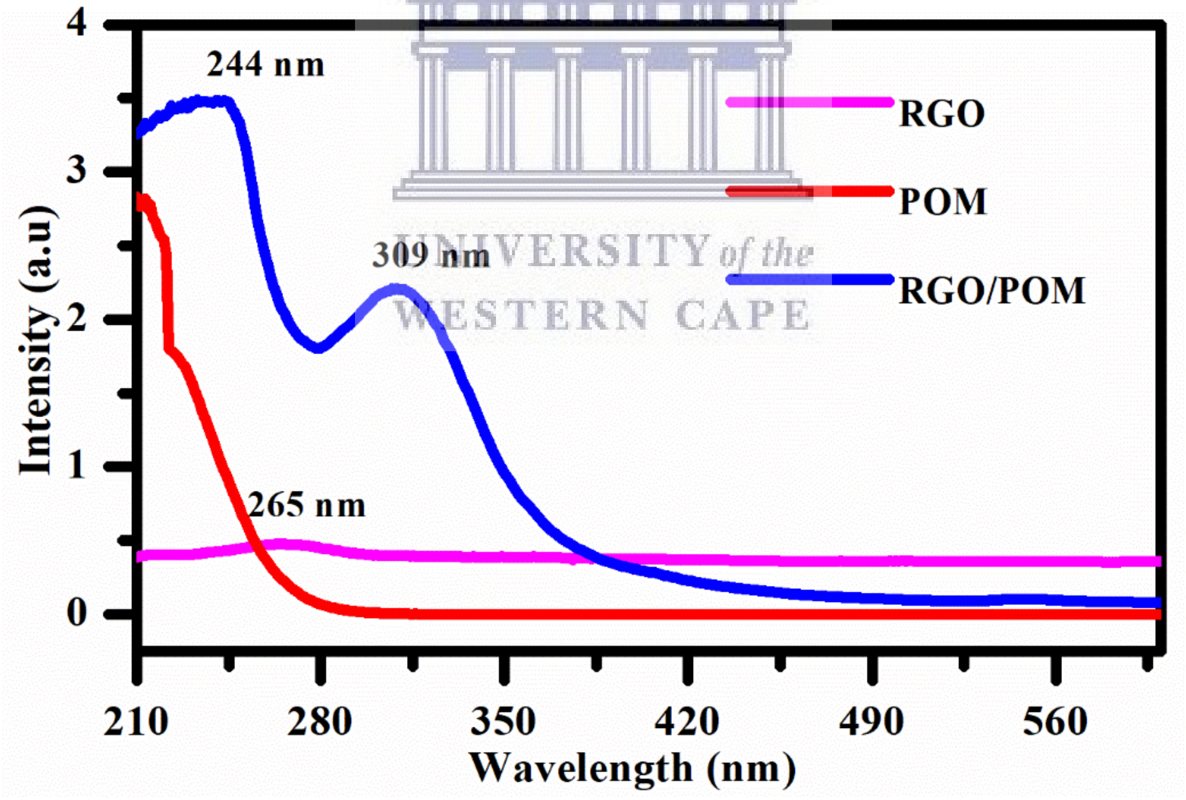

Figure 4.5: UV-vis absorbance spectra of RGO, POM, and POM/RGO

The formation of the POM/RGO hybrid material could be explained with the help of UV-visible spectra. Ethanol was chosen as a solvent because of its low 200 nm cut-off value and its stability for several number of days with both POM and RGO support. They have shown to form POM-shells, which contain up to 100s of individual POMs. For heteropolyoxomoybdates an absorption band usually observed between 200 and 400 nm with the main band centred at 310 form (Mo^{6+}) in octahedral coordination (Gupta, Aberg & Carrizosa, 2017). However, the absorption spectra of POM showed no significant band in the visible region. On the other hand, the absorption spectra of POM/RGO show a strong band at 309 nm which corresponds to O→M charge transfer transitions. Moreover, the second intense band at 244 nm assigned to the transition of d_{π}–p_{π} of electrons from $M{=}O_d$ bond showed a hypsochomic shift (form the spectra of RGO) due to the formation of the POM/RGO composite. These λ_{max} values of POM/RGO are the same with that of POM and RGO with slight shifting, which is in agreement with earlier reports (Mallick, Rana & Parida, 2012; Zhang et al., 2012),suggesting the presence of phosphomolybdic acid and RGO in the composite.

4.2.2 Fourier Transform Infrared Spectroscopy (FTIR)

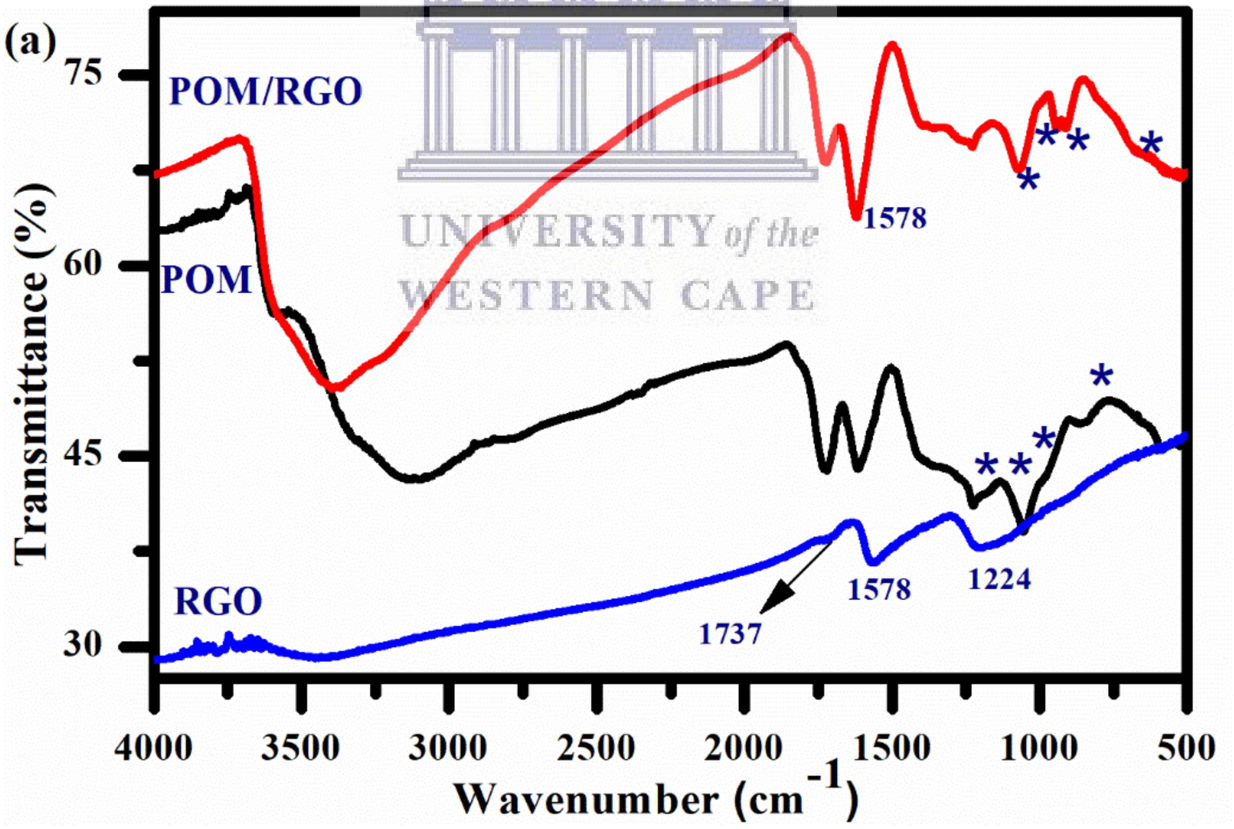

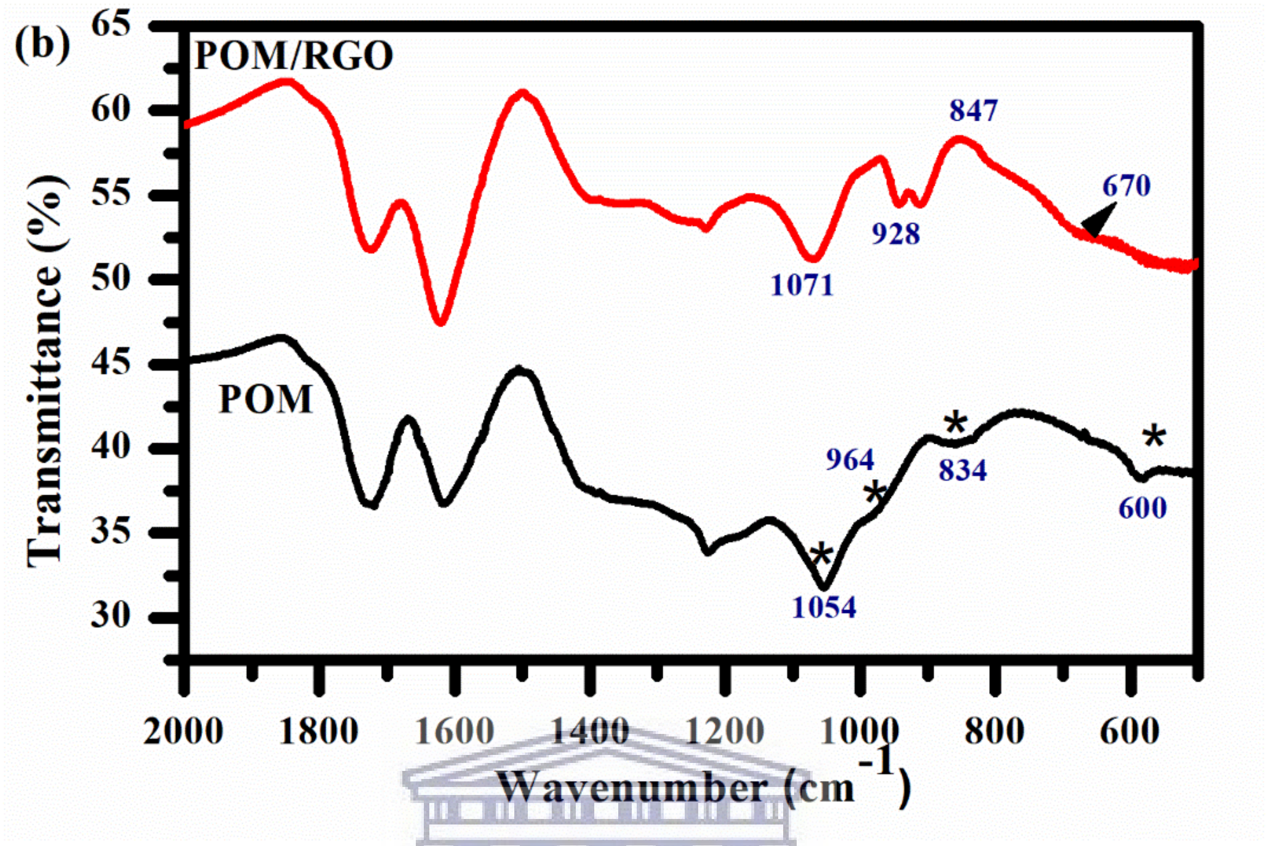

Figure 4.6: (a) FTIR spectra of POM, RGO and POM/RGO; (b) enlarged FTIR spectra of POM and POM/RGO over the range of 2000-500 cm^{-1}.

To further understand the interaction between POM and RGO, pure POM, RGO and POM/RGO were obtained, and the corresponding results are represented in **Figure 4.6** (a). Pure POM exhibited characteristic peaks at 1054 cm^{-1}, 964 cm^{-1}, 834 cm^{-1} and 600 cm^{-1} assigned to the stretching vibrations of the central-atom-oxygen (P-O) bond, the asymmetric stretching of the peripheral-atom-terminal oxygen (Mo-O) bond, vertex Mo-O-Mo bond and edge Mo-O-Mo bond respectively (Mallick, Rana & Parida, 2012). In the POM/RGO spectrum, the absorption at 1578 cm^{-1} is assigned to graphene skeletal vibration. The enlarged FTIR spectra of POM and POM/RGO over the range of 2000-500 cm^{-1} are presented in **Figure 4.6** (b). Compared with POM, the peaks attributed to POM/RGO are observed at 1071 cm^{-1}, 928 cm^{-1}, 847 cm^{-1} and 670 cm^{-1}. The shifting of these peaks is due to the presence of strong interaction between RGO and POM (Yuan et al., 2015a).

.

4.2.3 X-ray Diffraction (XRD)

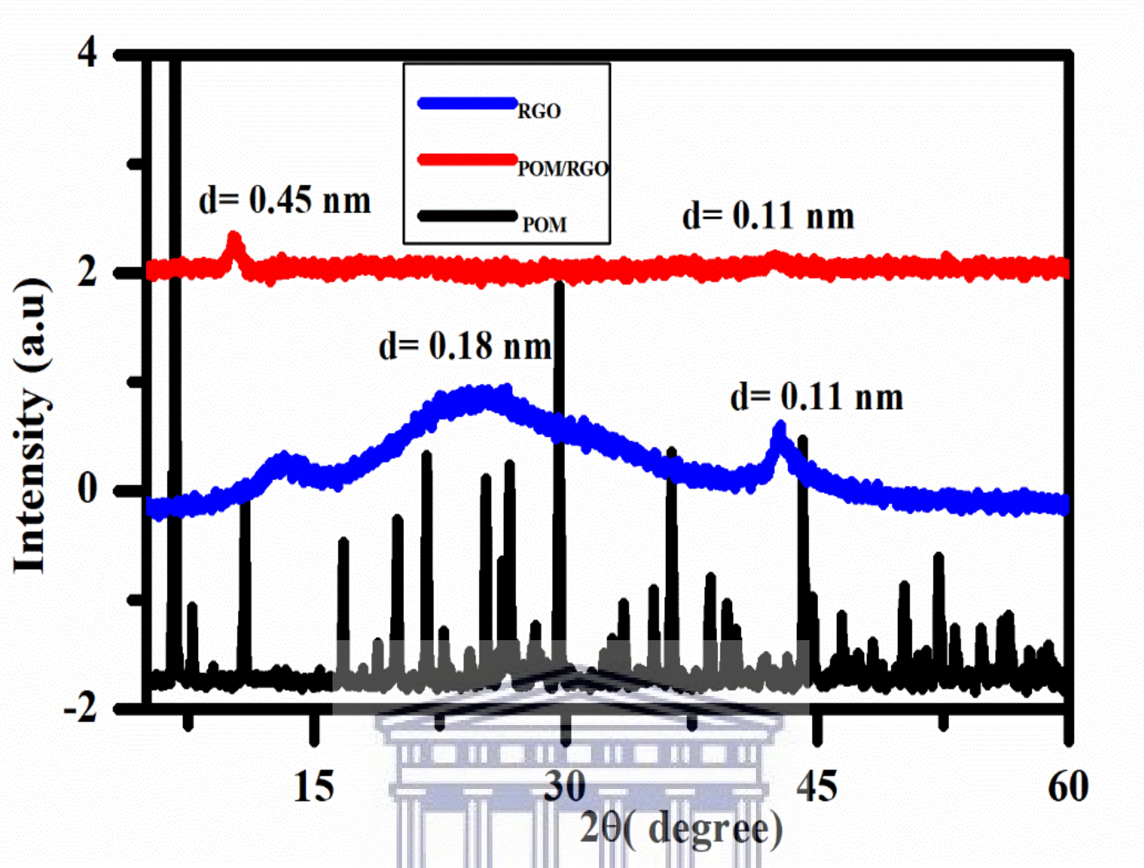

Figure 4.7: XRD spectrum of RGO, POM and POM/RGO

The XRD results of the prepared materials are shown in **Figure 4.7**. To demonstrate the formation of POM/RGO composite the XRD patterns of POM and RGO nanocomposites were also included. XRD characteristic peaks of phosphomolybdic from its hydrate form ($H_3Mo_{12}O_{40}P{\cdot}xH_2O$) can be observed above, these patterns are similar to characteristic peaks of the monoclinic Keggin structure (Li, Zhang, et al., 2010; Paul et al., 2015). However, no distinct diffraction peaks of POM observed in the XRD spectra of POM/RGO, which further suggest that POM clusters are highly dispersed on the surface of the RGO in the composite (Yuan et al., 2015b). The mentioned spectrum reveals that POM has been successfully immobilized on the surface via UV-irradiation.

4.2.4 Raman Spectroscopy

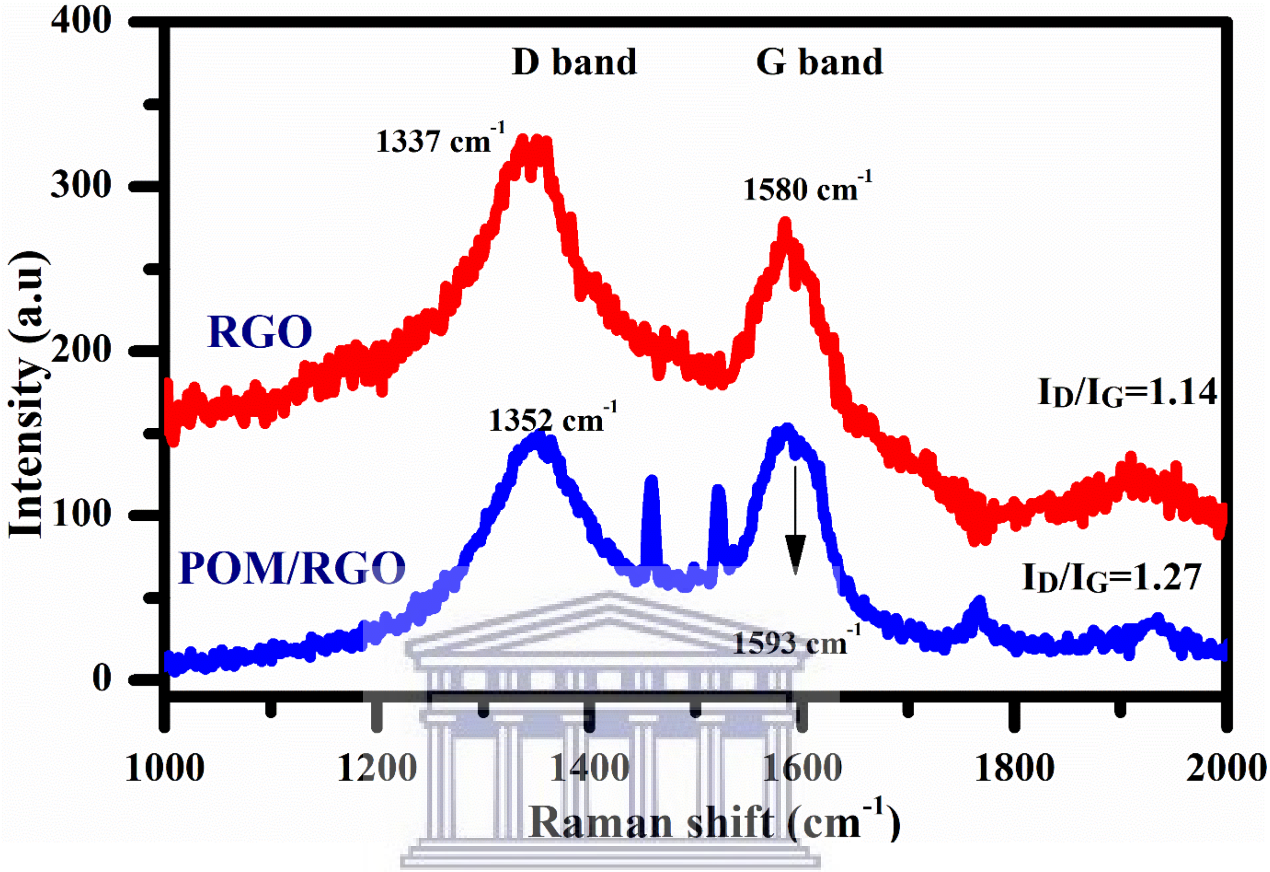

Figure 4.8: Raman spectra of RGO and POM/RGO obtained using excitation wavelength of 533 nm.

From the Raman spectra of POM/RGO and RGO in **Figure 4.8**, the D and G bands of POM/RGO showed some red shifts from 1337 cm^{-1} to 1352 cm^{-1} and 1580 cm^{-1} to 1593 cm^{-1}, respectively. This result is attributed to the strong interaction between RGO and POM in the nanocomposite (Chen, Liu, et al., 2013). Furthermore, there is an increment in the I_D/I_G value from RGO to POM/RGO (1.27). This indicated that introduction POM onto the graphene sheet results in increased disorder, defects and sp_2 domain sites on the sheets owning to the electron movement from the POM to the RGO sheets. These observations are similar to previous reports (Kim & Shanmugam, 2013).

4.2.5 Atomic Force Microscopy (AFM)

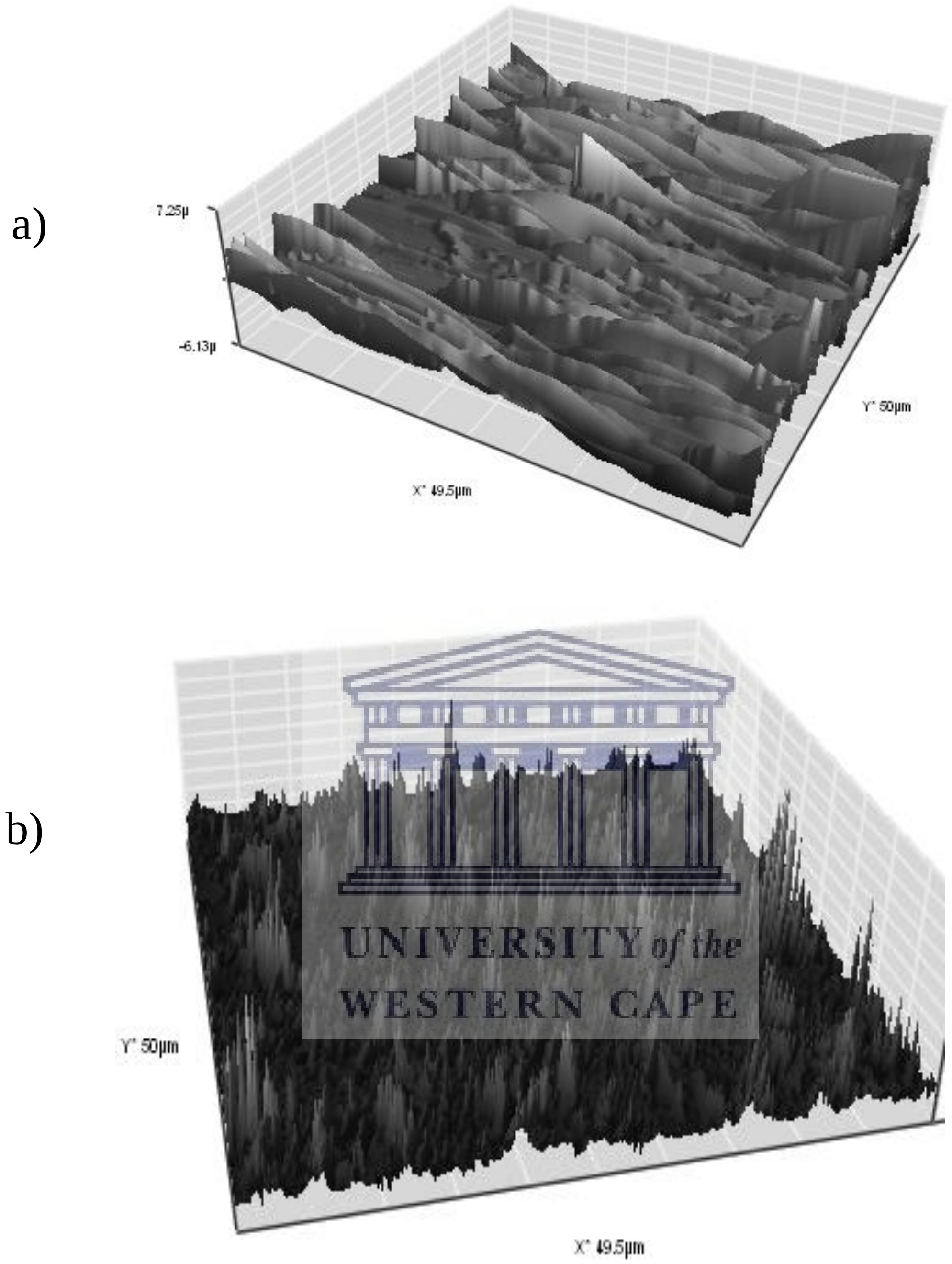

Figure 4.9: AFM images of RGO (a) and POM/RGO (b).

The surface morphologies of the RGO and POM/RGO were characterized using AFM. **Figure 4.9** (a and b) gives a typical AFM tapping mode of the surface of GCE drop coated with POM/RGO and RGO. The RGO sheets form a casually organised sheets which are parallel to the surface. Comparing **Figure 4.9** (a) and (b), the POM/RGO, have a roughness than RGO. The POM individual clusters are fully dispersed onto the RGO sheet resulting in their arrangement on the RGO sheets. We also noticed that the RGO is not observed in **Figure 4.9** (b), this is because the POMs are highly dispersed onto the sheets making it difficult to see the RGO.

4.2.6. Transmission Electron Microscopy (TEM)

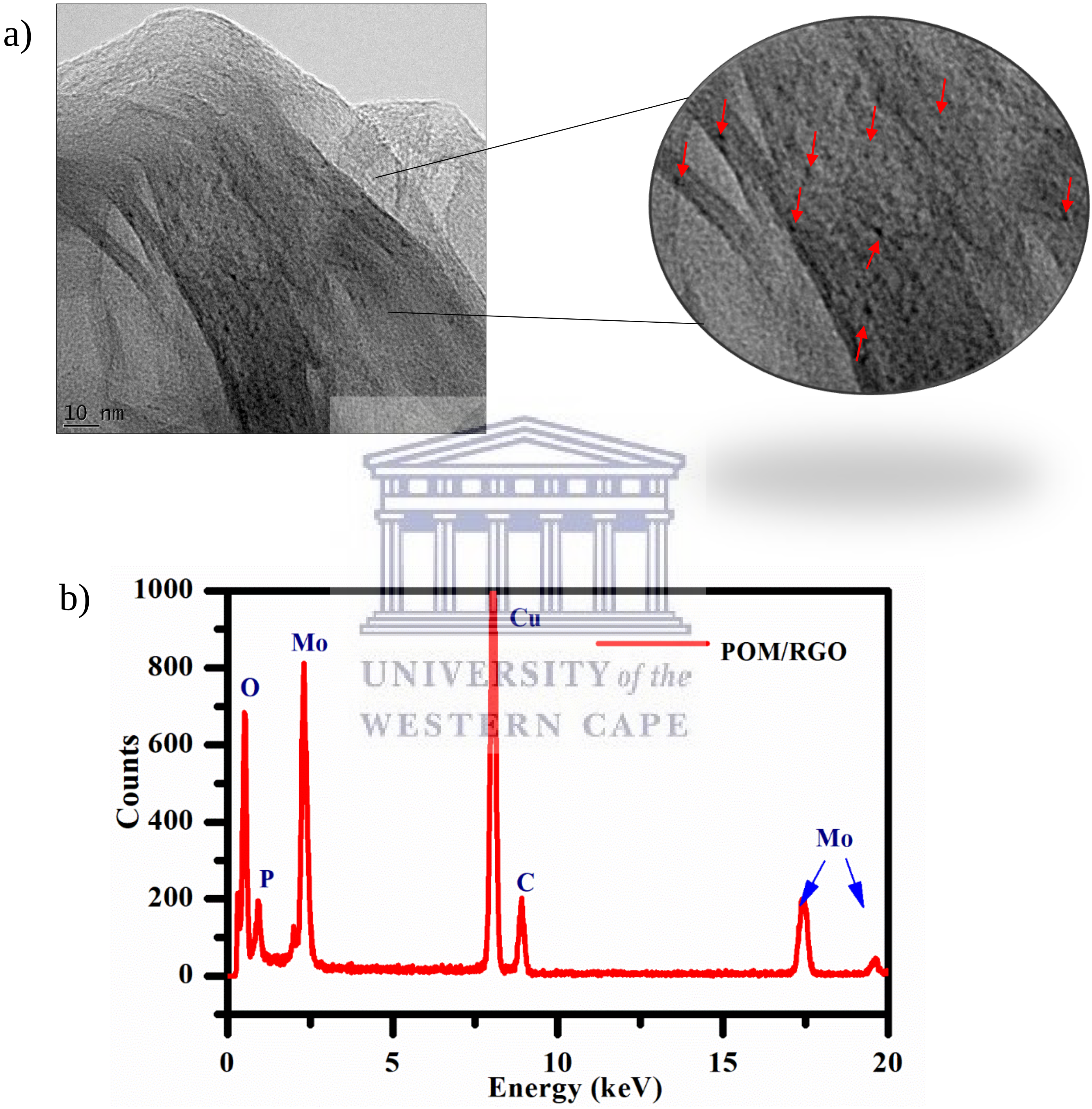

Figure 4.10: (a)TEM image of POM/RGO and EDX analysis of POM/RGO (b).

In order to support the observation from AFM, TEM was used to investigate the surface morphology of the synthesized nanocomposite. The morphology of POM/RGO in **Figure 4.10**

(a) reveals that the nature of RGO is highly beneficial to provide high surface area on the glassy carbon electrode (GCE). The dispersed POM clusters (zoomed image) indicate that POM strongly interacted with the RGO. Particularly, particles at some regions or edges were observed. This might result in aggregation of POM though strong interaction with some oxygen containing functional groups on the RGO. Schweger and his colleagues reported that POM clusters interact with oxygen containing functional groups of activated carbons (Kim & Shanmugam, 2013). The dark spots marked with red arrows are POM individual clusters dispersed on the RGO sheet. These results are in agreement with the AFM results. EDX analysis of POM/RGO confirms the formation of the nanomaterial. The C, from RGO and the P, Mo and O from the POM are observed in the EDX.

4.2.7 Scanning Electron Microscopy (SEM)

Figure 4.11: SEM images of RGO (a) and POM/RGO (b) at a scale view of 200.

The morphology of POM/RGO nanocomposite was investigated by SEM as shown in **Figure 4.11**. For comparison, a SEM image of RGO was included. As shown in Figure 2 (a) the surface of RGO nanosheets was smooth, with the sheets of RGO being visible. In the **Figure 4.11** (b) the POM nanoparticles were randomly deposited on the surface of RGO, which indicates that there was a strong interaction between POM and RGO. This confirms the AFM results.

4.2.8 Cyclic voltammetry (CV)

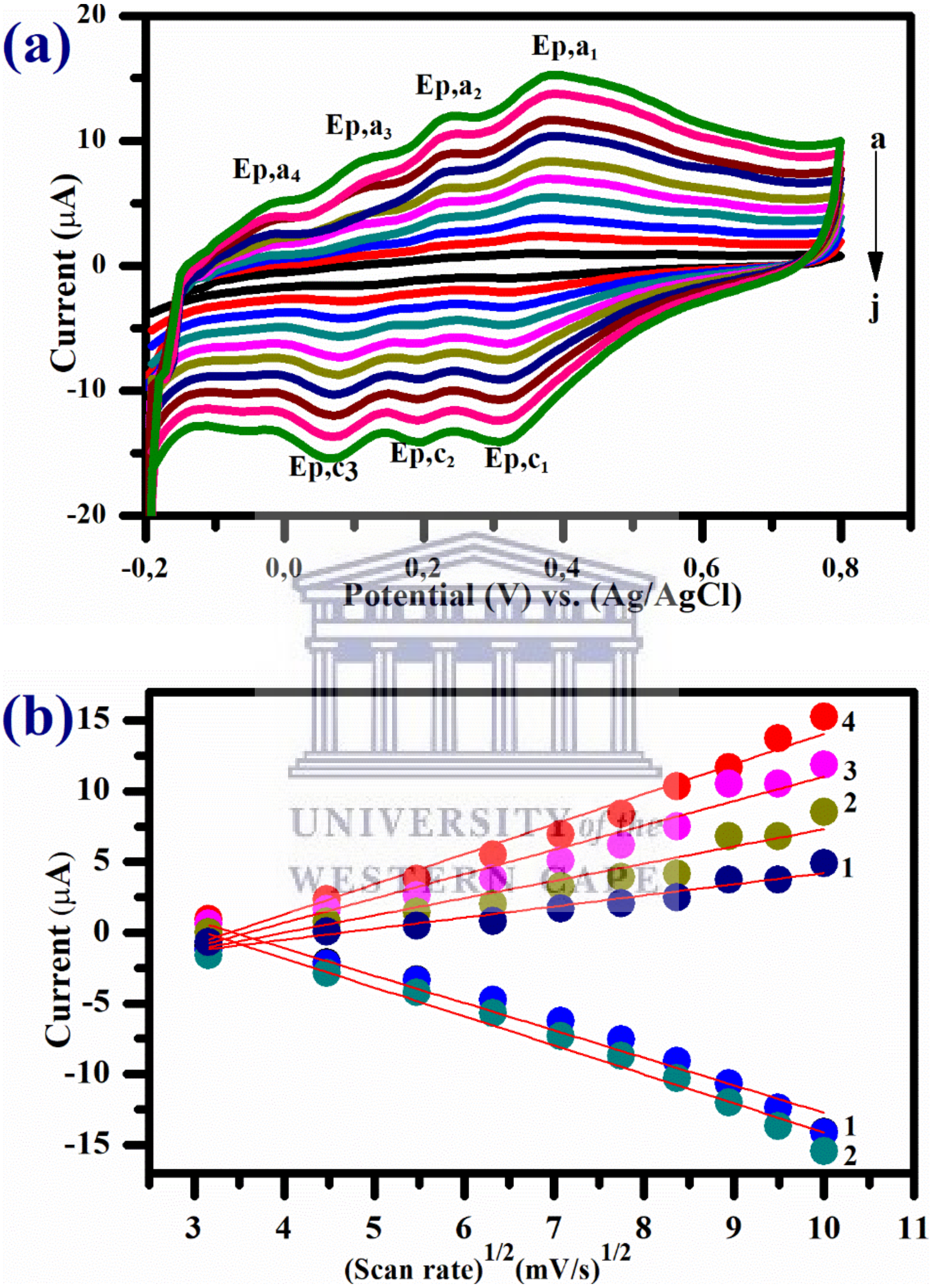

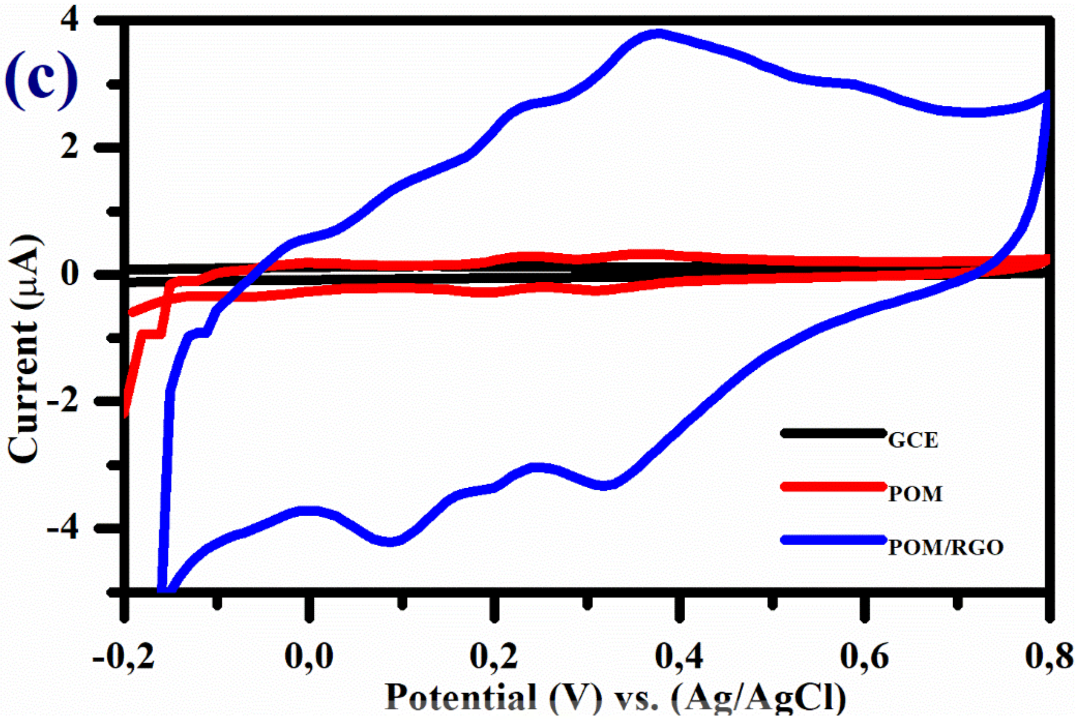

Figure 4.12: (a) CV of POM/RGO/GCE (a) in 0.5 M H_2SO_4 solution with different scan rate from a to j (10, 20,30,40,50,60,70, 80, 90, 100 mVs^{-1}). CV curves (b) shows the redox peak current versus the square root of scan rate of POM/RGO. (c) The comparison CV between POM, GCE and POM/RGO at a scan rate of 30 mVs^{-1}.

Table 4.1: The electrochemical parameters of POM/RGO/GCE IN 0.5 M H_2SO_4

POM/RGO peaks	Epa	Epc	Ep$_{1/2}$	ΔE
1	0.37	0.32	0.34	0.05
2	0.23	0.19	0.21	0.04
3	0.11	0.08	0.09	0.03
4	-0.02	0	-0.011	-0.02
Where Epa and Epc are anodic and cathodic peak potentials, respectively. The mean peak potentials are $E_{1/2}$ = (E pa+ Epc)/2				

To conduct CV measurements 1 mg of POM/RGO was dispersed in 1 ml ethanol solution to generate a homogeneous black mixture. Subsequently, 3 µl of the suspension was dropped onto a GCE and dried at room temperature to form POM/RGO/GCE. **Figure 4.12 (**a) shows the CV of POM/RGO modified GCE in the 0.5 M H_2SO_4 solution. In (a), the POM/RGO/GCE at different scan rates showed three reversible redox peaks and one weak irreversible peak at $E_{1/2}$ 0.35 V, 0.21 V, and -0,1 V as shown in **Table 4.1** and the peak separation potential of these peaks are no more than 60 mV. These results were in agreement with those reported by (Manivel & Anandan, 2011; Chen, Liu, et al., 2013). Redox peaks one, two and three corresponds to the reduction and oxidation via two-, four-, and six-electron process, respectively, which is demonstrated by the following equations **(2.4 -2.6)** (Wang, Han, et al., 2014):

$$PMo_{12}O_{40}^{3-} + 2e^{-} + 2H^{+} \rightarrow H_2PMo_{12}O_{40}^{3-}$$
$$H_2PMo_{12}O_{40}^{3-} + 2e^{-} + 2H^{+} \rightarrow H_4PMo_{12}O_{40}^{3-}$$
$$H_4PMo_{12}O_{40}^{3-} + 2e^{-} + 2H^{+} \rightarrow H_6PMo_{12}O_{40}^{3-}$$

The peak currents are proportional to scan rate as shown in **Figure 4.12 (**b), a linear relationship can be observed between anodic/cathodic peak currents vs (scan rate)$^{1/2}$ which can be supported by $R^2 = 0.9598$ for cathodic and $R^2 = 0.9676$ for anodic (using redox couple 2), this indicated that the reaction of POM on the surface of RGO was controlled by surface redox process. For comparison, the CV of bare GCE and POM modified GCE are also given in **Figure 4.12** (c). There are no redox peaks observed on the bare electrode in the potential range from +0.8 to -0.2 V. For the POM modified GCE, three reversible couples are observed. The POM/RGO modified GCE was similar to that of POM modified GCE, although the intensities of the peaks were obviously strengthened, indicating that the introduction of RGO did not only play a role in increasing the electroactive surface area but also facilitated electron-transfer due to its high electric conductivity. Electrochemical behaviour of POM/RGO showed a fast, surface controlled electron transfer process.

4.2.9 Electrochemical impedance spectroscopy (EIS)

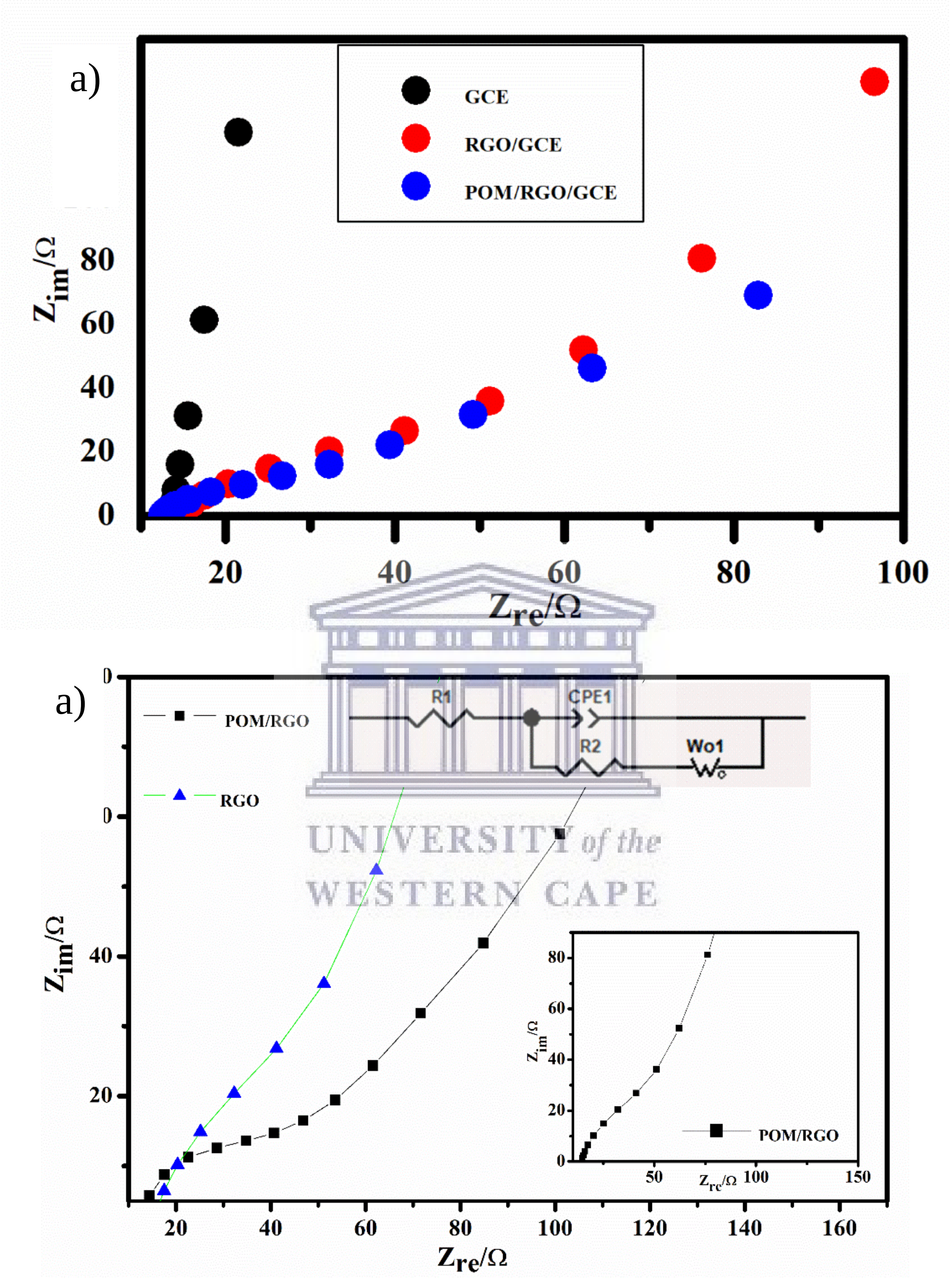

Figure 4.13: (a) Nyquist plot of bare glassy carbon electrode, RGO and POM/RGO. To clearly see the difference, POM/RGO and RGO EIS are presented in (b). Insert plot POM/RGO and the fitted circuit.

EIS is an effective method for probing the features of surface modified electrodes. It is capable of giving useful information about defects/holes exist on the modified surfaces, the kinetics and mechanism of the film formation processes and surface coverage. **Figure 4.13** (a) represents the impedance plot (Nyquist diagram) of the bare GCE, RGO/GCE and the POM-RGO/GCE in 0.5 M H_2SO_4 solution and **Figure 4.13** (b) shows the Nyquist diagram of RGO and POM. In addition, the inset plot on **Figure 4.13** (b) shows the experimental data that are fitted to standard Randles equivalent circuits for POM/RGO surface analysis which comprises the solution resistance (Rs), the charge transfer resistance (Rct), the constant phase element (CPE) and in addition W for the Warburg element which is in a series connection to Rct in the case of POM-RGO/GCE. The EIS graph (curve of GCE) demonstrated that the value of charge transfer resistance (R_{ct}) of bare GCE was calculated to be 75 ohm. When the bare GCE was modified with RGO, the value of R_{ct} was lower (11 ohm) (curve RGO). Because of the lower value, we can say that the RGO increases the rate of electron transfer. When POM was modified with RGO, the value of R_{ct} of POM-RGO/GCE was lower than that of RGO/GCE (curve of POM/RGO/GCE) (5 ohm). Thus, the addition of POM shows the increase of catalytic activity. These performances were attributed to the large surface area and the synergistic effect of POM and RGO.

‘The prepared composite was used as a surface for depositing the Ag-Fe_2O_3 *nanopaticles”*

4.3 Novel Ag-Fe_2O_3/POM/RGO

4.3.1 Ultraviolet-Visible spectroscopy (Uv-Vis spec)

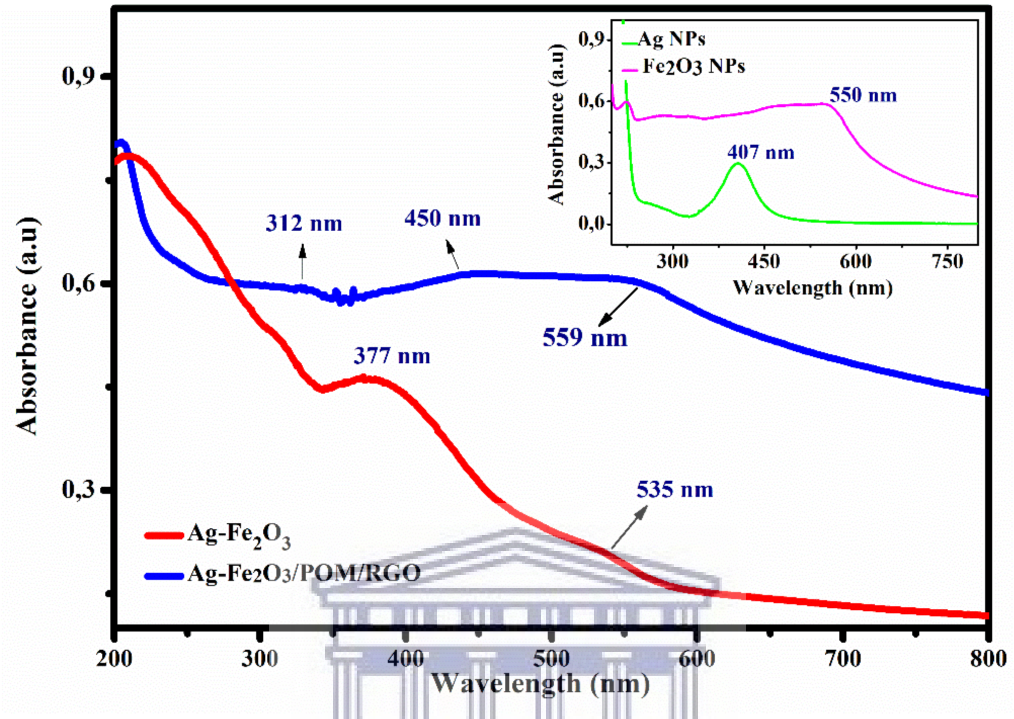

Figure 4.14: UV-vis spectra of Ag-Fe_2O_3/POM/RGO and Ag-Fe_2O_3/POM/RGO. Insert plot of Ag and Fe_2O_3 nanoparticles UV-vis spectra.

The formation of Ag-Fe_2O_3 nanoparticles and the novel Ag-Fe_2O_3/POM/RGO nanocomposite during the hydrothermal method were monitored by UV-Vis spectra in **Figure 4.14**. Pure Ag and Fe_2O_3 nanoparticles were also synthesised for comparison and an insert plot is presented to clearly see their individual absorbance's. From the inset plot, pure Ag nanoparticles and Fe_2O_3 nanoparticles show absorbance peaks at about 407 nm (Liu et al., 2011b) and 550 nm (Jang et al., 2009), respectively. In the Uv-Vis spectra of Ag-Fe_2O_3 nanoparticles the 377 nm peak assigned to Ag showed a bathochromic shift to 450 nm shoulder in the Ag-Fe_2O_3/POM/RGO spectrum. It was research that this peak position and shape are attributed to the surface plasmo resonance of the Ag nanoparticles (Van der Horst et al., 2015). The red shift of this peak can be due to the change in the dielectric environment and electron density of the Ag induced by the RGO sheets (Gao, Chen & Jiang, 2013; Geetha Bai et al., 2016). On the other hand, the shoulder assigned to Fe_2O_3 at 535 also show a bathochromic shift to 589 nm. This weak band for Fe_2O_3 corresponds to the ligand field transition of Fe^{3+} or the d-d transition (Narasimharao, Al-Shehri & Al-Thabaiti, 2015). A weak shoulder band at 312 nm was also observed possibly from the deposition of the Ag-Fe_2O_3 nanoparticles in the surface of POM/RGO due to agglomeration of the nanoparticles (Zhang, Bi, et al., 2016). This agglomeration is in accordance with the TEM results.

4.3.2 Fourier Transform Infrared Spectroscopy (FTIR)

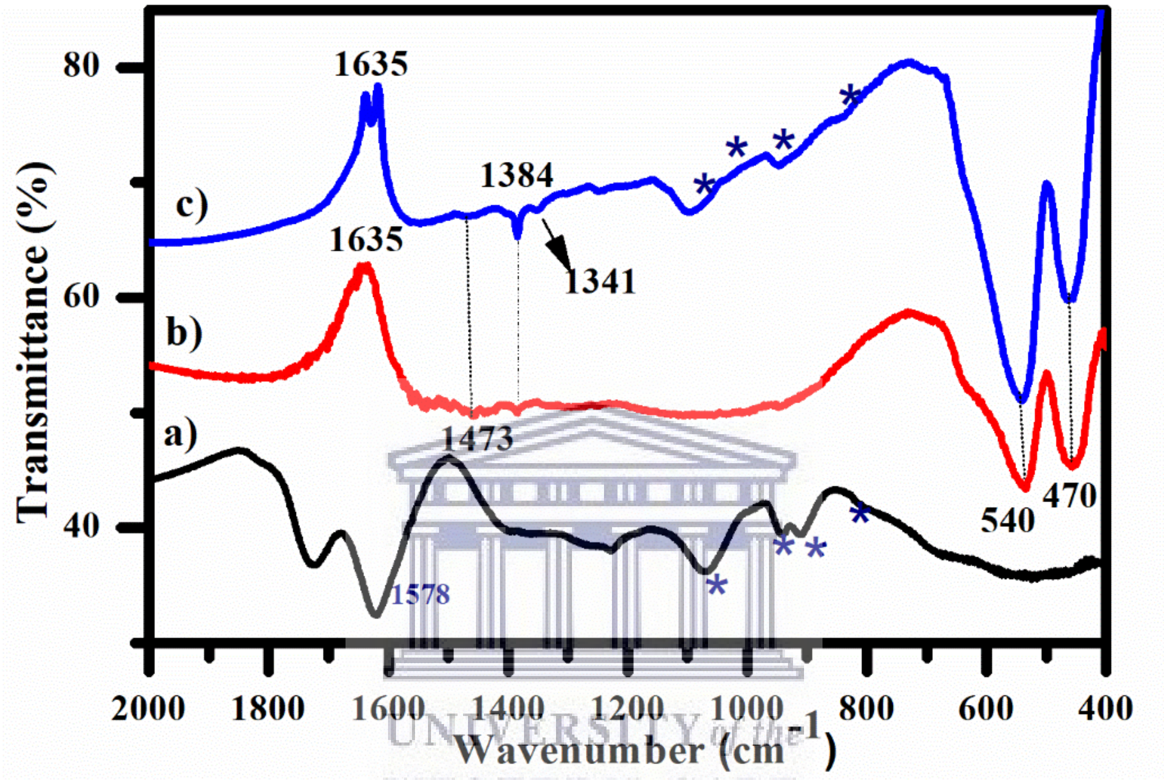

Figure 4.15: FTIR spectra of (a) POM/RGO, (b) Ag-Fe_2O_3 nanoparticles and (c) novel Ag-Fe_2O_3/POM/RGO nanocomposite.

FTIR spectroscopy was used to investigate the structural change in bonding related to a) POM/RGO, b) Ag-Fe_2O_3 and c) novel Ag-Fe_2O_3/POM/RGO composites as shown in **Figure 4.15**. The POM/RGO and Ag-Fe_2O_3 composites were included for comparison sake. In the spectrum b) of Ag-Fe_2O_3 strong absorption bands at 540 cm^{-1} and 470 cm^{-1} attributed to the Fe-O bond are observed (Xiao et al., 2015; Hu et al., 2018). These absorption bands are still present in spectrum c) of Ag-Fe_2O_3/POM/RGO but are more sharp. In addition, the peak at 540 cm^{-1} can be credited to the lattice absorption of iron oxide, indicating the strong interaction of the nanoparticles with the ester O. The absorption peaks (1071 cm^{-1}, 928 cm^{-1}, 847 cm^{-1} and 670 cm^{-1}) in spectrum a) of POM/RGO are also present (1098 cm^{-1}, 941 cm^{-1}, 840 cm^{-1} and 709 cm^{-1}) in spectrum c) but with slight shifting. These are due to the oxygen functional groups in POM/RGO interacting with the Fe_2O_3 nanoparticles (Zhang & Zheng, 2017). From the Ag-Fe_2O_3 spectrum b), the weak absorption bands at 1473 cm^{-1} and 1384 cm^{-1}, 1635 cm^{-1} are mainly responsible for reduction of Ag. These peaks are also present in the novel nanocomposite spectrum, with the absorbance band at 1384 cm^{-1} being associated with the stretch vibration of functional groups such as -C-O-C-, -C-O-, -C=C, C=O (Press, 2011; Geetha Bai et al., 2016). These values are in agreement with reported literature and hence confirm the formation of the novel composite.

4.3.3 X-ray Diffraction (XRD)

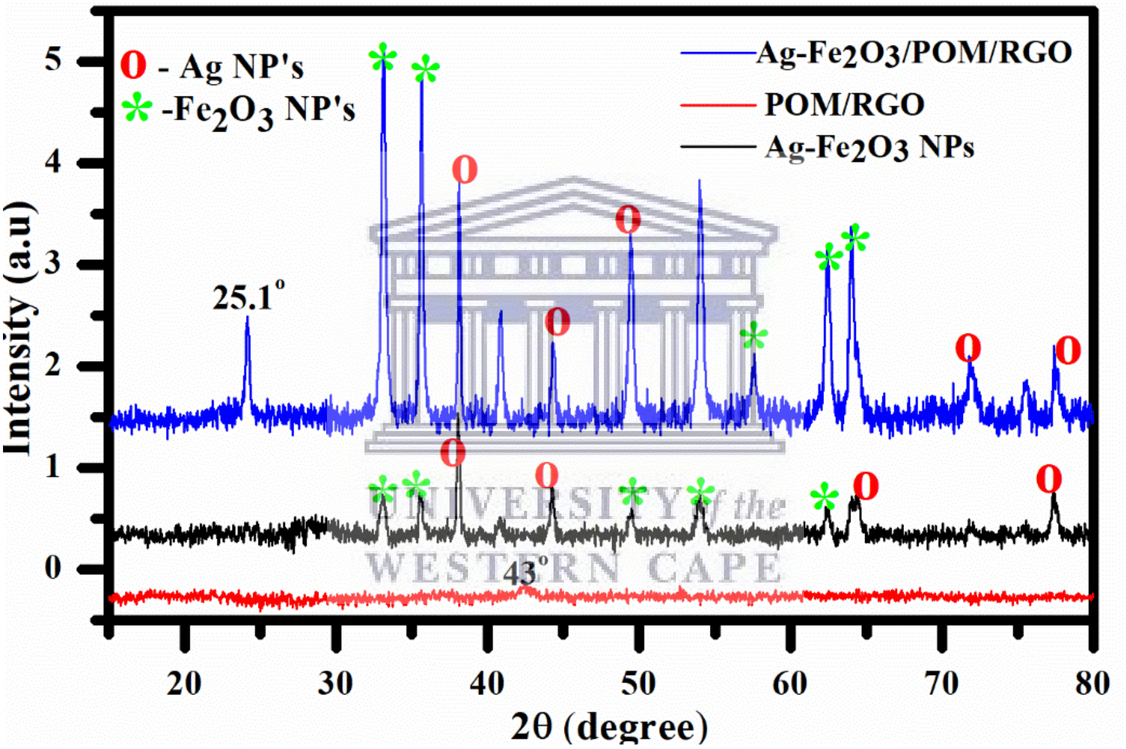

Figure 4.16: XRD patterns of POM/RGO, Ag-Fe_2O_3 nanoparticles and Ag-Fe_2O_3/POM/RGO.

The chemical components and the crystalline structure of the novel Ag-Fe_2O_3/POM/RGO nanocomposite was investigated using XRD as shown in **Figure 4.16**. For comparison the XRD patterns of Ag-Fe_2O_3 nanoparticles and POM/RGO were also included. As shown above, the curve of Ag-Fe_2O_3/POM/RGO consists of peaks with 2Ɵ values of 30.3°, 35.6°, 58.7°, 62.9° and 53.7° which are assigned to diffraction from the (220), (311), (400), (422) and (533) planes of rhombohedral crystalline lattice Fe_2O_3 phase (JCPDS card no 33-0664) (Hu et al., 2018). Meanwhile, five peaks diffraction peaks at 38.1°, 44.4°, 48.9°, 77° and 79.4° well indexed to (111), (200), (220), (311) and (222) planes of Ag cubic structure (JCPDS card no 04-0783)

(Zhang & Zheng, 2017). Additionally, the intensities of the diffraction peaks are increased in the novel nanocomposite and the diffraction peaks are slightly shifted this might be due to the interaction between oxygen functional groups of POM/RGO and Fe_2O_3. In comparison with the POM/RGO pattern, the diffraction peak of POM/RGO is not observed in the Ag-Fe_2O_3/POM/RGO indicating that the surface is fully decorated by Ag-Fe_2O_3 nanoparticles (Aal, Ionov & Alim, 2018). On the basis of the XRD results in can be concluded that the novel nanocomposite was successfully synthesized.

4.3.4 Raman Spectroscopy

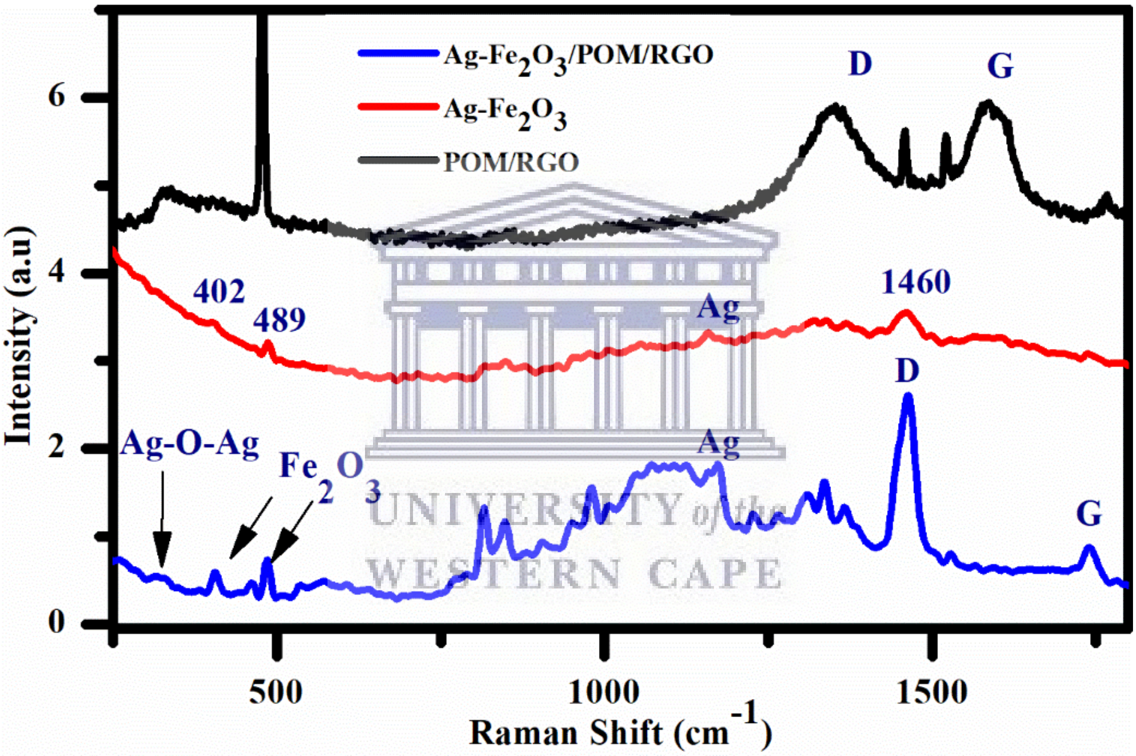

Figure 4.17: Raman spectra of POM/RGO, Ag-Fe_2O_3 nanoparticles and novel Ag-Fe_2O_3/POM/RGO obtained using excitation wavelength of 533 nm, 632.8 and 632.8 respectively.

From the Raman spectra on **Figure 4.17** of Ag-Fe_2O_3/POM/RGO the D and G band of shows a bathochromic shift from 1352 cm^{-1} to 1466 cm^{-1}, and from 1593 cm^{-1} to 1733 cm^{-1}, respectively. The I_D/I_G band of the Ag-Fe_2O_3/POM/RGO is (2.488) higher compared to that of (1.27) POM/RGO indicating the presence of sp_3 defects with the sp_2 carbon network after the hydrothermal method in the novel composite (Liu et al., 2015b). In the 200-600 cm^{-1} range, from the spectrum of Ag-Fe_2O_3 nanoparticles, the characteristic Fe-O bands of Fe_2O_3 are observed, which are centred at 402 cm^{-1} and 408 cm^{-1}. These peaks can also be observed from the spectrum of Ag-Fe_2O_3/POM/RGO but with a slight shifting to 403 cm^{-1} and 483.70 cm^{-1}, which confirm the formation of Fe_2O_3 nanoparticles in the novel composite (Kumar et al., 2017). The Ag-Fe_2O_3/POM/RGO results also showed a vibration band at 281 cm^{-1} that can be assigned to an Ag-O mode and a vibration band at 1117 cm^{-1} for Ag mode (Van der Horst et al., 2015). These confirm the success of the hydrothermal synthesis of Ag-Fe_2O_3/POM/RGO composite.

4.3.5 Transmission Electron Microscopy (TEM)

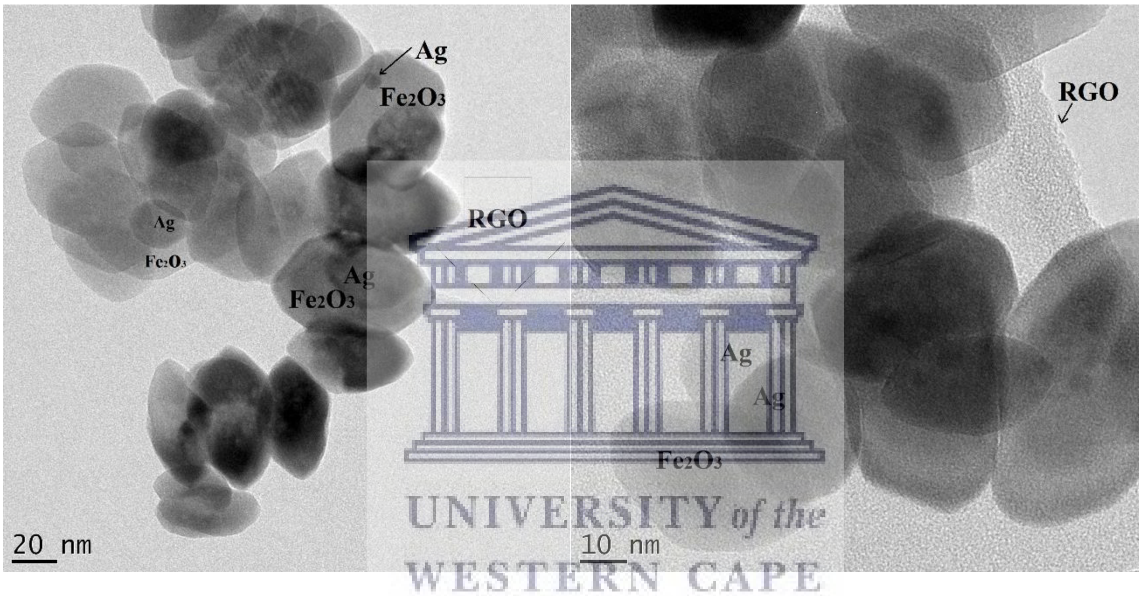

Figure 4.18: TEM images of the novel Ag-Fe_2O_3/POM/RGO composite at different magnifications.

TEM was used to study the surface morphology and the size distribution of the novel Ag-Fe_2O_3/POM/RGO nanocomposite. The conditions for obtaining TEM images were discussed in **Chapter 3**. **Figure 4.18** show the TEM images of the Ag-Fe_2O_3/POM/RGO at different magnifications. From the TEM image it can be seen that the Fe_2O_3 and Ag nanoparticles are distributed onto the RGO sheet. **Figure 4.18** show irregular shaped particles of Fe_2O_3 with diameter 16 nm and Ag nanoparticles of 3 nm. The particle sizes were calculated using a Java-based image processing programming known as “ImageJ”. These nanoparticles have less uniform dispersion with a slight agglomeration. This aggregation might be caused by longer reaction time of the hydrothermal method chosen to prepare the novel composite, leading to bad dispersion (non-uniform) of the nanoparticles on the POM/RGO surface (Paul et al., 2016).

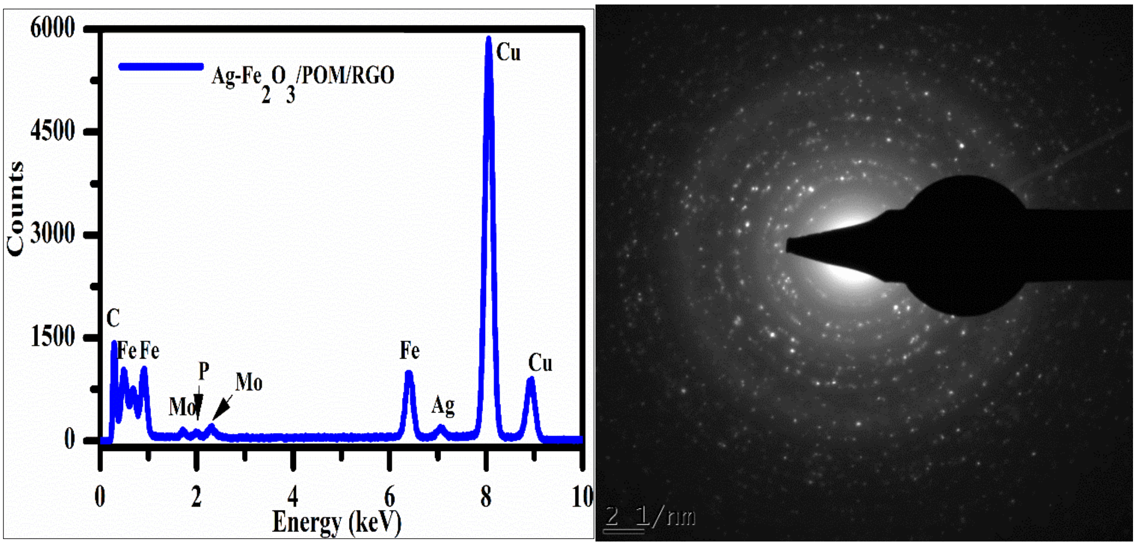

Figure 4.19: EDX spectroscopy of the novel composite (left) and Selected area (electron) diffraction (SAED) of Ag-Fe_2O_3/POM/RGO nanocomposite.

The chemical component and the structure of Ag-Fe_2O_3/POM/RGO was examined using EDX as shown in **Figure 4.19**. The EDX pattern of the novel composite suggested that the sample is composed of the elements listed in **Table 4.2**, which confirm the formation of the novel composite. The copper peak observed in the EDX of the sample is due to the copper grid that was used (as explained in chapter 3). No other impurity element was observed, indicating the purity of the novel material. The SAED patterns suggest that the as prepared Ag-Fe_2O_3/POM/RGO has high crystallinity.

Table 4.2: Elements and their corresponding weight % obtained from the EDX of the novel nanostructured material.

Elements	Weight %
C	5.57
O	20.25
P	1.1
Mo	4.23
Ag	18.24
Fe	50.61

4.3.6 Scanning Electron Microscopy (SEM)

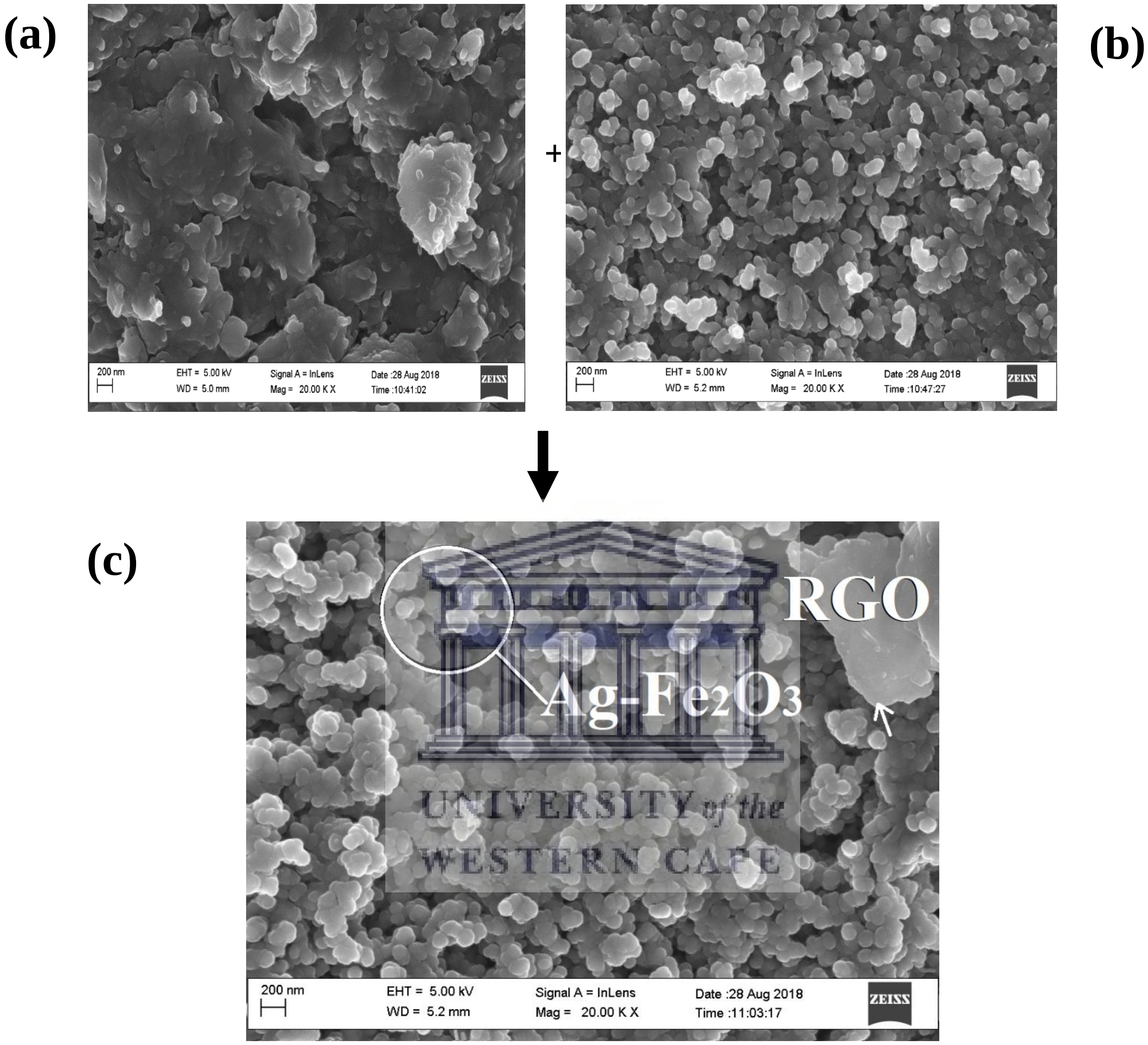

Figure 4.20: SEM images of (a) POM/RGO, (b) Ag-Fe_2O_3 nanoparticles and (c) Ag-Fe_2O_3/POM/RGO.

The morphology of Ag-Fe_2O_3/POM/RGO nanocomposite was investigated by SEM as shown if **Figure 4.20** (c). For comparison, SEM images of (a) POM/RGO and (b) Ag-Fe_2O_3 were included. **Figure 4.20** (c) showed a RGO sheet, this was absent in the Ag-Fe_2O_3, indicating that in (c) Ag-Fe_2O_3 nanoparticles were dispersed onto the POM/RGO surface.

4.3.7 Small angle x-ray scattering (SAXS)

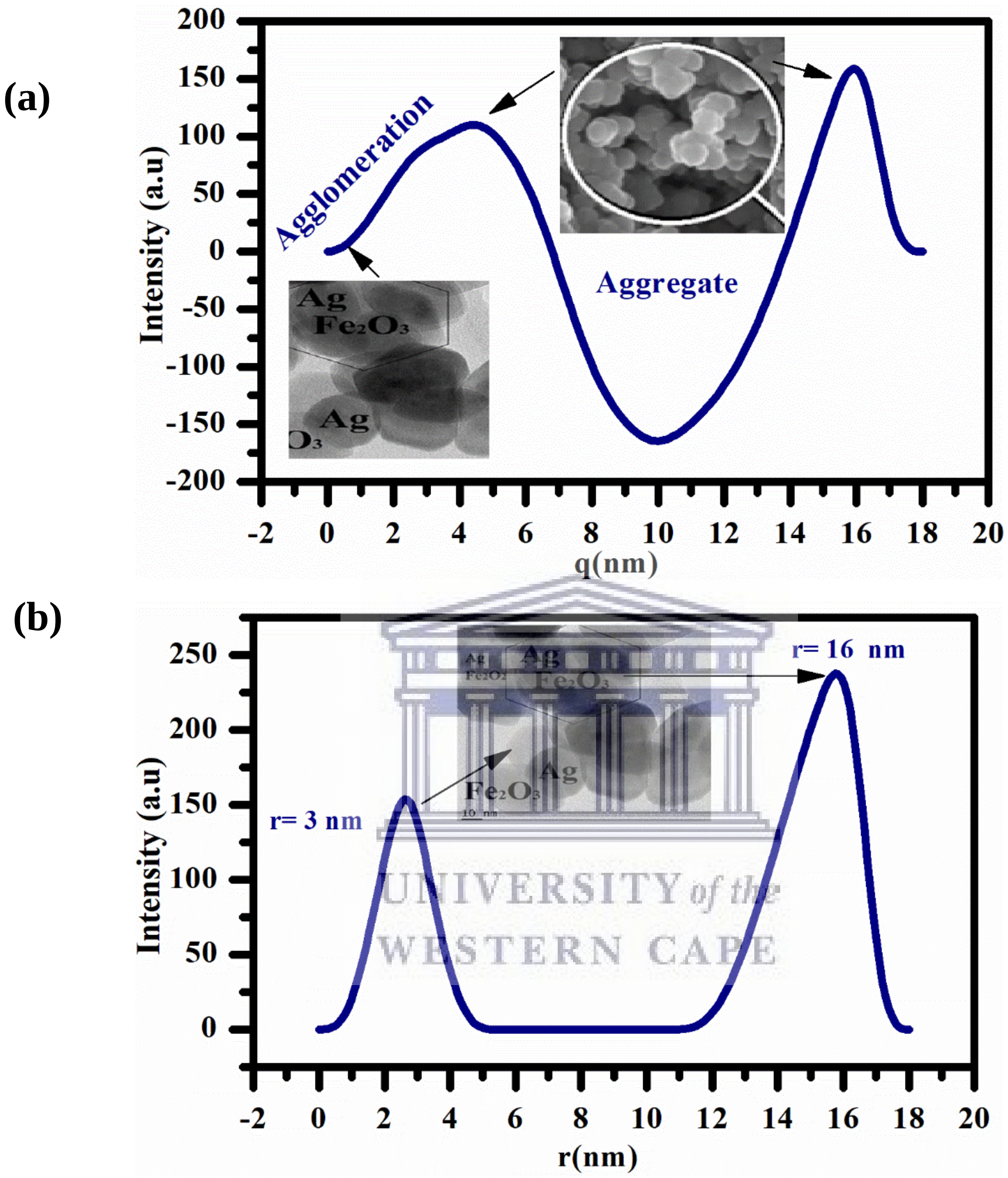

Figure 4.21: SAXS analysis of Size distribution of the Ag-Fe_2O_3 nanoparticles on the Ag-Fe_2O_3/POM/RGO nanocomposite by intensity (b). Inset TEM image at 10 nm showing the Ag-Fe_2O_3/POM/RGO. (a) size distribution from SAXS in terms of distribution by volume. Inset plot SEM and TEM images showing the Ag-Fe_2O_3/POM/RGO composite.

SAXS was used to determine the structure of the Ag-Fe_2O_3 nanoparticles in the Ag-Fe_2O_3/POM/RGO novel nanocomposite. **Figure 4.21 (a)** shows the size distribution of the Ag-Fe_2O_3 nanoparticles in terms of volume. The SAXS of the composite shows a dip which goes to negative values, this indicates that the nanoparticles are inhomogeneous. Moreover, there is a second peak in the graph at about 16 nm, after the dip, this second peak tells us that the particles are aggregates, i.e. (they stick together). These results correlates with the insert SEM and TEM images which show that the particles are not core-shell but they are sticking together. In **Figure 4.21** (b) the size distribution is in terms of intensity, this indicated that the nanoparticles with sizes 16 nm are more intense compared to the 3 nm ones (Schnablegger & Singh, 2013). TEM image was inserted to show that the Fe_2O_3 nanoparticles which were calculated by "ImageJ" to be in the range of (15-16) are the more intense.

4.3.8 Cyclic voltammetry (CV)

To conduct CV measurements 1 mg of Ag-Fe_2O_3/POM/RGO was dispersed in 1 ml ethanol solution to generate a homogeneous mixture black suspension. Subsequently, 3 µl of the suspension was dropped onto a GCE and dried at room temperature to form Ag-Fe_2O_3/POM/RGO/GCE. **Figure 4.22 (**a) shows the CV of Ag-Fe_2O_3/POM/RGO modified GCE in 0.5 M H_2SO_4 solution at scan rates from 10 mV/s to 100 mV/s. From the graph is can be observed that as the scan rate increase, there is also an increase in current, this behaviour was plotted in the inset graph to calculate the diffusion coefficient. The CV of the novel composite was determined to be reversible from **equation 4.1** using the parameters on **Table 4.3** . The CV shows three redox peaks, two anodic peaks and one cathodic peak.

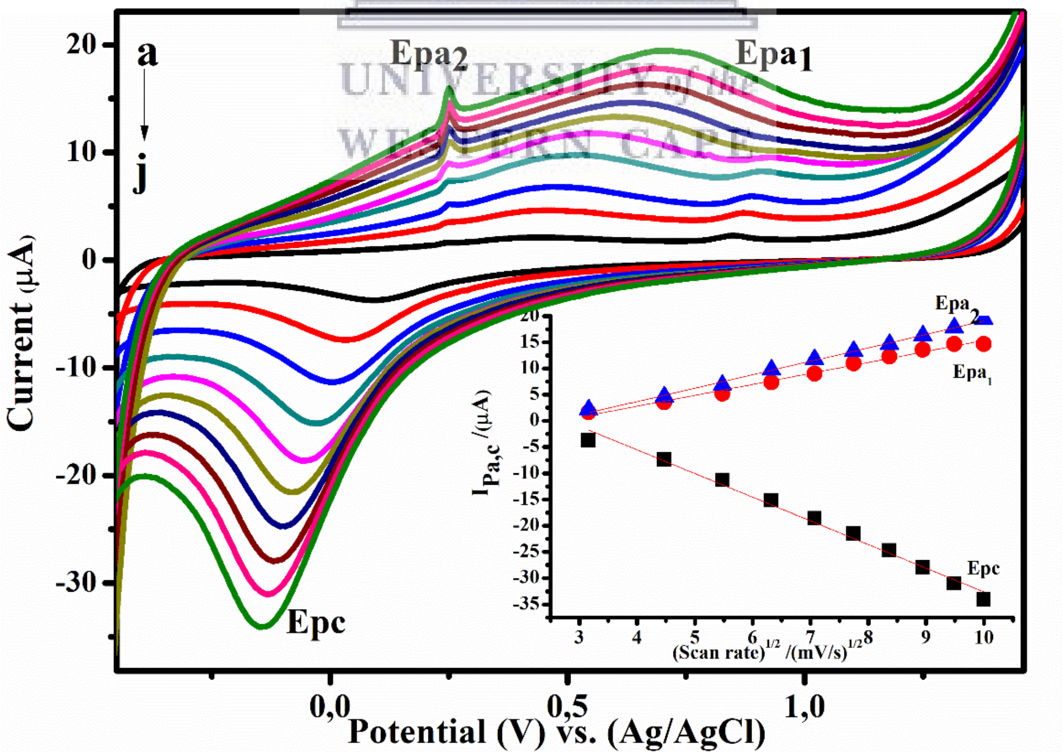

Figure 4.22: (a) CV of Ag-Fe_2O_3/POM/RGO/GCE (a) in 0.5 M H_2SO_4 solution with different scan rate from a to j (10, 20,30,40,50,60,70, 80, 90 and 100 mVs^{-1}). Inset Randles-Sevcik plot of current vs (scan rate)$^{1/2}$.

Oxidation potential at 0.25 V corresponds to the reaction of $Ag^0 \rightarrow Ag^+ + 1e^-$ (Liu, Zhu, et al., 2012). This anodic peak is proportional to the scan rate with the regression equation of $I_{p2}(\mu A) = 2.5659\ (\frac{mV}{s})^{\frac{1}{2}} - 6.517$, R^2= 0.988. This behaviour indicates that the redox process is surface controlled, and that the Ag nanoparticles are on the surface of the POM/RGO sheets (Olga S. Ivanova & Francis P. Zamborini, 2010). This anodic peak is in agreement with the Ag nanoparticles in the literature (Van der Horst et al., 2015). A well-defined redox peak Epa_1 and Epc were observed at 0.579 V and -0.080 V which corresponds to the Fe^{3+}/Fe^{2+}(Liu et al., 2017). It is worth noting that the obvious peaks in the CV of the composite confirm that the reaction arising from Fe_2O_3 nanoparticles makes a major contribution on the sensors performance. The diffusion coefficient of the nanocomposite was calculated to be 0.000235 cm^2/s, indicating that the Ag-Fe_2O_3 nanoparticles on the surface of the RGO sheets is improved. On the other hand, there were no peaks observed for the POM.

Table 4.3: Showing parameters obtained from the CV of Ag-Fe_2O_3/POM/RGO

Scan Rate (mV.s-1)	Scan Rate1/2 (mV.s-1)	Epa_1 (V)	Ipa_1 (μA)	Epa_2 (V)	Ipa_2 (μA)	Epc (V)	Ipc (μA)	ΔEp (V)
10	3.16	0.429	2.120	0.249	1.623	-0.089	-3.72	0.518
20	4.47	0.449	4.620	0.249	3.530	-0.029	-7.39	0.478
30	5.48	0.469	6.82	0.249	5.226	-0.009	-11.22	0.478
40	6.32	0.529	9.77	0.249	7.390	-0.031	-15.16	0.560
50	7.07	0.559	11.79	0.249	9.001	-0.061	-18.62	0.620
60	7.75	0.620	13.63	0.250	10.99	-0.089	-21.49	0.709
70	8.37	0.645	14.63	0.250	12.28	-0.099	-24.71	0.744
80	8.94	0.680	16.28	0.250	13.60	-0.120	-27.95	0.800
90	9.49	0.695	17.78	0.250	14.65	-0.130	-31.03	0.825
100	10.0	0.715	19.45	0.250	14.65	-0.145	-34.08	0.860
Mean		0.579	11.69	0.250	9.294	-0.080	-19.54	0.659

Determination of reversibility:

$$Ip(a) = Ip(c) \qquad \textbf{(4.1)}$$

$$\frac{Ip_{a1}}{Ip_{c1}} = \frac{11.69\ \mu A}{-19.54\ \mu A} = 0.59 \approx 1$$

$$\therefore\ chemically\ reversible$$

Determination of diffusion coefficient:

$$Ipa = (2.69x10^5)n^{3/2}A[C]D^{1/2}V^{1/2} \qquad \textbf{(4.2)}$$

$$Sope == (2.69x10^5)n^{3/2}D^{1/2}$$

$$\therefore D^{1/2} = \frac{Slope}{(2.69x10^5)A[C]n^{3/2}}$$

$$\therefore D^{1/2} = \frac{Slope}{(2.69x10^5)A[C]n^{3/2}}$$

$$D^{1/2} = \frac{2.0939\,\frac{\mu A}{(s/mV)^{1/2}}}{(2.69x10^5)(0.283\ cm^2)[500\ mol \cdot cm^3](1)^{3/2}}$$

$$D = 0.000235\ cm^2/s$$

4.3.9 Electrochemical Impedance Spectroscopy

In order to analyze the impedance changes of the modified electrode, Electrochemical Impedance Spectroscopy was employed. **Figure 4.23** depicts the Nyquist plots in 0.5 M H_2SO_4 solution. The Nyquist plot of the impedance spectra consists of semicircle portion which at higher frequencies correlates to the electron transfer limited process, while on the other hand, a linear portion at lower frequencies correlates to the diffusion process. The electron transfer resistance (Rct) can be evaluated by using the semicircle diameter. In order to figure out the impedance parameters, the Zview 2 software is employed in the simulations. The Rs(CPE[RctW]) equivalent circuit model was employed in the simulation of the impedance behaviour of all the modified electrodes, from the experimentally gained impedance data. By exploiting the series components, the model was developed. The first component is ohmic resistance of the solutions (Rs) and the second one is a set of constant phase elements (CPE) and the resistance of layer (Rct). Rct indicates the conductivity of the samples that are in the parallel position with CPE. Additionally, from the diffusion impedance, W which stands for the Warburg element is a series connection to Rct. **Table 4.4** shows the obtained data of all modified electrodes. The size of the semicircle domain and there Ret value was increased. This confirms that the presence of RGO and the Ag-Fe_2O_3 nanoparticles on the surface of the electrode limits the electron-transfer on the electrochemical probe. It can be seen from the table that the novel composite compared to the others decreases suggesting that the nanoparticles were successfully synthesized in the electrode surface (Teymourian, Salimi & Khezrian, 2013).

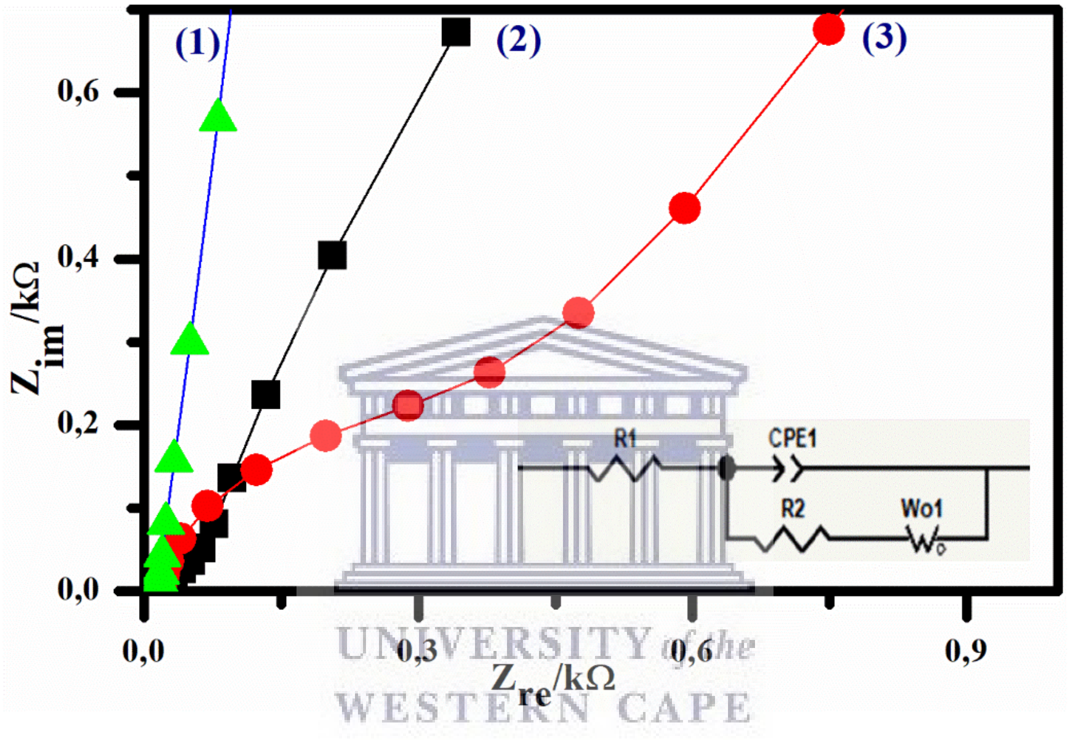

Figure 4.23: (a) Nyquist plot of (1) Ag-Fe_2O_3 nanoparticles, (2) POM/RGO and (3) Ag-Fe_2O_3/POM/RGO novel nanocomposite. Insert plot is the Randels fitted circuit of Ag-Fe_2O_3/POM/RGO and the fitted circuit.

Table 4.4 Summary of electrochemical impedance spectroscopy simulations with fitted circuit element parameters in 0.5 M H_2SO_4 solution.

Electrode material	R_s(Ω)	CPE	R_{ct}(Ω)	W_O	Error %
POM/RGO	12.61	0.96067	545230	-	0.096
Ag-Fe_2O_3 Nps	15.7	0.93366	813450	-	0.233
Ag-Fe_2O_3/POM/RGO	18.22	0.96354	700.5	0.32	1.430

CHAPTER 5

Ag-Fe_2O_3/POM/RGO NANOCOMPOSITE AS A PLATFORM FOR H_2O_2 SENSOR

Chapter overview

This chapter describes hydrogen peroxide (H_2O_2) detection using the novel Ag-Fe_2O_3/POM/RGO nanocomposite as a platform for enzyme-less electrochemical sensor in PBS and different water samples. The developed electrochemical sensor based on Ag-Fe_2O_3/POM/RGO showed unique characteristics towards H_2O_2 detection, which were first investigated by cyclic voltammetry (CV). And then the amperometric response to H_2O_2 measured at -0.67 V (vs. Ag/AgCl) by Ag-Fe_2O_3/POM/RGO modified glassy carbon electrode (GCE). The calibration curves were found to be linear from 0.3 mM to 3 mM (R) with the detection limit of 0.0029 mM (S/N=4). The selectivity was evaluated in water from different dam/rivers in the presence and absence of H_2O_2.

5.1 Cyclic voltammetry detection of H_2O_2 (CV)

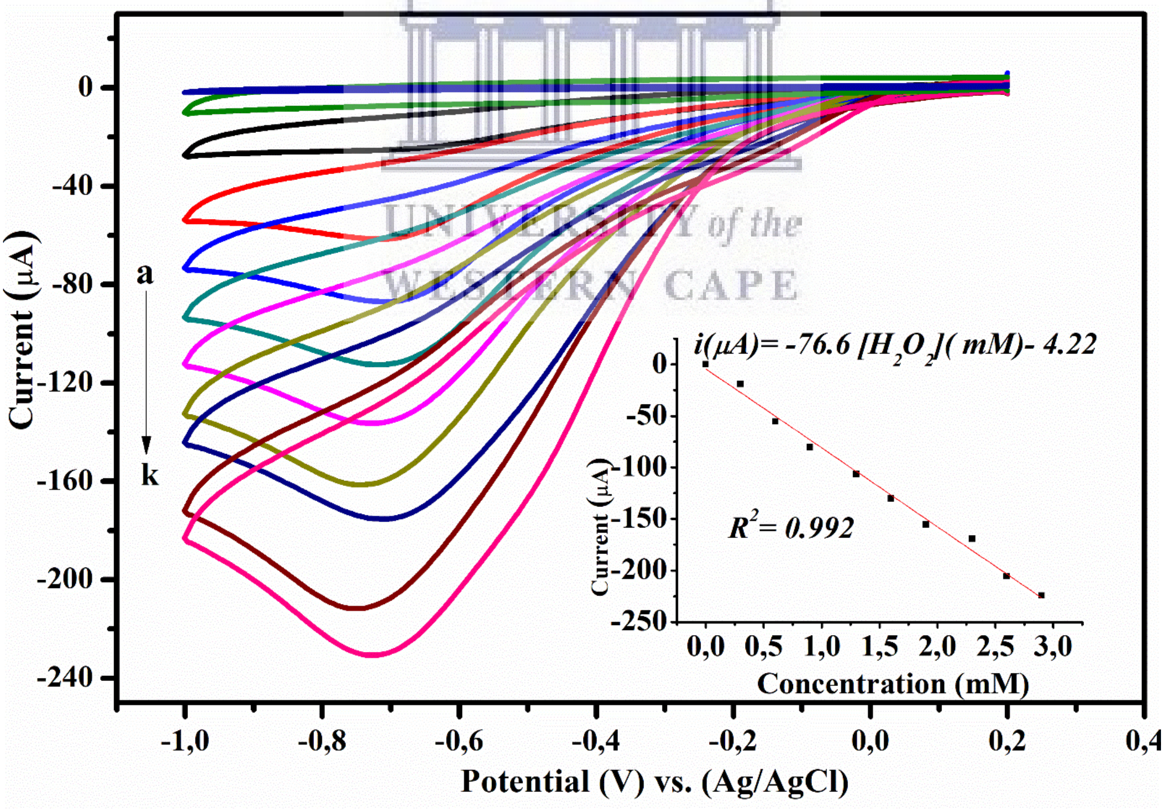

Figure 5.1: Cyclic voltammetry of H_2O_2 obtained by Ag-Fe_2O_3/POM/RGO/GCE in N_2 saturated stirring 0.1 M PBS (pH 6.8) (concentration of H_2O_2 from a → k: 0, 0.3, 0.6, 0.9,

1.3,1.6, 1.9, 2.3, 2.6, 2.9 mM) at scan rate of 0.03 V/s and bare GCE. *Insert* plot of catalytic current of H_2O_2 versus H_2O_2 concentrations.

For the sake of evaluating the electrocatalytic performance of the sensor, cyclic voltammetry was used to obtain some parameters. Electrocatalytic reduction of Ag-Fe_2O_3/POM/RGO/GCEE and GCE are shown in **Figure 5.1**. The catalytic activity of Ag-Fe_2O_3/POM/GCE is evidently better than that of GCE. **Figure 5.1** shows that the CV of Ag-Fe_2O_3/POM/RGO/GCE in N_2-saturated 0.1 M PBS (pH 6.8) at 30 mV/s scan rate exhibits the highest electro reduction activity towards H_2O_2 detection. In the absence of H_2O_2, the CV (curve b) of Ag-Fe_2O_3/POM/RGO/GCE is quite similar to the bare electrode (curve a). However, as can be seen from the CV curve c), with the addition of H_2O_2, a reduction peak appeared at -62 mV/s, corresponding to the reduction of H_2O_2. The influence of concentration on the CV results of Ag-Fe_2O_3/POM/RGO/GCE at 30 mV/s scan rate was then studied. It was found that when 0, 0.3 0.6, 0.9, 1.3, 1.6, 1.9, 2.3, 2.6, 2.9 mM concentration of H_2O_2 were added the reduction potentials were shifted to more negative values indicating an irreversible reduction process and the current responses were increased obviously (Zhang & Zheng, 2017). It was found that the reduction of H_2O_2 on Ag-Fe_2O_3/POM/RGO/GCE surface had diffusion controlled electron transfer process since the cathodic peak current showed a linear relation with the square roots of the concentrations (Qi & Zheng, 2016). This relationship is shown as the insert plot of **Figure 5.1** with R^2= 0.992 and a linear relation of $I(\mu A) = -76.6[H_2O_2](mM) - 4.22$. These results showed that the composite exhibited notable catalytic performance for reduction of hydrogen peroxide. The optimum working potential for H_2O_2 reduction on Ag-Fe_2O_3/POM/RGO surface was determined by measuring the response current of the electrodes at various working potentials ranging from 0 to -1.0 V.

5.2 Sensor optimization

From the mentioned experimental results, it can be confirmed that H_2O_2 can be electrochemically reduced in the presence of Ag-Fe_2O_3/POM/RGO on the surface of the GCE . To develop the performance of the sensor, various factors influencing the current response of the sensor were investigated. In order to find the best potential, the relationship between the reduction current of H_2O_2 and the applied potential was measured. Finally, -0.67 V was selected from the CV results as the optimized potential and used to conduct amperometric detection of H_2O_2.

5.3 Amperometric detection of H_2O_2

Figure 5.2 shows the amperometric responses of the Ag-Fe_2O_3/POM/RGO modified GCE at -0.67 V versus SCE as a result of the successive addition of H_2O_2 to the continuously stirred 0.1 M PBS solution (pH 6.8) at 25 °C. The experiments were carried out with freshly prepared electrodes. As shown in **Figure 5.2**, the Ag-Fe_2O_3/POM/RGO was very sensitive to the changes in the concentration of H_2O_2 and responded rapidly. The response time was fast (less than 5 s) and with increasing the concentration of H_2O_2 from 0.3 mM to 3 mM, the current increased linearly. In calibration curve, the sensor shows linear section for the response to H_2O_2 with the linear regression equation of $I = -82.88\ (\mu A.\ mM^{-1}) + 2.3$ ($R^2 = 0.9921$) with relative standard deviation (RSDs) of 1.8 % for n = 4. The limit of quantification (LOQ) and the limit of detection (LOD) of Ag-Fe_2O_3/POM/RGO were determined by using the following equations:

$$LOD = \frac{3S_D}{b} \qquad \textbf{(5.1)}$$

$$LOQ = \frac{10S_D}{b} \qquad \textbf{(5.2)}$$

where b is the slope of the calibration curve and S_D is the standard deviation of the blank solution as shown in **Figure 5.2** (inset). The LOD and LOQ are calculated to be 0.0029 mM and 0.0098 mM, respectively. As listed in **Table 5.1**, the detection limit, linear range and the sensitivity of Ag-Fe_2O_3/POM/RGO is near most of the other modified electrocatalytic materials.

Table 5.1: Comparison of the performance of the Ag-Fe_2O_3/POM/RGO sensor with recent reported sensor

Electrode modification	Sensitivity ($\mu A\ mM^{-1}cm^{-2}$)	Linear range (mM)	Detection limit (mM)	Ref
Ag /MnOOHRGO	-	0.5µM-17.8 mM	0.2µM	(Bai et al., 2014)
POM/RGO	95.6	100 µM-20mM	1.02 µM	(Yang et al., 2016a)
Ag/Fe_2O3	134.5	0.5 µM- 4. 0 mM	0.2 µM	(Qi & Zheng, 2016)
Ag-Fe_2O_3/POM/RGO	270.96	0.3 – 3.3	0.0029	This work

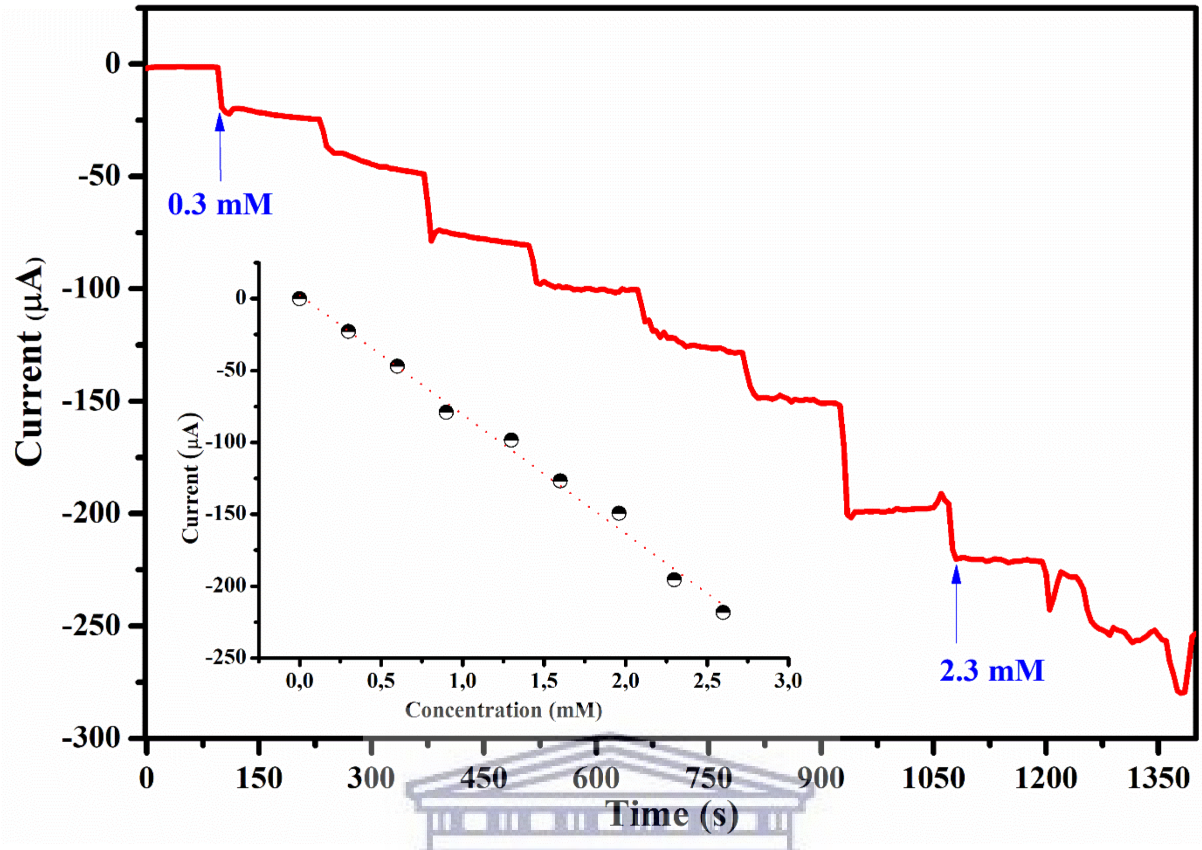

Figure 5.2: Current–time responses of Ag-Fe_2O_3/POM/RGO with the subsequent addition of H_2O_2 into 0.1 M PBS (pH 6.8) at -0.5 V; (Inset) Calibration curve.

5.4 Selectivity and stability studies

In order to explore the selectivity and anti-interference advantages of the sensor, the effect of the presence of molecules, which are well known interferants to the detection of hydrogen peroxide, on the sensor performance, were investigated. It is known that the presence of these species results in a significant change in the response current of the sensors due to their highly electroactive nature, especially at relatively high working potentials. Therefore, it is imperative to have minimum interference effect to detect H_2O_2 concentration correctly. The *i*-t curve of Ag-Fe_2O_3/POM/RGO obtained by the consecutive injection of H_2O_2, uric acid (UA), glucose and ethanol which are considered common interfering species (Yang et al., 2016a) into 0.1 M PBS at pH 6.8 at a working potential of -0.67 V *vs*. SCE is shown in **Figure 5.3**. When 0.3 mM of H_2O_2 was added, the current response increased significantly. However, after injecting uric acid (UA), glucose and ethanol the response current was almost unchanged. While the equal concentration of H_2O_2 was added again, the response increased significantly. As can be seen, the mentioned electroactive interfering species is quite negligible which indicates that Ag-

Fe_2O_3/POM/RGO has superior selectivity toward H_2O_2. The use of negative working potential, -0.67 V, allowed us to construct interference free Ag-Fe_2O_3/POM/RGO sensor.

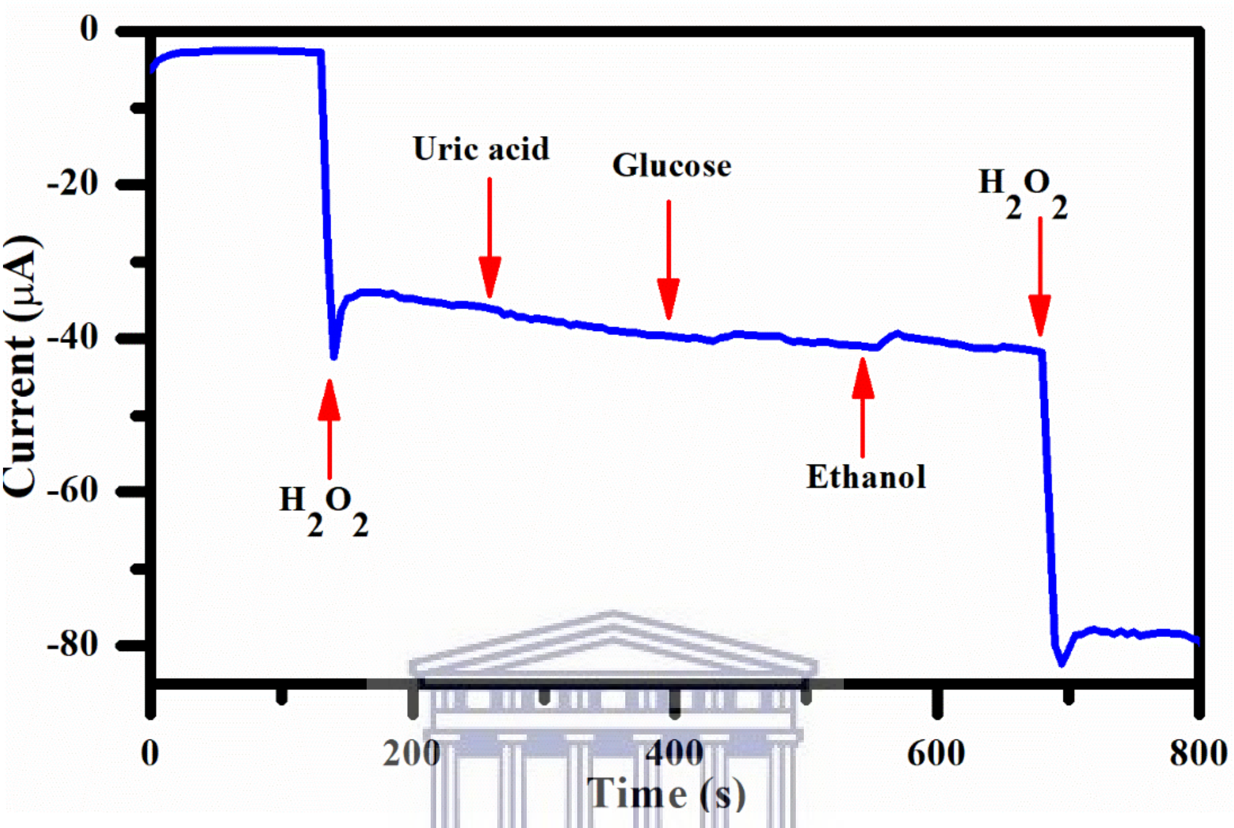

Figure 5.3: Amperometric response of Ag-Fe_2O_3/POM/RGO upon the successive addition of 0.3 mM H_2O_2, uric acid, glucose, and ethanol into 0.1 M PBS (pH 6.8) with an applied potential -0.67 V.

5.4 Repeatability, reproducibility and stability

The reproducibility, repeatability and stability of the prepared sensor were studied. The long term stability of Ag-Fe_2O_3/POM/RGO sensor was determined by measuring the analytical response towards addition of 0.3 mM H_2O_2 concentration in PBS periodically. The modified electrode was stored in the fridge at 4° when not in use and the current was monitored periodically for 15 days in a course of three weeks and the results were plotted in **Figure 5.4**. During the first week, the current response showed no considerable decrease, as it can be seen from **Figure 5.4**, after three weeks the sensor retained about 82 % of its initial response, showing its excellent long term stability. In order to determine the reproducibility of the sensor, five modified electrodes were prepared under the same conditions and the RSD for the current response towards 0.3 mM H_2O_2 was found to be 1.81 % confirming that the results are reproducible. The RSD of one sensor for 5 successive assays in determining the current response towards 0.3 mM H_2O_2 was 2.53 %. Hence its repeatability was good.

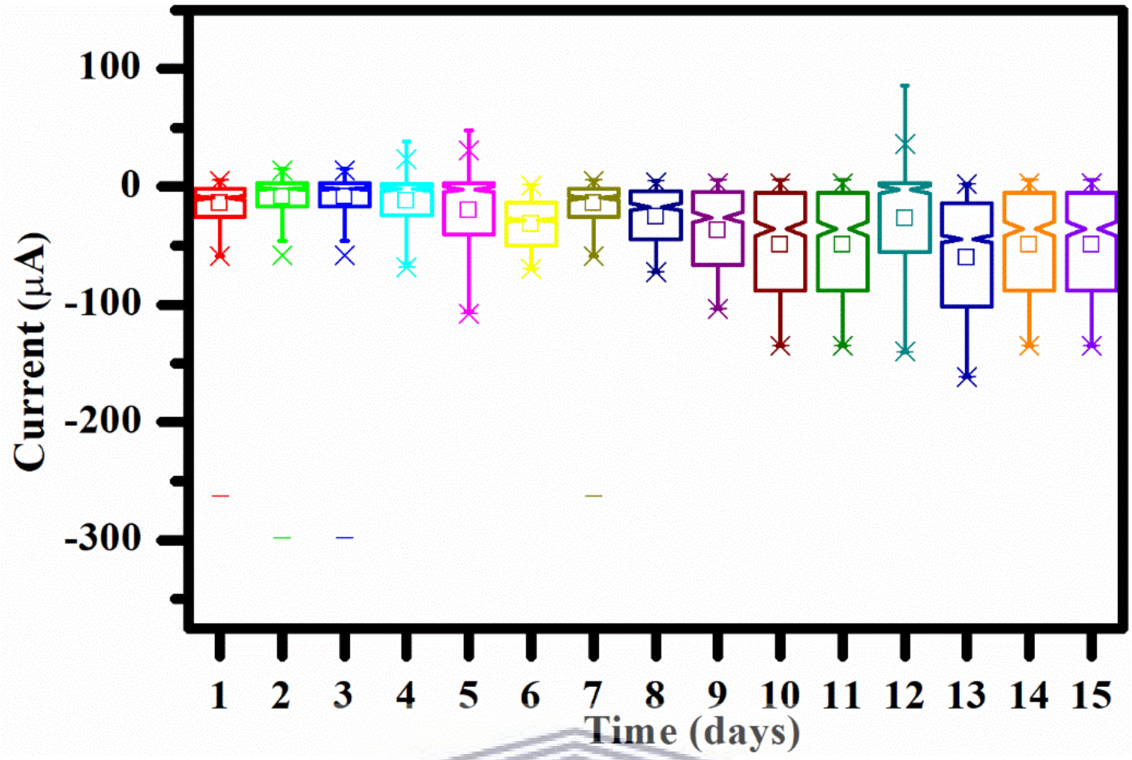

Figure 5.4: Long term stability of Ag-Fe_2O_3/POM/RGO stored at 4 °C studied over 15 days in PBS at pH 6.8 with addition of 0.3 mM H_2O_2 concentration at -0.67 V.

5.5 Practical application of the Ag-Fe_2O_3/POM/RGO sensor

Table 5.2: Analysis of real sample with sensor at different H_2O_2 concentration

Sample	Added [H_2O_2]/ mM	Detected [H_2O_2]/mM	Recovery %	RSD (n=3) %
Bellville WWTP	0	undetected	undefined	undetected
	0.2	0,205	97.56	2,439
	0.3	0,307	97.72	2,178
	0.4	0,411	97.32	1,931
Kuils river system	0	undetected	undefined	undetected
	0.2	0,224	89.28	3,802
	0.3	0,299	100.3	3,857
	0.4	0,421	95.01	2,468
Bera river	0	undetected	undetected	undetected
	0.2	0,223	89.70	4,391

	0.3	0,254	118.1	3,174
	0.4	0,437	91.53	3,121
Somerset Earth dam	0	undetected	undefined	undetected
	0.2	0,212	94.34	1,364
	0.3	0,308	97.40	3,376
	0.4	0,421	95.01	0,961
Tygerberg reservoir	0	undetected	undefined	undetected
	0.2	0,214	93.46	2,812
	0.3	0,314	95.54	1,507
	0.4	0,412	97.09	1,832
Lounens river raw Somerset	0	undetected	undefined	undetected
	0.2	0,210	95.24	4,167
	0.3	0,299	100.3	3,618
	0.4	0,413	96.85	1,558
UWC sports ground	0	undetected	undefined	undetected
	0.2	0,215	93.02	1,631
	0.3	0,306	98.04	0,999
	0.4	0,405	98.77	1,928

To measure the repeatability, reproducibility and stability of the chemical sensor, seven water samples from different rivers, dams, reservoirs (**Table 5.2**) were used as real samples for performing the detection of H_2O_2. The determination of H_2O_2 in the water samples was carried out on the Ag-Fe_2O_3/POM/RGO novel nanocomposite chemical sensor. Initially the water samples were measured without adding H_2O_2 solution. Later H_2O_2 solutions were successfully added to the systems in order to determine the current response through standard addition method. To establish the performance of the sensor in real-life water analysis, we investigated its response to wastewater samples. There is still a pressing need to develop new strategies that couple with the concentration usually found in the contaminated water sites. The wastewater samples were obtained from the City of Cape Town Western Cape Scientific Services. The recoveries were evaluated for the wastewater using standard spiking methods where solutions of the three samples were spiked with H_2O_2 standard solutions of three different concentrations. **Table 5.2** shows the recovery results of H_2O_2 after the three water samples were spiked with 0.2, 0.3 and 0.4 mM concentrations. The average recoveries range from 91.53% to 118.1% with relative standard deviations (RSD) less than 5% based on triplicate tests at each concentration. By considering the calculated recovery and relative standard deviation (RSD) values, it can be observed that the developed sensor holds possible applications in determining certain concentration of H_2O_2.

CHAPTER 6

CONCLUSION AND RECCOMENDATIONS

The goal of this work was to design a highly sensitive and selective non-enzyme H_2O_2 electrochemical sensor. To address this, Ag-Fe_2O_3/POM/RGO modified GCE electrode was prepared based on the combination of metal-metal oxide nanoparticles, polyoxometalate (POM) namely phosphomolybdic acid ($H_3PMo_{12}O_{40}$) and reduced graphene oxide (RGO). Ag-Fe_2O_3/POM/RGO nanocomposite as the selected sensor platform showed good detection towards H_2O_2 concentrations. POM was used to functionalize RGO and modify its surface characteristics. The enhanced electrocatalytic ability of the composite electrode is considered to be the result of the large surface area, high conductivity as well as the fast electron transfer produced by the POM/RGO surface. This sensor showed good repeatability, reproducibility and selectivity towards H_2O_2 detection. There were no significant current changes during the detection of 0.3 mM H_2O_2 in the presence of normal physiological interferents such as ascorbic acid, uric acid, glucose and ethanol. The fabricated sensor's performance was further evaluated in the determination of H_2O_2 in real samples where the results indicated low RSD values ranging from (0.9 to 4.2) % which confirmed high possibility to use the prepared sensor in the future for water diagnosis. The prepared composite displayed the highest H_2O_2 sensing performance with a low detection limit of 0.0029 mM and excellent sensitivity value of 270.96 (μA $mM^{-1}cm^{-2}$) with linear concentration range of (0.3 – 3) mM.

The synergetic effect of RGO, POM and the Ag-Fe_2O_3 nanoparticles and providing high surface area, high conductivity as well as fast electron transfer of the materials are the main factors which increased the performance of the electrode towards H_2O_2 detection. Based on this work, further studies should concentrate on advanced applications of this nanocomposite in other diagnostic purposes i.e. measuring H_2O_2 in the human blood or urine since high levels H_2O_2 can constitute a pathogenic factor in vascular organ damage attendant upon systemic hypertension. Other recommendations may include:

- Blend the POM with any conducting polymer in the same electrode to observe the effect it might have in improving the H_2O_2 sensing performances
- Using more green methods during the synthesising for better dispersion and less agglomeration of composite components.

REFERENCES

Aal, S.K.A., Ionov, A. & Alim, R.N.M. 2018. Simple synthesis of graphene nanocomposites MgO–rGO and - Fe_2O_3–rGO for multifunctional applications. *Applied Physics A*. 0(0):0. DOI: 10.1007/s00339-018-1748-5.

Abou El-Nour, K.M.M., Eftaiha, A., Al-Warthan, A. & Ammar, R.A.A. 2010. Synthesis and applications of silver nanoparticles. *Arabian Journal of Chemistry*. 3(3):135–140. DOI: 10.1016/j.arabjc.2010.04.008.

Ahammad, A.J.S. 2012. Hydrogen Peroxide Biosensors Based on Horseradish Peroxidase and Hemoglobin. *Journal of Biosensors & Bioelectronics*. s9:1–11. DOI: 10.4172/2155-6210.S9-001.

Ajitha, B., Kumar Reddy, Y.A., Reddy, P.S., Jeon, H.-J. & Ahn, C.W. 2016. Role of capping agents in controlling silver nanoparticles size, antibacterial activity and potential application as optical hydrogen peroxide sensor. *RSC Adv*. 6(42):36171–36179. DOI: 10.1039/C6RA03766F.

Amanulla, B., Palanisamy, S., Chen, S.M., Velusamy, V., Chiu, T.W., Chen, T.W. & Ramaraj, S.K. 2017. A non-enzymatic amperometric hydrogen peroxide sensor based on iron nanoparticles decorated reduced graphene oxide nanocomposite. *Journal of Colloid and Interface Science*. 487:370–377. DOI: 10.1016/j.jcis.2016.10.050.

Amir, R.M., Anjum, F.M., Khan, M.I., Khan, M.R., Pasha, I. & Nadeem, M. 2013. Application of Fourier transform infrared (FTIR) spectroscopy for the identification of wheat varieties. *Journal of Food Science and Technology*. 50(5):1018–1023. DOI: 10.1007/s13197-011-0424-y.

Ammam, M. 2013. Materials Chemistry A. *Journal of material chemistry Accepted manuscript*. (207890). DOI: 10.1039/c3ta13397d.

Bader, H., Sturzenegger, V. & Hoigné, J. 1988. Photometric method for the determination of low concentrations of hydrogen peroxide by the peroxidase catalyzed oxidation of N,N-diethyl-p-phenylenediamine (DPD). *Water Research*. 22(9):1109–1115. DOI: 10.1016/0043-1354(88)90005-X.

Bai, W., Nie, F., Zheng, J. & Sheng, Q. 2014. Novel silver nanoparticle-manganese oxyhydroxide-graphene oxide nanocomposite prepared by modified silver mirror reaction and its application for electrochemical sensing. *ACS Applied Materials and Interfaces*. 6(8):5439–5449. DOI: 10.1021/am500641d.

Bandodkar, A.J. & Wang, J. 2014. Non-invasive wearable electrochemical sensors: A review. *Trends in Biotechnology*. 32(7):363–371. DOI: 10.1016/j.tibtech.2014.04.005.

Biabani-ravandi, A., Rezaei, M. & Fattah, Z. 2013. Catalytic performance of Ag/Fe_2O_3 for the low temperature oxidation of carbon monoxide. *CHEMICAL ENGINEERING JOURNAL*. 219:124–130. DOI: 10.1016/j.cej.2012.12.094.

Bo, Z., Shuai, X., Mao, S., Yang, H., Qian, J., Chen, J., Yan, J. & Cen, K. 2014. Green preparation of reduced graphene oxide for sensing and energy storage applications. *Scientific Reports*. 4:1–8. DOI: 10.1038/srep04684.

Bochenkov, V.E. & Sergeev, G.B. 2010. Sensitivity , Selectivity , and Stability of Gas-Sensitive Metal-Oxide Nanostructures. 3:31–52.

Bui, M.P.N., Pham, X.H., Han, K.N., Li, C.A., Kim, Y.S. & Seong, G.H. 2010. Electrocatalytic reduction of hydrogen peroxide by silver particles patterned on single-walled carbon nanotubes. *Sensors and Actuators, B: Chemical*. 150(1):436–441. DOI: 10.1016/j.snb.2010.06.019.

Bykkam, S., Ahmadipour, M., Narisngam, S., Kalagadda, V.R. & Chidurala, S.C. 2015. RETRACTED: Extensive Studies on X-Ray Diffraction of Green Synthesized Silver Nanoparticles. *Advances in Nanoparticles*. 04(01):1–10. DOI: 10.4236/anp.2015.41001.

Chaubey, A. & Malhotra, B.D. 2002. Mediated biosensors. *Biosensors and Bioelectronics*. 17(6–7):441–456. DOI: 10.1016/S0956-5663(01)00313-X.

Chen, J.J.J. & Barteau, M.A. 2016. Electrochemical Properties of Keggin-Structure Polyoxometalates in Acetonitrile: Effects of Countercation, Heteroatom, and Framework Metal Exchange. *Industrial and Engineering Chemistry Research*. 55(37):9857–9864. DOI: 10.1021/acs.iecr.6b02316.

Chen, J., Xu, L., Li, W. & Gou, X. 2005. Fe_2O_3 Nanotubes in Gas Sensor and Lithium-Ion Battery Applications. *Advanced Materials*. 17(5):582–586. DOI: 10.1002/adma.200401101.

Chen, J., Liu, S., Feng, W., Zhang, G. & Yang, F. 2013. Fabrication phosphomolybdic acid–reduced graphene oxide nanocomposite by UV photo-reduction and its electrochemical properties. *Physical Chemistry Chemical Physics*. 15(15):5664. DOI: 10.1039/c3cp43638a.

Chen, S., Yuan, R., Chai, Y. & Hu, F. 2013. Electrochemical sensing of hydrogen peroxide using metal nanoparticles: A review. *Microchimica Acta*. 180(1–2):15–32. DOI: 10.1007/s00604-012-0904-4.

Chen, X., Wu, G., Cai, Z., Oyama, M. & Chen, X. 2014. Advances in enzyme-free electrochemical sensors for hydrogen peroxide , glucose , and uric acid. 689–705. DOI: 10.1007/s00604-013-1098-0.

Chettri, P., Vendamani, V.S., Tripathi, A., Kumar, M., Pathak, A.P. & Tiwari, A. 2017. Applied Surface Science Green synthesis of silver nanoparticle-reduced graphene oxide using Psidium guajava and its application in SERS for the detection of methylene blue. 406:312–318.

Chi, Q. & Dong, S. 1995. Amperometric biosensors based on the immobilization of oxidases in a Prussian blue film by electrochemical codeposition. *Analytica Chimica Acta*. 310(3):429–436. DOI: 10.1016/0003-2670(95)00152-P.

Corr, S.A. 2014. Metal oxide nanoparticles. *SPR Nanoscience*. 2:204–224. DOI: 10.1039/9781849737623-00204.

Cosnier, S. 2005. Affinity biosensors based on electropolymerized films. *Electroanalysis*. 17(19):1701–1715. DOI: 10.1002/elan.200503308.

Cui, K., Song, Y., Yao, Y., Huang, Z. & Wang, L. 2008. A novel hydrogen peroxide sensor based on Ag nanoparticles electrodeposited on DNA-networks modified glassy carbon electrode. *Electrochemistry Communications*. 10(4):663–667. DOI: 10.1016/j.elecom.2008.02.016.

Das, R., Nath, S.S., Chakdar, D., Gope, G. & Bhattacharjee, R. 2010. Synthesis of silver nanoparticles and their optical properties. *Journal of Experimental Nanoscience*. 5(4):357–362. DOI: 10.1080/17458080903583915.

Dhara, K., Ramachandran, T., Nair, B.G. & Satheesh Babu, T.G. 2016. Au nanoparticles decorated reduced graphene oxide for the fabrication of disposable nonenzymatic hydrogen peroxide sensor. *Journal of Electroanalytical Chemistry*. 764:64–70. DOI: 10.1016/j.jelechem.2016.01.011.

Dhawale, V.P., Khobragade, V. & Kulkarni, S.D. 2018. Synthesis and Characterization of Aluminium Oxide (Al_2O_3) Nanoparticles and its Application in Azodye Decolourisation.

2(1):10–17. DOI: 10.11648/j.ijec.20180201.13.

Dinesh, B., Mani, V., Saraswathi, R. & Chen, S.-M. 2014. Direct electrochemistry of cytochrome c immobilized on a graphene oxide–carbon nanotube composite for picomolar detection of hydrogen peroxide. *RSC Advances*. 4(54):28229. DOI: 10.1039/c4ra02789b.

Emiru, T.F. & Ayele, D.W. 2017. Controlled synthesis, characterization and reduction of graphene oxide: A convenient method for large scale production. *Egyptian Journal of Basic and Applied Sciences*. 4(1):74–79. DOI: 10.1016/j.ejbas.2016.11.002.

Evanoff, D.D. & Chumanov, G. 2005. Synthesis and optical properties of silver nanoparticles and arrays. *ChemPhysChem*. 6(7):1221–1231. DOI: 10.1002/cphc.200500113.

Gao, N., Chen, Y. & Jiang, J. 2013. Ag@Fe_2O_3-GO nanocomposites prepared by a phase transfer method with long-term antibacterial property. *ACS Applied Materials and Interfaces*. 5(21):11307–11314. DOI: 10.1021/am403538j.

Geetha Bai, R., Muthoosamy, K., Shipton, F.N., Pandikumar, A., Rameshkumar, P., Huang, N.M. & Manickam, S. 2016. The biogenic synthesis of a reduced graphene oxide–silver (RGO–Ag) nanocomposite and its dual applications as an antibacterial agent and cancer biomarker sensor. *RSC Adv*. 6(43):36576–36587. DOI: 10.1039/C6RA02928K.

Grieshaber, D., MacKenzie, R., Vörös, J. & Reimhult, E. 2008. Electrochemical Biosensors - Sensor Principles and Architectures. *Sensors*. 8(12):1400–1458. DOI: 10.3390/s80314000.

Gumerova, N.I. & Rompel, A. 2018. Synthesis, structures and applications of electron-rich polyoxometalates. *Nature Reviews Chemistry*. 2(2). DOI: 10.1038/s41570-018-0112.

Guo, T., Yao, M.S., Lin, Y.H. & Nan, C.W. 2015. A comprehensive review on synthesis methods for transition-metal oxide nanostructures. *CrystEngComm*. 17(19):3551–3585. DOI: 10.1039/c5ce00034c.

Gupta, S., Aberg, B. & Carrizosa, S. 2017. Functionalized Graphene–Polyoxometalate Nanodots Assembly as “Organic–Inorganic” Hybrid Supercapacitors and Insights into Electrode/Electrolyte Interfacial Processes. *C*. 3(4):24. DOI: 10.3390/c3030024.

Gurvinder Singh Bumbrah, R.M.S. 2016. Raman spectroscopy – Basic principle, instrumentation and selected applications for the characterization of drugs of abuse. *Egyptian Journal of Forensic Sciences*. 27(4):209–215. DOI: 10.1016/j.ejfs.2015.06.001.

Guy, O.J. & Walker, K.D. 2016. Graphene Functionalization for Biosensor Applications. In *Silicon Carbide Biotechnology*. Second Edi ed. Elsevier Inc. 85–141. DOI: 10.1016/B978-0-12-802993-0/00004-6.

Haghighi, B., Hamidi, H. & Gorton, L. 2010. Formation of a robust and stable film comprising ionic liquid and polyoxometalate on glassy carbon electrode modified with multiwalled carbon nanotubes: Toward sensitive and fast detection of hydrogen peroxide and iodate. *Electrochimica Acta*. 55(16):4750–4757. DOI: 10.1016/j.electacta.2010.03.041.

Haider, A. & Kang, I.-K. 2015. Preparation of Silver Nanoparticles and Their Industrial and Biomedical Applications: A Comprehensive Review. *Advances in Materials Science and Engineering*. 2015:1–16. DOI: 10.1155/2015/165257.

Han, J.W. & Kim, J. 2015. Reduced graphene oxide – silver nanoparticle nanocomposite : a potential anticancer nanotherapy. *International Journal of Nanomedecine*. 10:6257–6276. DOI: 10.2147/IJN.S92449.

Honeychurch, K.C. 2012. Printed thick-fi lm biosensors. DOI: 10.1533/9780857096210.2.366.

Van der Horst, C., Silwana, B., Iwuoha, E. & Somerset, V. 2015. Synthesis and Characterization of Bismuth-Silver Nanoparticles for Electrochemical Sensor Applications. *Analytical Letters*. 48(8):1311–1332. DOI: 10.1080/00032719.2014.979357.

Hsu, C.C., Lo, Y.R., Lin, Y.C., Shi, Y.C. & Li, P.L. 2015. A spectrometric method for hydrogen peroxide concentration measurement with a reusable and cost-efficient sensor. *Sensors (Switzerland)*. 15(10):25716–25729. DOI: 10.3390/s151025716.

Hu, W., Zhang, W., Wu, Y. & Qu, W. 2018. Self-assembly and hydrothermal technique syntheized Fe2O3-RGO nanocomposite: The enhancement effect of electrochemical simultaneous detection of honokiol and magnolol. *Journal of Electroceramics*. 40(1):1–10. DOI: 10.1007/s10832-017-0075-0.

Iqbal, M., Gupta, S. & Hussaini, S. 2012. A Review on Electrochemical Biosensors: Principles and Applications. *Advances in Bioresearch*. 3(December):158–163. Available: http://search.ebscohost.com/login.aspx?direct=true&profile=ehost&scope=site&authtype=crawler&jrnl=09764585&AN=90473663&h=kjZ3el/Z5TBys2YaG5uV3hWo/Dup5KLZ13L1N3uIf3RqgiksYGMnE0uFELxcW0UvYMcHfcsvsHYI41/5BWWwaQ==&crl=c.

Ivanova, S. 2014. Hybrid Organic-Inorganic Materials Based on Polyoxometalates and Ionic Liquids and Their Application in Catalysis. *ISRN Chemical Engineering*. 2014(January):1–13. DOI: 10.1155/2014/963792.

Jang, J.S., Yoon, K.Y., Xiao, Y., Fan, F.R.F. & Bard, A.J. 2009. Development of a potential Fe_2O_3-based photocatalyst thin film for water oxidation by scanning electrochemical microscopy: Effects of Ag-Fe_2O_3nanocomposite and Sn doping. *Chemistry of Materials*. 21(20):4803–4810. DOI: 10.1021/cm901056c.

Janshoff, A., Galla, H. & Steinem, C. n.d. Piezoelectric Mass-Sensing Devices as BiosensorsÐAn Alternative to Optical.

Jayanthi, S.A., Nathan, D.M.G.T., Jayashainy, J. & Sagayaraj, P. 2015. A novel hydrothermal approach for synthesizing α-Fe_2O_3, γ-Fe_2O_3 and Fe_3O_4 mesoporous magnetic nanoparticles. *Materials Chemistry and Physics*. 162:316–325. DOI: 10.1016/j.matchemphys.2015.05.073.

K. Ihokura, J.W. 1994. Stannic Oxide gas sensor. 15.

Kang, Z., Liu, Y., Tsang, C.H.A., Ma, D.D.D., Wang, E. & Lee, S.-T. 2009. Heteropolyacid-assisted fabrication of carbon nanostructures under ambient conditions. *Chemical Communications*. 413–415. DOI: 10.1039/b812573b.

Karunakaran, C., Rajkumar, R. & Bhargava, K. 2015. Introduction to Biosensors. *Biosensors and Bioelectronics*. (June):1–68. DOI: 10.1016/B978-0-12-803100-1.00001-3.

Keston, A.S. & Brandt, R. 1965. The fluorometric analysis of ultramicro quantities of hydrogen peroxide. *Analytical Biochemistry*. 11(1):1–5. DOI: 10.1016/0003-2697(65)90034-5.

Khatoon, U.T., Mantravadi, K.M. & Nageswara, G.V.S. 2018. Strategies to synthesise copper oxide nanoparticles and their bio applications – a review. 0836. DOI: 10.1080/02670836.2018.1482600.

Kim, Y. & Shanmugam, S. 2013. Polyoxometalate–Reduced Graphene Oxide Hybrid Catalyst: Synthesis, Structure, and Electrochemical Properties. *ACS Applied Materials & Interfaces*. 5(22):12197–12204. DOI: 10.1021/am4043245.

King, A.A.K., Davies, B.R., Noorbehesht, N., Newman, P., Church, T.L., Harris, A.T., Razal, J.M. & Minett, A.I. 2016. A new raman metric for the characterisation of graphene oxide and its derivatives. *Scientific Reports*. 6:1–6. DOI: 10.1038/srep19491.

Kołodziejczak-radzimska, A. & Jesionowski, T. 2014. Zinc Oxide—From Synthesis to Application: A Review. 2833–2881. DOI: 10.3390/ma7042833.

Kopanja, L., Milosevic, I., Panjan, M., Damnjanovic, V. & Tadic, M. 2016. Sol-gel combustion synthesis, particle shape analysis and magnetic properties of hematite (α-Fe_2O_3) nanoparticles embedded in an amorphous silica matrix. *Applied Surface Science*. 362:380–386. DOI: 10.1016/j.apsusc.2015.11.238.

Koyun, A., Ahlatc, E. & İ, Y.K. 1962. Biosensors and Their Principles.

Kumar, K.V.A., Chandana, L., Ghosal, P. & Subrahmanyam, C. 2017. Simultaneous photocatalytic degradation of p-cresol and Cr (VI) by metal oxides supported reduced graphene oxide. *Molecular Catalysis*. 1–9. DOI: 10.1016/j.mcat.2017.11.014.

Kumar, V., Gupta, R.K., Gundampati, R.K., Singh, D.K., Mohan, S., Hasan, S.H. & Malviya, M. 2018. Enhanced electron transfer mediated detection of hydrogen peroxide using a silver nanoparticle–reduced graphene oxide–polyaniline fabricated electrochemical sensor. *RSC Advances*. 8(2):619–631. DOI: 10.1039/C7RA11466D.

Kyeyune, B. 2017. Atomic Force Microscopy. Africa Institute for Mathematical Science Tanzania. DOI: 10.1063/1.881238.

Lassoued, A., Dkhil, B., Gadri, A. & Ammar, S. 2017. Control of the shape and size of iron oxide (α-Fe_2O_3) nanoparticles synthesized through the chemical precipitation method. *Results in Physics*. 7:3007–3015. DOI: 10.1016/j.rinp.2017.07.066.

Lavin-Lopez, M.D.P., Romero, A., Garrido, J., Sanchez-Silva, L. & Valverde, J.L. 2016. Influence of different improved hummers method modifications on the characteristics of graphite oxide in order to make a more easily scalable method. *Industrial and Engineering Chemistry Research*. 55(50):12836–12847. DOI: 10.1021/acs.iecr.6b03533.

Lee, C.S., Kyu Kim, S. & Kim, M. 2009. Ion-sensitive field-effect transistor for biological sensing. *Sensors*. 9(9):7111–7131. DOI: 10.3390/s90907111.

Lei, C.X., Hu, S.Q., Shen, G.L. & Yu, R.Q. 2003. Immobilization of horseradish peroxidase to a nano-Au monolayer modified chitosan-entrapped carbon paste electrode for the detection of hydrogen peroxide. *Talanta*. 59(5):981–988. DOI: 10.1016/S0039-9140(02)00641-0.

Li, H., Zhang, X., Pang, H., Huang, C. & Chen, J. 2010. PMo 12-functionalized Graphene nanosheet-supported PtRu nanocatalysts for methanol electro-oxidation. *Journal of Solid*

State Electrochemistry. 14(12):2267–2274. DOI: 10.1007/s10008-010-1067-z.

Li, L., Du, Z., Liu, S., Hao, Q., Wang, Y., Li, Q. & Wang, T. 2010. A novel nonenzymatic hydrogen peroxide sensor based on MnO_2/graphene oxide nanocomposite. *Talanta*. 82(5):1637–1641. DOI: 10.1016/j.talanta.2010.07.020.

Li, Y., Zhao, X., Zhang, P., Ning, J., Li, J., Su, Z. & Wei, G. 2015. A facile fabrication of large-scale reduced graphene oxide–silver nanoparticle hybrid film as a highly active surface-enhanced Raman scattering substrate. *J. Mater. Chem. C*. 3(16):4126–4133. DOI: 10.1039/C5TC00196J.

Lin, C.G., Hu, J. & Song, Y.F. 2017. Polyoxometalate-Functionalized Nanocarbon Materials for Energy Conversion, Energy Storage, and Sensor Systems. *Advances in Inorganic Chemistry*. 69:181–212. DOI: 10.1016/bs.adioch.2016.12.004.

Liu, A., Zhou, W., Shen, K., Liu, J. & Zhang, X. 2015a. One-pot hydrothermal synthesis of hematite-reduced graphene oxide composites for efficient removal of malachite green from aqueous solution. *RSC Advances*. 5(22):17336–17342. DOI: 10.1039/c4ra15589k.

Liu, A., Zhou, W., Shen, K., Liu, J. & Zhang, X. 2015b. One-pot hydrothermal synthesis of hematite-reduced graphene oxide composites for efficient removal of malachite green from aqueous solution. *RSC Adv*. 5(22):17336–17342. DOI: 10.1039/C4RA15589K.

Liu, H., Weng, L. & Yang, C. 2017. A review on nanomaterial-based electrochemical sensors for H_2O_2, H_2S and NO inside cells or released by cells. *Microchimica Acta*. 184(5):1267–1283. DOI: 10.1007/s00604-017-2179-2.

Liu, L., Wu, D., Shao, X., Wang, J., Nie, J., Sun, J. & Wang, S. 2017. Synthesis of Fe_2O_3 /reduced graphene oxide composite anode materials with good cycle stability. *Composite Interfaces*. 24(3):257–266. DOI: 10.1080/09276440.2016.1191834.

Liu, M., Liu, R. & Chen, W. 2013. Graphene wrapped Cu_2O nanocubes: Non-enzymatic electrochemical sensors for the detection of glucose and hydrogen peroxide with enhanced stability. *Biosensors and Bioelectronics*. 45:206–212. DOI: 10.1016/J.BIOS.2013.02.010.

Liu, R., Li, S., Yu, X., Zhang, G., Zhang, S., Yao, J., Keita, B., Nadjo, L., et al. 2012. Facile synthesis of Au-nanoparticle/polyoxometalate/graphene tricomponent nanohybrids: An enzyme-free electrochemical biosensor for hydrogen peroxide. *Small*. 8(9):1398–1406. DOI: 10.1002/smll.201102298.

Liu, S., Tian, J., Wang, L. & Sun, X. 2011a. A method for the production of reduced graphene oxide using benzylamine as a reducing and stabilizing agent and its subsequent decoration with Ag nanoparticles for enzymeless hydrogen peroxide detection. *Carbon*. 49(10):3158–3164. DOI: 10.1016/j.carbon.2011.03.036.

Liu, S., Tian, J., Wang, L. & Sun, X. 2011b. Microwave-assisted rapid synthesis of Ag nanoparticles/graphene nanosheet composites and their application for hydrogen peroxide detection. *Journal of Nanoparticle Research*. 13(10):4539–4548. DOI: 10.1007/s11051-011-0410-3.

Liu, S., Tian, J., Wang, L., Zhang, Y., Luo, Y., Li, H., Asiri, A.M., Al-Youbi, A.O., et al. 2012. Fast and Sensitive Colorimetric Detection of H_2O_2 and Glucose: A Strategy Based on Polyoxometalate Clusters. *ChemPlusChem*. 77(7):541–544. DOI: 10.1002/cplu.201200051.

Liu, X., Zhu, Y., Zhu, Z., Qin, Y., Li, F., Tian, H. & Xin, S. 2012. Solid phase microextraction and selective determination of cysteine in whole blood by cyclic voltammetry with silver nanoparticles modified clustered carbon fiber electrodes. *Analytical Methods*. 4(10):3256–3260. DOI: 10.1039/c2ay25369k.

Liu, X., Chen, C., Zhao, Y. & Jia, B. 2013. A Review on the Synthesis of Manganese Oxide Nanomaterials and Their Applications on Lithium-Ion Batteries. 2013.

López, X., Maestre, J.M., Bo, C. & Poblet, J.M. 2001. Electronic properties of polyoxometalates: A DFT study of α/β-[$XM_{12}O_{40}$]n-relative stability (M=W, Mo and X a main group element). *Journal of the American Chemical Society*. 123(39):9571–9576. DOI: 10.1021/ja010768z.

Lorestani, F., Shahnavaz, Z., Mn, P., Alias, Y. & Manan, N.S.A. 2015. One-step hydrothermal green synthesis of silver nanoparticle-carbon nanotube reduced-graphene oxide composite and its application as hydrogen peroxide sensor. *Sensors and Actuators, B: Chemical*. 208:389–398. DOI: 10.1016/j.snb.2014.11.074.

Loryuenyong, V., Totepvimarn, K., Eimburanapravat, P., Boonchompoo, W. & Buasri, A. 2013. Preparation and Characterization of Reduced Graphene Oxide Sheets via Water-Based Exfoliation and Reduction Methods. 2013.

Lu, W., Liao, F., Luo, Y., Chang, G. & Sun, X. 2011. Electrochimica Acta Hydrothermal synthesis of well-stable silver nanoparticles and their application for enzymeless hydrogen peroxide detection. *Electrochimica Acta*. 56(5):2295–2298. DOI: 10.1016/j.electacta.2010.11.053.

Luo, X., Morrin, A., Killard, A.J. & Smyth, M.R. 2006. Application of nanoparticles in electrochemical sensors and biosensors. *Electroanalysis*. 18(4):319–326. DOI: 10.1002/elan.200503415.

Mallick, S., Rana, S. & Parida, K. 2012. Facile Method for the Synthesis of Phosphomolybdic Acid Supported on Zirconia − Ceria Mixed Oxide and Its Catalytic Evaluation in the Solvent-Free Oxidation of Benzyl Alcohol.

Manivel, A. & Anandan, S. 2011. Silver nanoparticles embedded phosphomolybdate-polyaniline hybrid electrode for electrocatalytic reduction of H_2O_2. *Journal of Solid State Electrochemistry*. 15(1):153–160. DOI: 10.1007/s10008-010-1080-2.

Mantzila, A.G. & Prodromidis, M.I. 2005. Performance of impedimetric biosensors based on anodically formed Ti/TiO_2 electrodes. *Electroanalysis*. 17(20):1878–1885. DOI: 10.1002/elan.200503306.

Marcos Fernández-Garcia, J.A.R. 2007. Diseases Transmitted by Mosquitoes. (October). DOI: BNL-79479-2007-BC.

Mascini, M. 2006. A Brief Story of Biosensor Technology. In *Biotechnological Applications of Photosynthetic Proteins Biochips, Biosensors and Biodevices*. 4–10. DOI: 10.1007/978-0-387-36672-2_2.

MEHRVAR, M. & ABDI, M. 2004. Recent Developments, Characteristics, and Potential Applications of Electrochemical Biosensors. *Analytical Sciences*. 20(8):1113–1126. DOI: 10.2116/analsci.20.1113.

Mercier, D., Ben Haddada, M., Huebner, M., Knopp, D., Niessner, R., Salmain, M., Proust, A. & Boujday, S. 2015. Polyoxometalate nanostructured gold surfaces for sensitive biosensing of benzo[a]pyrene. *Sensors and Actuators, B: Chemical*. 209:770–774. DOI: 10.1016/j.snb.2014.12.015.

Mital, G.S. & Manoj, T. 2011. A review of TiO_2 nanoparticles. (March 2014). DOI: 10.1007/s11434-011-4476-1.

Moozarm Nia, P. 2017. Fabrication and evaluation of novel non-enzymatic hydrogen peroxide and glucose sensors based on conducting polymer/nanocomposites. Available:

http://studentsrepo.um.edu.my/id/eprint/7201.

Munajad, A., Subroto, C. & Suwarno. 2018. Fourier transform infrared (FTIR) spectroscopy analysis of transformer paper in mineral oil-paper composite insulation under accelerated thermal aging. *Energies*. 11(2). DOI: 10.3390/en11020364.

Munyao, P. 2008. Amperometric biosensor systems prepared on poly(aniline-ferrocenium hexafluorophosphate) composites doped with poly(vinyl sulfonic acid sodium salt).

Narasimharao, K., Al-Shehri, A. & Al-Thabaiti, S. 2015. Porous Ag-Fe_2O_3 nanocomposite catalysts for the oxidation of carbon monoxide. *Applied Catalysis A: General*. 505:431–440. DOI: 10.1016/j.apcata.2015.05.017.

Nurani, S.J., Saha, K.C., Rahman Khan, M.A. & Sunny, S.M.H. 2015. Silver Nanoparticles Synthesis, Properties, Applications and Future Perspectives: A Short Review. *IOSR Journal of Electrical and Electronics Engineering Ver. I*. 10(6):117–126. DOI: 10.9790/1676-1061117126.

Olga S. Ivanova & Francis P. Zamborini. 2010. Size – Dependent Electrochemical Oxidation of Silver Nanoparticles. *J. Am. Chem. Soc.* 132(1):70–72. DOI: 10.1021/ja908780g.

Omidi, M., Fatehinya, A., Farahani, M., Akbari, Z., Shahmoradi, S., Yazdian, F., Tahriri, M. & Vashaee, D. 2017. Characterization of biomaterials. In *Biomaterials for Oral and Dental Tissue Engineering*. Elsevier Ltd. 97–115. DOI: 10.1016/B978-0-08-100961-1.00007-4.

Pan, L., Tang, J. & Chen, Y. 2013. Synthesis of Fe_3O_4, Fe_2O_3, Ag/Fe_3O_4 and Ag/Fe_2O_3 nanoparticles and their electrocatalytic properties. *Science China Chemistry*. 56(3):362–369. DOI: 10.1007/s11426-012-4763-y.

Pareek, V., Bhargava, A., Gupta, R., Jain, N. & Panwar, J. 2017. Synthesis and Applications of Noble Metal Nanoparticles: A Review. *Advanced Science, Engineering and Medicine*. 9(7):527–544. DOI: 10.1166/asem.2017.2027.

Paul, B., Purkayastha, D.D., Dhar, S.S., Das, S. & Haldar, S. 2016. Facile one-pot strategy to prepare Ag/Fe_2O_3decorated reduced graphene oxide nanocomposite and its catalytic application in chemoselective reduction of nitroarenes. *Journal of Alloys and Compounds*. 681:316–323. DOI: 10.1016/j.jallcom.2016.04.229.

Paul, N., Hammond, R.B., Hunter, T.N., Edmondson, M., Maxwell, L. & Biggs, S. 2015. Synthesis of nuclear waste simulants by reaction precipitation: Formation of caesium phosphomolybdate, zirconium molybdate and morphology modification with citratomolybdate complex. *Polyhedron*. 89:129–141. DOI: 10.1016/j.poly.2014.12.030.

Perumal, V. & Hashim, U. 2014. Advances in biosensors:Principle, architecture and applications. *Journal of Applied Biomedicine*. 12:1–15.

Pervaiz, E., Gul, I.H. & Anwar, H. 2013. Hydrothermal synthesis and characterization of $CoFe_2O_4$nanoparticles and nanorods. *Journal of Superconductivity and Novel Magnetism*. 26(2):415–424. DOI: 10.1007/s10948-012-1749-0.

Petit, C. & Bandosz, T.J. 2009. MOF – graphite oxide nanocomposites : surface characterization and evaluation as adsorbents of ammonia. *J. Mater. Chem.* 19:6521–6528. DOI: 10.1039/b908862h.

Poblet, J.M., López, X. & Bo, C. 2003. Ab initio and DFT modelling of complex materials: towards the understanding of electronic and magnetic properties of polyoxometalates. *Chem. Soc. Rev.* 32(5):297–308. DOI: 10.1039/B109928K.

Pohanka, M. & Republic, C. 2008. Electrochemical biosensors – principles and applications. *Methods*. 6(2):57–64. Available: http://www.zsf.jcu.cz/jab/6_2/pohanka.pdf.

Pope, M.T. & Müller, A. 1991. Polyoxolometalate chemistry - An old field with new dimensions in several disciplines. *Angewandte Chemie International Edition*. 30(1):34–48. DOI: 10.1002/anie.199100341.

Press, D. 2011. Memecylon edule leaf extract mediated green synthesis of silver and gold nanoparticles. 1265–1278.

Qi, C.C. & Zheng, J. Bin. 2016. Synthesis of Fe_3O_4-Ag nanocomposites and their application to enzymeless hydrogen peroxide detection. *Chemical Papers*. 70(4):404–411. DOI: 10.1515/chempap-2015-0224.

Rocchitta, G., Spanu, A., Babudieri, S., Latte, G., Madeddu, G., Galleri, G., Nuvoli, S., Bagella, P., et al. 2016. Enzyme biosensors for biomedical applications: Strategies for safeguarding analytical performances in biological fluids. *Sensors (Switzerland)*. 16(6). DOI: 10.3390/s16060780.

Ronkainen, N.J., Halsall, H.B. & Heineman, W.R. 2010. Electrochemical biosensors. *Chemical Society Reviews*. 39(5):1747. DOI: 10.1039/b714449k.

Rowley-Neale, S.J., Randviir, E.P., Abo Dena, A.S. & Banks, C.E. 2018. An overview of recent applications of reduced graphene oxide as a basis of electroanalytical sensing platforms. *Applied Materials Today*. 10:218–226. DOI: 10.1016/j.apmt.2017.11.010.

Sang, S., Li, D., Zhang, H., Sun, Y., Jian, A., Zhang, Q. & Zhang, W. 2017. Facile synthesis of AgNPs on reduced graphene oxide for highly sensitive simultaneous detection of heavy metal ions. *RSC Advances*. 7(35):21618–21624. DOI: 10.1039/C7RA02267K.

Saragi, T., Santika, A.S., Permana, B., Syakir, N., Kartawidjaja, M. & Risdiana. 2017. Synthesis and Properties of Iron Oxide Particles Prepared by Hidrothermal Method. *IOP Conference Series: Materials Science and Engineering*. 196(1):2–6. DOI: 10.1088/1757-899X/196/1/012025.

Sartzi, H., Miras, H.N., Vilà-Nadal, L., Long, D.L. & Cronin, L. 2015. Trapping the δ Isomer of the Polyoxometalate-Based Keggin Cluster with a Tripodal Ligand. *Angewandte Chemie - International Edition*. 54(51):15488–15492. DOI: 10.1002/anie.201505377.

Scandurra, G., Arena, A., Ciofi, C. & Saitta, G. 2013. Electrical Characterization and Hydrogen Peroxide Sensing Properties of Gold/Nafion:Polypyrrole/MWCNTs Electrochemical Devices. *Sensors*. 13(3):3878–3888. DOI: 10.3390/s130303878.

Schnablegger, H. & Singh, Y. 2013. The SAXS guide: getting acquainted with the principles. *Anton Paar*. 124.

Shaikh, A., Parida, S. & Böhm, S. 2016. One step eco-friendly synthesis of Ag–reduced graphene oxide nanocomposite by phytoreduction for sensitive nitrite determination. *RSC Advances*. 6(102):100383–100391. DOI: 10.1039/C6RA23655C.

Shan, C., Yang, H., Song, J., Han, D., Ivaska, A. & Niu, L. 2009. Direct Electrochemistry of Glucose Oxidase and Biosensing for Glucose Based on Graphene. 81(6):2378–2382.

Shang, J., Ma, L., Li, J., Ai, W., Yu, T. & Gurzadyan, G.G. 2012. The origin of fluorescence from graphene oxide. *Scientific Reports*. 2:1–8. DOI: 10.1038/srep00792.

Smarzewska, S. & Ciesielski, W. 2014. Electroanalysis of pindolol on a GCE modified with reduced graphene oxide. *Analytical Methods*. 6(14):5038–5046. DOI: 10.1039/c4ay00648h.

Smith, S.J., Huang, B., Liu, S., Liu, Q., Olsen, R.E., Boerio-Goates, J. & Woodfield, B.F. 2015. Synthesis of metal oxide nanoparticles via a robust "solvent-deficient" method. *Nanoscale*. 7(1):144–156. DOI: 10.1039/c4nr04964k.

Son, K. & Jang, Z. 2013. NMR investigation of Ag nanoparticles. *Journal of the Korean Physical Society*. 62(2):292–296. DOI: 10.3938/jkps.62.292.

Srikar, S.K., Giri, D.D., Pal, D.B., Mishra, P.K. & Upadhyay, S.N. 2016. Green Synthesis of Silver Nanoparticles: A Review. *Green and Sustainable Chemistry*. 06(01):34–56. DOI: 10.4236/gsc.2016.61004.

Subrahmanyam, S., Piletsky, S.A. & Turner, A.P.F. 2002. Application of natural receptors in sensors and assays. *Analytical Chemistry*. 74(16):3942–3951. DOI: 10.1021/ac025673+.

Syafiuddin, A., Salmiati, Salim, M.R., Beng Hong Kueh, A., Hadibarata, T. & Nur, H. 2017. A Review of Silver Nanoparticles: Research Trends, Global Consumption, Synthesis, Properties, and Future Challenges. *Journal of the Chinese Chemical Society*. 64(7):732–756. DOI: 10.1002/jccs.201700067.

Tarvin, M., McCord, B., Mount, K., Sherlach, K. & Miller, M.L. 2010. Optimization of two methods for the analysis of hydrogen peroxide: High performance liquid chromatography with fluorescence detection and high performance liquid chromatography with electrochemical detection in direct current mode. *Journal of Chromatography A*. 1217(48):7564–7572. DOI: 10.1016/j.chroma.2010.10.022.

Teymourian, H., Salimi, A. & Khezrian, S. 2013. Fe_3O_4 magnetic nanoparticles/reduced graphene oxide nanosheets as a novel electrochemical and bioeletrochemical sensing platform. *Biosensors and Bioelectronics*. 49:1–8. DOI: 10.1016/j.bios.2013.04.034.

Thevenot, D.R., Toth, K., Dursts, R.A. & Wilson, G.S. 1999. Electrochemical Biosensors: Recommended Definitions and Classification (Technical Report). *Pure Applied Chemistry*. 71(12):2333–2348. DOI: 10.1016/S0956-5663(01)00115-4.

Thévenot, D.R., Toth, K., Durst, R.A. & Wilson, G.S. 2001. Electrochemical biosensors: Recommended definitions and classification. *Biosensors and Bioelectronics*. 16(1–2):121–131. DOI: 10.1016/S0956-5663(01)00115-4.

Tian, J., Liu, S. & Sun, X. 2010. Supramolecular microfibrils of o-phenylenediamine dimers: Oxidation-induced morphology change and the spontaneous formation of Ag nanoparticle decorated nanofibers. *Langmuir*. 26(19):15112–15116. DOI: 10.1021/la103038m.

To, I. & Biosensors, O. 2005. *Optical biosensors*.

Tran, Q.H., Nguyen, V.Q. & Le, A.T. 2013. Silver nanoparticles: Synthesis, properties, toxicology, applications and perspectives. *Advances in Natural Sciences: Nanoscience and Nanotechnology*. 4(3). DOI: 10.1088/2043-6262/4/3/033001.

Uchida, S., Satoh, Y., Yamashiro, N. & Satoh, T. 2004. Determination of hydrogen peroxide in water by chemiluminescence detection, (II) theoretical analysis of luminol chemiluminescence processes. *Journal of Nuclear Science and Technology*. 41(9):898–906. DOI: 10.1080/18811248.2004.9715562.

Vasileva, P., Donkova, B., Karadjova, I. & Dushkin, C. 2011. Synthesis of starch-stabilized silver nanoparticles and their application as a surface plasmon resonance-based sensor of hydrogen peroxide. *Colloids and Surfaces A: Physicochemical and Engineering Aspects*. 382(1–3):203–210. DOI: 10.1016/j.colsurfa.2010.11.060.

Wang, J. 2006. *Analytical Electrochemistry, Third Edition*. DOI: 10.1002/0471790303.

Wang, M., Sheng, Q., Zhang, D., He, Y. & Zheng, J. 2012. TiC nanoparticles-chitosan composite film for the direct electron transfer of myoglobin and its application in biosensing. *Bioelectrochemistry*. 86:46–53. DOI: 10.1016/j.bioelechem.2012.01.009.

Wang, M.Y., Shen, T., Wang, M., Zhang, D.E., Tong, Z.W. & Chen, J. 2014. One-pot synthesis of α-Fe_2O_3 nanoparticles-decorated reduced graphene oxide for efficient nonenzymatic H_2O_2 biosensor. *Sensors and Actuators, B: Chemical*. 190:645–650. DOI: 10.1016/j.snb.2013.08.091.

Wang, Y., Xu, H., Zhang, J. & Li, G. 2008. Electrochemical sensors for clinic analysis. *Sensors*. 8(4):2043–2081. DOI: 10.3390/s8042043.

Wang, Y., Wu, Y., Zhao, C. & Wang, F. 2014. Fabrication of Electrochemical Reduced Graphene Oxide Films on Glassy Carbon Electrode by Pulsed Potentiostatic Methods and Its Electrochemical Application. *Journal of the Chinese Chemical Society*. 61(11):1245–1253. DOI: 10.1002/jccs.201400189.

Wang, Z., Han, Q., Xia, J., Xia, L., Bi, S., Shi, G., Zhang, F., Xia, Y., et al. 2014. A novel phosphomolybdic acid-polypyrrole/graphene composite modified electrode for sensitive determination of folic acid. *Journal of Electroanalytical Chemistry*. 726:107–111. DOI: 10.1016/j.jelechem.2014.05.013.

Weckhuysen, B.M. 2004. CHAPTER 12 Ultraviolet-Visible Spectroscopy. 255–270.

Wei, J., Qiu, J., Li, L., Ren, L., Zhang, X., Chaudhuri, J. & Wang, S. 2012. A reduced graphene oxide based electrochemical biosensor for tyrosine detection. *Nanotechnology*. 23(33). DOI: 10.1088/0957-4484/23/33/335707.

Welch, C.M., Banks, C.E., Simm, A.O. & Compton, R.G. 2005. Silver nanoparticle assemblies supported on glassy-carbon electrodes for the electro-analytical detection of hydrogen peroxide. *Analytical and Bioanalytical Chemistry*. 382(1):12–21. DOI: 10.1007/s00216-005-3205-5.

Wenner, S., Jones, L., Marioara, C.D. & Holmestad, R. 2017. Atomic-resolution chemical mapping of ordered precipitates in Al alloys using energy-dispersive X-ray spectroscopy. *Micron*. 96:103–111. DOI: 10.1016/j.micron.2017.02.007.

Xiao, L., Schroeder, M., Kluge, S., Balducci, A., Hagemann, U., Schulz, C. & Wiggers, H. 2015. Direct self-assembly of Fe_2O_3/reduced graphene oxide nanocomposite for high-performance lithium-ion batteries. *Journal of Materials Chemistry A*. 3(21):11566–11574. DOI: 10.1039/c5ta02549d.

Xu, W.-P., Zhang, L.-C., Li, J.-P., Lu, Y., Li, H.-H., Ma, Y.-N., Wang, W.-D. & Yu, S.-H. 2011. Facile synthesis of silver@graphene oxide nanocomposites and their enhanced antibacterial properties. *Journal of Materials Chemistry*. 21(12):4593. DOI: 10.1039/c0jm03376f.

Y, B.H., Veronique, M., Hua, L., Halliwell, B., Clement, M. V & Long, L.H. 2000. Hydrogen peroxide in the human body. *FEBS letters*. 486(1):14–17. DOI: 10.1016/S0014-5793(00)02197-9.

Yang, M.H., Kim, D.S., Lee, T.J., Lee, S.J., Lee, K.G. & Choi, B.G. 2016a. Polyoxometalate-grafted graphene nanohybrid for electrochemical detection of hydrogen peroxide and glucose. *Journal of Colloid and Interface Science*. 468:51–56. DOI: 10.1016/j.jcis.2016.01.047.

Yang, M.H., Kim, D.S., Lee, T.J., Lee, S.J., Lee, K.G. & Choi, B.G. 2016b. Polyoxometalate-grafted graphene nanohybrid for electrochemical detection of hydrogen peroxide and glucose. *Journal of Colloid and Interface Science*. 468:51–56. DOI: 10.1016/j.jcis.2016.01.047.

Yi, Q., Niu, F., Li, L., Du, R., Zhou, Z. & Liu, X. 2011. Novel nanoporous silver particles for electro-reduction of hydrogen peroxide in alkaline media. *Journal of Electroanalytical Chemistry*. 654(1–2):60–65. DOI: 10.1016/j.jelechem.2011.01.031.

Yokuş, Ö.A., Kardaş, F., Akyildirim, O., Eren, T., Atar, N. & Yola, M.L. 2016. Sensitive voltammetric sensor based on polyoxometalate/reduced graphene oxide nanomaterial: Application to the simultaneous determination of l-tyrosine and l-tryptophan. *Sensors and Actuators, B: Chemical*. 233:47–54. DOI: 10.1016/j.snb.2016.04.050.

Yola, M.L., Atar, N., Eren, T., Karimi-Maleh, H. & Wang, S. 2015. Sensitive and selective determination of aqueous triclosan based on gold nanoparticles on polyoxometalate/reduced graphene oxide nanohybrid. *RSC Adv*. 5(81):65953–65962. DOI: 10.1039/C5RA07443F.

Yuan, B., Song, L., Liew, K.M. & Hu, Y. 2015a. Solid acid-reduced graphene oxide nanohybrid for enhancing thermal stability, mechanical property and flame retardancy of polypropylene. *RSC Advances*. 5(51):41307–41316. DOI: 10.1039/c5ra04699h.

Yuan, B., Song, L., Liew, K.M. & Hu, Y. 2015b. Solid acid-reduced graphene oxide nanohybrid for enhancing thermal stability, mechanical property and flame retardancy of polypropylene. *RSC Advances*. 5(51):41307–41316. DOI: 10.1039/C5RA04699H.

Yusoff, N., Rameshkumar, P., Mehmood, M.S., Pandikumar, A., Lee, H.W. & Huang, N.M. 2017. Ternary nanohybrid of reduced graphene oxide-nafion@silver nanoparticles for boosting the sensor performance in non-enzymatic amperometric detection of hydrogen peroxide. *Biosensors and Bioelectronics*. 87(July 2016):1020–1028. DOI: 10.1016/j.bios.2016.09.045.

Zainal Abidin Ali Shamala Devi Sekaran, and R. Puteh, R.Y. (in press). Green Synthesis of Silver Nanoparticles Using Apple Extract and Its Antibacterial Properties. *Advances in Materials Science and Engineering*. 2016:ID 4102196 (6 pages). DOI: 10.1155/2016/4102196.

Zhang, N. & Zheng, J. 2017. Synthesis of Ag–Fe_2O_3–RGO nanocomposites for the electrocatalytic reduction of H_2O_2. *Journal of Materials Science: Materials in Electronics*. 28(15):11209–11216. DOI: 10.1007/s10854-017-6909-3.

Zhang, H., Xie, A., Shen, Y., Qiu, L. & Tian, X. 2012. Layer-by-layer inkjet printing of fabricating reduced graphene-polyoxometalate composite film for chemical sensors. *Physical Chemistry Chemical Physics*. 14(37):12757. DOI: 10.1039/c2cp41561e.

Zhang, W., Bi, E., Li, M. & Gao, L. 2016. Synthesis of Ag/RGO composite as effective conductive ink filler for flexible inkjet printing electronics. *Colloids and Surfaces A:*

Physicochemical and Engineering Aspects. 490:232–240. DOI: 10.1016/j.colsurfa.2015.11.014.

Zhang, X.F., Liu, Z.G., Shen, W. & Gurunathan, S. 2016. Silver nanoparticles: Synthesis, characterization, properties, applications, and therapeutic approaches. *International Journal of Molecular Sciences*. 17(9). DOI: 10.3390/ijms17091534.

Zhao, C., Zhang, H. & Zheng, J. 2017. A non-enzymatic electrochemical hydrogen peroxide sensor based on Ag decorated boehmite nanotubes/reduced graphene oxide nanocomposites. *Journal of Electroanalytical Chemistry*. 784:55–61. DOI: 10.1016/j.jelechem.2016.12.005.

Zhao, W., Wang, H., Qin, X., Wang, X., Zhao, Z., Miao, Z., Chen, L., Shan, M., et al. 2009. A novel nonenzymatic hydrogen peroxide sensor based on multi-wall carbon nanotube/silver nanoparticle nanohybrids modified gold electrode. *Talanta*. 80(2):1029–1033. DOI: 10.1016/j.talanta.2009.07.055.

Zhou, D. & Han, B.G. 2010. Graphene-based nanoporous materials assembled by mediation of polyoxometalate nanoparticles. *Advanced Functional Materials*. 20(16):2717–2722. DOI: 10.1002/adfm.200902323.

Zhou, M., Zhai, Y. & Dong, S. 2009. Electrochemical Sensing and Biosensing Platform Based on Chemically Reduced Graphene Oxide. 81(14):5603–5613.